UNIVERSIDAD NACIONAL DE INGENIERÍA

FACULTAD DE CIENCIAS

UNIDAD DE POSGRADO

"OPTIMIZATION OF TRANSPARENT CONDUCTING OXIDES IN HETEROJUNCTION SOLAR CELLS BY EXCIMER LASER ANNEALING"

TESIS

PARA OPTAR EL GRADO ACADEMICO DE MAESTRO EN CIENCIAS CON MENCION EN ENERGIAS RENOVABLES Y EFICIENCIA ENERGETICA

ELABORADO POR

JERZY JAVIER SUÁREZ BERRÚ

Asesor

Dr. MANFRED HORN

LIMA – PERÚ

2015

Table of contents

ACKNOWLEDGEMENTS

Quisiera agradecer en primer lugar a la Doctora Delfina Muñoz, jefa del Laboratorio de las células de HETerounión (LHET), por brindarme la oportunidad de realizar esta pasantía de 5 meses en el INES. Además quisiera agradecer a la Ingeniera Perrine Carroy, quien fue la persona encargada de orientarme y dirigir mi trabajo durante mi estancia en el laboratorio de Heterounión, asimismo quisiera agradecer al Ingeniero Anthony Valla por haber compartido parte de su conocimiento conmigo en lo referente a caracterización óptica y por estar siempre dispuesto a ayudar. Agradezco también a Marc Pirot por haberme mostrado el funcionamiento del láser Excico para realizar el recocido superficial de películas delgadas por láser.

Esta pasantía no hubiese sido posible sin el apoyo del gobierno peruano a través del Concytec quien financia la maestría en energías renovables y eficiencia energética en Perú y además colaboró con los billetes de avión para viajar a Francia. De igual forma quisiera agradecer al CEA-LITEN por haberme aceptado como *stagiaire* en sus laboratorios y haberme dado la posibilidad de formar parte de un equipo de primer nivel en el sector fotovoltaico.

De igual manera agradezco al Dr. Robert Baptist por su apoyo académico y al Dr. Manfred Hörn quien ha sido mi asesor y es una referencia en energía solar en el Perú.

Finalmente quiero agradecer a mis padres por su honestidad y amor por el trabajo que me han inspirado toda la vida, gracias una vez más por su apoyo sincero e incondicional.

Lima, 16 de Junio de 2015

Javier Suárez

INTRODUCTION

One of the most important problems in our society is the lack of clean energy sources to overcome the energetic crisis and global warming. For this reason, I enrolled "Master en Energías Renovables y Eficiencia Energética" at UNI. This master gave me a good training and knowledge to face real problems concerning renewable energies. I chose photovoltaic solar energy because my major interest in physics are solid state physics and material science, in this manner I could bring together my two passions for material science and green energy.

In April 2014, I had the unique chance to go to Institut National de l'Energie Solaire (INES) to make an internship for five month. The principal objective of this internship at Laboratoire de Heterojunction (LHET) in INES was to test the Excimer Laser Annealing (ELA) to improve HET solar cell performance through the amelioration of optical transmission and through the reduction of electrical resistance of Indium Tin Oxide (ITO).

We also studied the impact of ELA on the most important Transparent Conducting oxides (TCO) in research at INES, such as: ITO (Indium Tin Oxide), AZO (Aluminum doped Zinc Oxide) and IOH (hydrogen doped Indium Oxide). We measured different physical properties of thin films such as: optical transmission, electrical conductivity, sheet resistance, index of refraction. We measured also the size of ITO grains by SEM. We also studied electrical properties of two different solar cells (R&D and Pilot line measuring I-V curve, lifetime of charge carriers, Pseud Fill Factor, series and shunt resistance in solar cell.

Almost all these techniques are covered briefly in this thesis to show the fundamentals of physics of the electronic devices to know what we were really measuring.

At the end of this report, conclusions are presented in two parts one for the characterization of TCO thin films and the other one for the HET solar cell characterization.

1 OBJECTIVES OF ELA

In this chapter, we describe the most important constraints in the improvement of amorphous/crystalline Silicon Solar cells and we also mention some of the objectives of this internship at INES.

1.1 Short Description of the problem context

The core of Silicon Heterojunction solar cells (HET cell) is composed basically by two materials: Hydrogenated Amorphous silicon (a-Si:H) and Crystalline Silicon (c-Si). HET cells show high performance (24.7% demonstrated) (Taguchi, 2013) thanks to the hydrogen contained in the amorphous Silicon that allows to reach a very good passivation of the defects at the surface of the c-Si substrate. In addition the field effect passivation at the p-n junction is intensified by the band discontinuities generated by the use of two materials with different band gaps (c-Si (n) / a-Si:H (p)). Both effects allow to obtain record open-circuit voltages (V_{OC}): up to 750 mV demonstrated (Taguchi, 2013). However, the a-Si:H is a poor electrical conductor with almost no anti-reflective properties: this, on the one hand, totally hinders the collection of the photogenerated carriers and their transport to the metallic contacts, and, on the other hand, prevents a lot of incoming light from entering the cell. Therefore, it is necessary to add a thin film of an additional material that overcomes these constraints. The common materials used for this purpose are known as Transparent Conducting Oxides (TCOs), such as tin-doped indium oxide or Indium Tin Oxide (ITO), Aluminum-doped Zinc Oxide (AZO), Hydrogen-doped Indium Oxide (IO:H), etc. At INES, ITO is incorporated in HET technology whereas AZO and IO:H are still at research level.

The ITO is deposited onto the HET solar cell as a thin film. Depending on the fabrication conditions, ITO thin films can be highly transparent and act as a good anti-reflective coating on silicon thanks to adapted refractive index and thickness, thus allowing a maximum of photons reaching the cell, subsequently producing photogenerated charge carriers. ITO thin films can also be a good conductor that allows the collection of the photogenerated carriers in the cell over its whole surface and brings them to the metallic contacts. Nonetheless, optical and electrical properties are not independent and a compromise has to be found. Moreover, because of the low temperature procedures used for fabricating hydrogenated amorphous silicon (T_{dep} < 200°C), ITO must be synthesized also at low temperatures to avoid any damaging of the a-Si:H layers and of the cell performance, thus producing a non-optimal material (amorphous or polycrystalline ITO with non-optimal opto-electrical properties). During this internship, in order to improve the properties of ITO thin films without damaging amorphous silicon material, we annealed ITO thin films by using an excimer laser trying to enhance the compromise between transmission and electrical conductivity. The use of a laser is of particular interest in that case since it allows a depth-localized annealing that should limit the damage caused to the underlying a-Si:H layers.

1.2 Objectives of this Internship

In order to improve the performance of a solar cell, three main actions can be performed:

1. Maximizing the light which is absorbed by the material to maximize the current flowing out of the cell: described with the value of the short circuit current (Jsc).

2. Maximizing the extraction of photogenerated charges carriers with the action of a maximized electric field: described with the value of the open circuit voltage (Voc).

3. Minimizing electric losses (leakage current, series resistance, carrier recombination…): described by a maximized Fill Factor (FF).

The principal objective of this internship is to study the possibility to improve HET solar cells performance through the improvement optical transmission (in order to maximize cell J_{SC}) and through the reduction of electrical resistance (in order to improve FF) of ITO thin films by using excimer laser annealing. First of all, we made a study of laser annealing of ITO thin films deposited on glass substrates and crystalline Silicon substrates to know the amount of laser energy that is required to produce changes in the ITO properties. After that, we made excimer laser annealing of ITO thin films on HET solar cells under different conditions of laser energy density to study its influence on the cell performances. Finally, some AZO and IOH thin films were also annealed with the excimer laser to measure changes in conductivity and transmission.

2 HETEROJUNCTION SOLAR CELLS

In this chapter, a summary of the fundamentals of photovoltaics is presented. Afterwards the different steps of fabrication of a solar amorphous/crystalline heterojunction solar cell are showed, then the mechanism of functioning of a HET solar cell is described.

2.1 Short Introduction to Photovoltaics

In this section, a very quick discussion of the principal parameters and characteristics of a solar cell are presented: this will help to understand better the kind of solar cell (HET) that is going to be studied in this internship.

2.1.1 Photovoltaic Effect

The principle of photovoltaics (PV) is based on the conversion of solar energy (light from the sun) into electrical energy (electric current). This photovoltaic energy conversion primarily needs a material which can promote an electron to a higher energy state by absorbing a photon; secondly, this higher-energy electron must pass through an external circuit to lose its extra energy and then return to the solar cell. Many materials could be used for this purpose. However semiconductors are usually utilized by the Photovoltaic Industry. In Figure 2-1, the principal parts of a standard c-Si solar cell are explained, such as the types of semiconductors (p and n doped silicon), the boundary layer (interface between regions of the semiconductors), and the metallic electrodes. The production of photocurrent in a solar cell can be summarized as:

1) Generation of electron-holes pairs (EHPs) in the solar cell by absorption of photons.
2) Separation of electrons and holes at the junction by the buit-in potential (V_{bi}).
3) Collection of electrons and holes at the terminals.

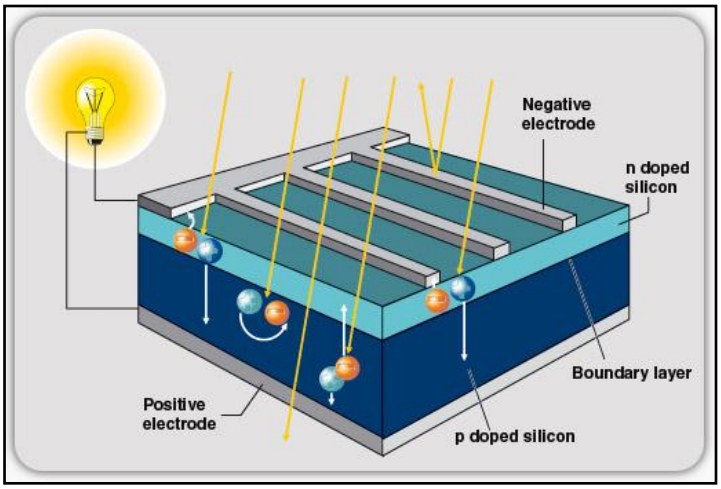

Figure 2-1: Principals parts of a standard crystalline Silicon solar cell (Smets, 2014).

2.1.2 Photovoltaic Technologies

There are many technologies that use the Photovoltaic Effect. They can be classified in three different generations regarding their efficiency, cost per Watt peak (Wp) [1] and raw materials (Figure 2-2):

[1] The nominal power of a PV module is determined by measuring in an electric circuit the current and voltage while the resistance is varying under standard conditions (1000W/m^2 illumination with A.M 1.5 spectrum at 25ºC): the nominal power is the highest measured power.

1) 1st Generation Solar cells

This generation is based on Silicon wafers. This is one of the oldest technologies and 90% of the market uses this technology. Some examples of this kind of PV technology are:

- Homojunction Silicon Solar cell
- Hydrogenated Amorphous/ Crystalline Silicon solar cell

2) 2nd Generation Solar cells

This generation is based on thin films deposited on glass or any other kind of low-cost substrate. The most important technologies are:

- a-Si:H solar cells, a-Si:H/µc-Si:H tandem solar cells
- Cadmium Teluride Solar Cell
- Coper Indium Galium Selenide (CIGS) Solar Cell
- Organic/Dye sensitized Solar Cell
- III-V PV technologies (GaAs)

3) 3rd Generation Solar cells

These technologies are based on innovative ideas and are still at research level. Some of these technologies are:

- Multi-gap solar cells
- Quantum dots Solar cells
- Hot carriers Solar cells
- Down-convertor or up convertor Solar Cells

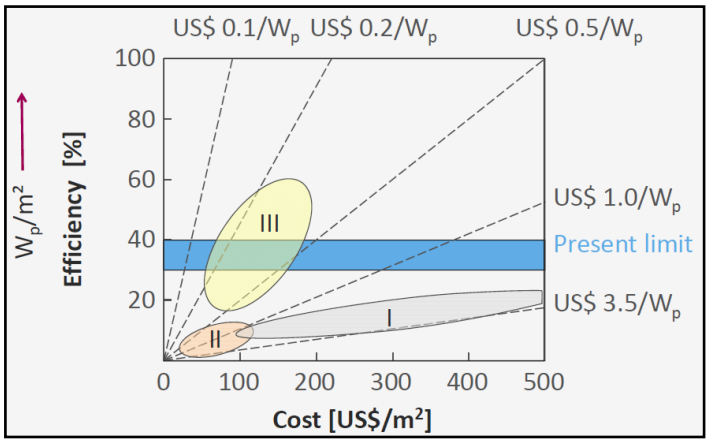

Figure 2-2. Efficiency vs. Cost per m^2. Colored regions show different generations of solar cells (Smets, 2014).

2.1.3 Solar Spectrum

The principal source of energy for solar cells is the Sun whose irradiance spectrum can be compared to that of a black body at 5800K. The graphs in Figure 2-3 illustrate the Spectral Irradiance of the Sun for two different Air Masses[2] (A.M. 0 and A.M. 1.5) and the absorption of some materials: c-Si, a-Si:H and c-Ge. The A.M. 0 Spectrum (before solar radiation crosses the atmosphere) is used in spatial solar cell industry. The A.M 1.5 is the solar radiation that crosses the atmosphere at a latitude of 48.2º (i.e. light from the Sun crosses 1.5 times the atmosphere thickness at the Equator).

[2] The Air Mass coefficient represents the amount of atmosphere the sun light should pass through before striking the device at sea level normalized to the shortest pass length (i.e. when the Sun is at the zenith): A.M= $\frac{1}{\cos\theta}$, where θ is the zenith angle.

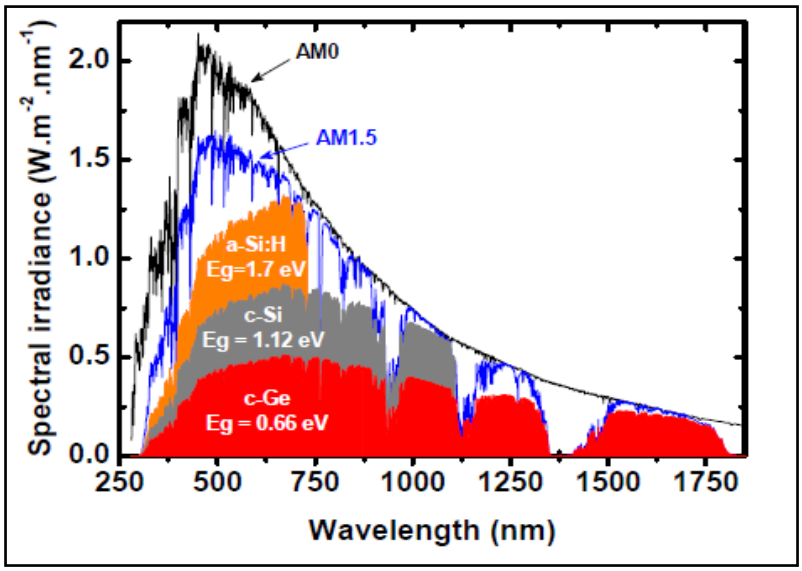

Figure 2-3 . Spectral Irradiance vs. Wavelength for A.M. 0 and A.M. 1.5 and Spectral Absorption of a-Si:H, c-Si and c-Ge (Labrune, 2011)

2.1.4 p-n Junction in dark

The p-n junction is one of the most important part of a Silicon solar cell: that is why this kind of device will be described under thermal equilibrium which means a junction under constant temperature, no generation (not illuminated junction) and no injection (no Bias voltage applied) of charge carriers. This junction is made by two types of semiconductors, an n-doped semiconductor (where majority charge carriers are electrons) and a p-doped semiconductor (where majority charge carriers are holes), as it is shown in Figure 2-4. When they are put together electrons (resp. holes) diffuse from a region with high electron (resp. hole) concentration i.e. the n-region (resp. p-region) to another with low concentration i.e. the p-region (resp. n-region), while donors (positively ionized dopant atoms) and acceptors (negatively ionized dopant atoms) stay fixed in n- and p-region respectively. This region is known as depletion region or space charge region. The presence of positive charges on one side of the depletion region and negative ones on the other side generates an electric field opposing the diffusion of the free charge carriers. At one point, both phenomena will compensate and

equilibrium is reached. In Figure 2-5, a band energy diagram of a homojunction of crystalline Silicon (c-Si) in thermal equilibrium is displayed; the size of the depletion region is $W = W_e + W_b$, with $W_b > W_e$ (because in the figure, the p region is more doped than the n region); V_{bi} is the built-in potential of the junction which is the electric potential resulting from the integration of the electric field across the depletion region.

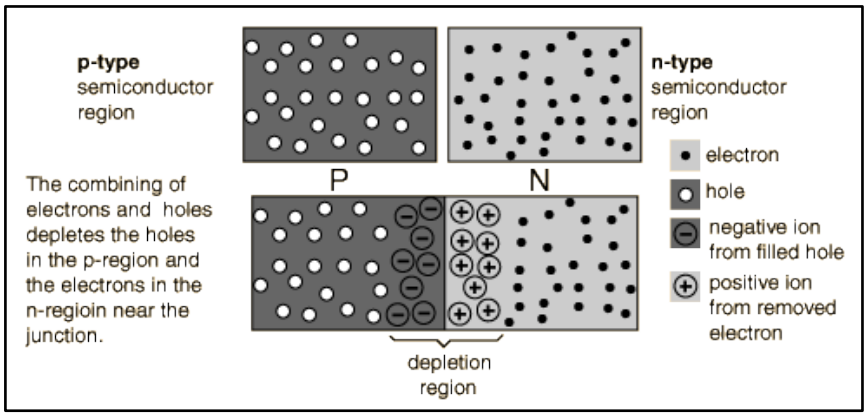

Figure 2-4 . p-n Junction

Under no-illumination conditions, density of current in dark (J_D) in function of applied voltage (V) is then the one of a simple diode and could be written as in eq. (2-1), where J_0 is the diode saturation current and n is the ideality factor ($1 \leq n < 2$). (Labrune, 2011)

$$J_D(V) = J_0 \left[exp\left(\frac{qV}{nkT}\right) - 1 \right] \qquad (2\text{-}1)$$

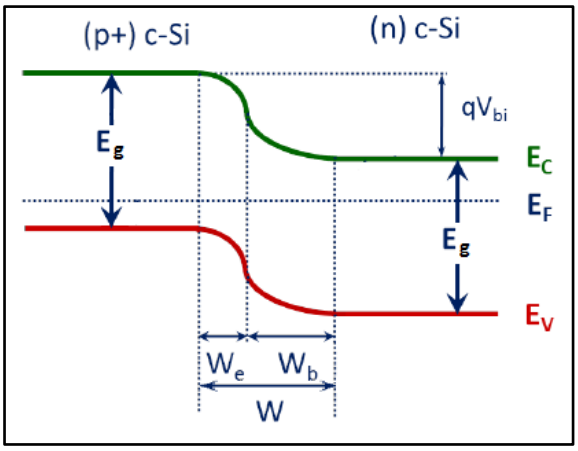

Figure 2-5 . Band diagram of a Homojunction of c-Si. (Labrune, 2011)

2.1.5 p-n Junction under illumination

When a p-n junction is illuminated, the total current is $J = J_D + J_{sh} - J_{ph}$, where J_D is the dark current as defined in eq. (2-1), J_{ph} is the photocurrent generated in the junction, and J_{sh} is the leaking shunt current (Green, 1992).

$$J(V) = J_0 \left[exp\left(\frac{q(V - R_s.J)}{nkT}\right) - 1 \right] + \frac{V - R_s.J}{R_{sh}} - J_{ph} \qquad (2\text{-}2)$$

Where J_0 is the diode saturation current density, V is the voltage applied to the junction, R_s is the series resistance, R_{sh} is the shunt or parallel resistance in the junction and n is the ideality factor. Figure 2-6.A shows a realistic model for the p-n junction under illumination while two diagrams of Current vs. Voltage under dark and illuminated conditions are presented in Figure 2-6.B.

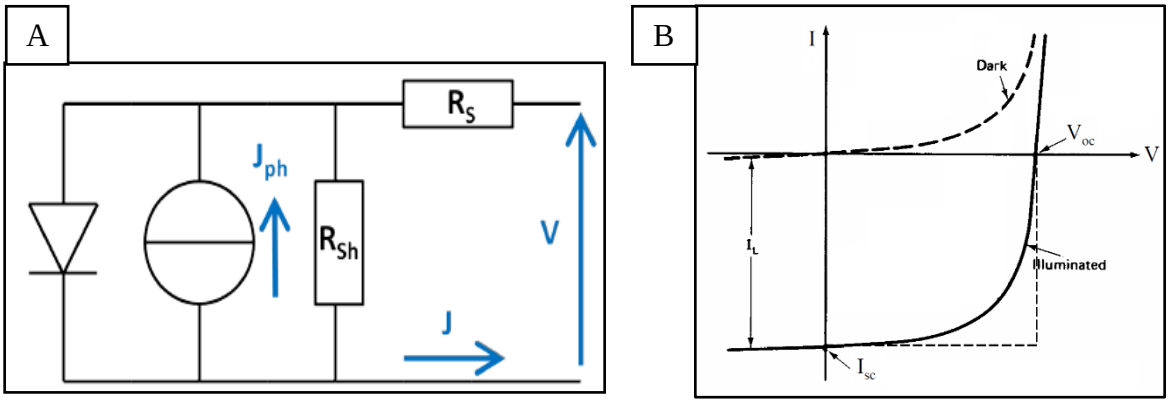

Figure 2-6. A) Realistic Electrical circuit of a p-n junction under illumination; B) Diagram of I vs. V under dark and illuminated conditions (Labrune, 2011)

2.1.6 External Parameters of photovoltaic devices

In sections 2.1.4 and 2.1.5, the principal characteristics of a p-n junction have been mentioned, since this kind of junction is an important component of many photovoltaic devices (such as crystalline silicon solar cells). In this section, some of the critical parameters of a solar cell (see Figure 2-7) will be described, such as:

- Short circuit current density, J_{sc} [$mA.cm^{-2}$]. It is the maximum current density in a solar cell and occurs when the voltage across the device is equal to zero (i.e. when the cell terminals are short-circuited).
- Open circuit voltage, V_{oc} [V]. It is the maximum voltage in a solar cell and occurs when the current across the device is equal to zero (i.e. when the cell terminals are not connected to any circuit).
- Maximum peak power density, P_{max} [$W_{p.}\ cm^{-2}$]. It is the maximum value of the product of J and V. As follows: $P_{max} = J_{MPP} . V_{MPP}$
- Fill factor (FF)[%]. It is the ratio of the area of the dark grey rectangle and the light rectangle in Figure 2-7. It describes the electrical quality of the cell.

$$FF = \frac{P_{max}}{J_{sc} . V_{oc}} = \frac{J_{MPP} . V_{MPP}}{J_{sc} . V_{oc}} \qquad (2\text{-}3)$$

- Efficiency (η)[%]. It is the ratio of the maximum peak power density to the light incident power density.

$$\eta = \frac{P_{max}}{P_{inc}} = \frac{J_{MPP} \cdot V_{MPP}}{P_{inc}} = \frac{J_{sc} \cdot V_{oc} \cdot FF}{P_{inc}} \quad (2\text{-}4)$$

The measurement of these parameters in a solar cell are obtained from the Current-voltage characteristic curve I=f(V) of a solar cell, see Figure 2-7. The measurement of the I-V characteristic curve (I-V curve) is performed under standard test conditions:

- A.M. 1.5 spectrum.
- Irradiance: 1000 $W.m^{-2}$.
- Temperature: 25 °C.

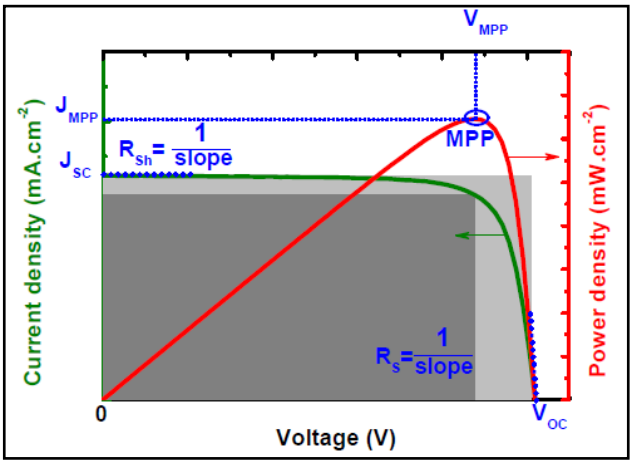

Figure 2-7 . Current density -Voltage characteristic curve of a solar cell. (Labrune, 2011)

2.1.7 Principal Losses in absorption in solar cells

In essence, there are two kinds of losses when light is absorbed by semiconductor solar cells that intrinsically depend on the material used for the solar cell:

1) Photons with less energy than the Band gap energy (E_g) of semiconductor used in the solar cell, cannot be absorbed by the Semiconductor.
2) Photons with larger energy than the band gap of the semiconductor are absorbed by electronic transitions (from the valence band to the conduction band). However, electronic excess energy is dissipated by collisions between electrons and atoms or ions in the crystalline lattice. This process is known as Thermalization.

Apart from these intrinsic losses, there are other loss factors that could be reduced to get a more efficient solar cell, such as:

- Reflection from the front side: It could be reduced using a material with good reflection properties: the reflection depends on the index of refraction of the material and the path geometry of the light. The path geometry is determined by refraction at the front side. For example, wet texturing is a technique used to produce a determined roughness at the front side in order to trap more light into the cell, by enhancing both the optical path length and by diminishing the reflection.
- Shadows from the metal grid: The contacts (fingers and busbars) which are used to collect charge carriers at the front of the solar cell produce many power (current) losses because of the shadowing they cause. A good way to increase the spacing between fingers and then reduce shadowing is by using a TCO with higher conductivity.
- Recombination of charge carriers: when the EHPs are produced in the cell, it is required that most of these carriers should be collected. For that the recombination centers must be reduced at the silicon surface (i.e. chemical passivation of silicon surface with Hydrogen) or in the bulk (i.e. wafer with less defects).

- Parasitic series resistances: this kind of resistance can be resistance in the semiconductor materials, interface resistance between the semiconductor and the metal contacts, resistance of the metal contacts, etc. These resistances produce power losses that can be reduced by improving contact quality, emitter conductivity, less resistive wafer, etc.
- Parasitic parallel resistances: it is generally caused by macroscopic defects. Low parallel (or shunt) resistance provides an alternative path for the photogenerated charges. To limit power losses, the parallel resistance of the cell has to be increased and this can be done by improving edge isolation, junction quality, semiconductor quality without cracks (Smets, 2014).

2.2 Fabrication of HET solar cells

During the internship, two types of HET cells were treated by Excimer Laser Annealing (ELA): the so-called "R&D" and "PILOT LINE" solar cells: the first ones were made in an R&D cluster tool and the second ones in a pre-industrial factory. In this section, only a summary of the fabrication of the R&D HET cells is presented. The procedure to make the PILOT LINE HET cells is similar to the one of R&D cells, except that they are fabricated in an industrial way (mass production).

2.2.1 JUSUNG Equipment

The machine used to produce HET solar cells is a thin-film deposition cluster of the brand JUSUNG Engineering Inc. which is a High Vacuum equipment that allows to deposit different kind of thin films on texturized c-Si wafers as raw material. This equipment has five medium or high vacuum chambers: two Plasma enhanced chemical vapor deposition chambers (PECVD), two Physical vapor deposition chambers (PVD) and one Metal organic chemical vapor deposition at low pressure chamber (MOCVD). In Figure 2-8, the different parts of the JUSUNG machine are shown (Martín, 2012).

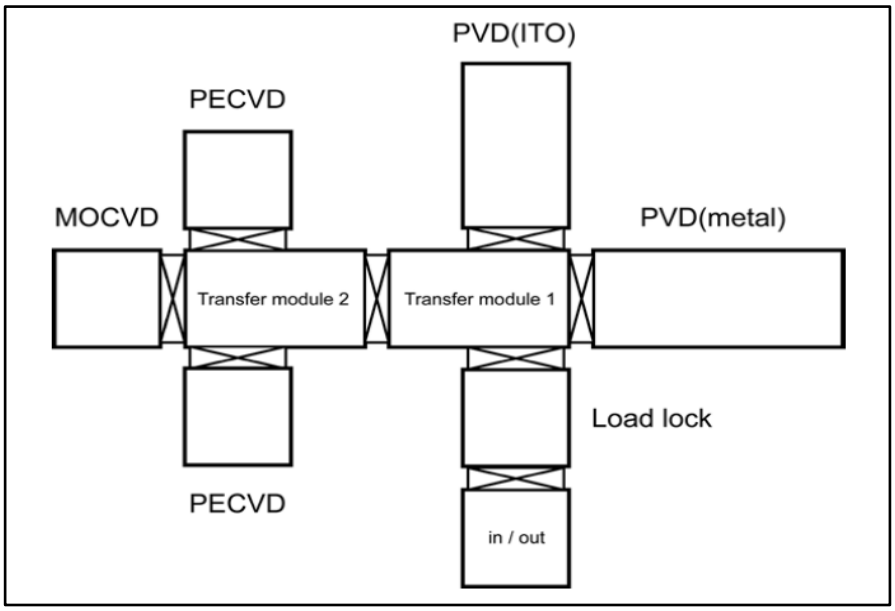

Figure 2-8. Machine JUSUNG used to fabricate HET solar cells. (Martín, 2012)

2.2.2 Procedure of fabrication of bifacial HET solar cells of inverted emitter

Fabrication of Heterojunction solar cell consists of several steps. The principal materials and techniques used to produce the R&D HET cells in the R&D Clean Room, are described in this section (with a little drawing on the right). The order of some steps presented here is not necessarily the same used in real manufacturing or in other laboratories/institutes.

1) Raw Material:

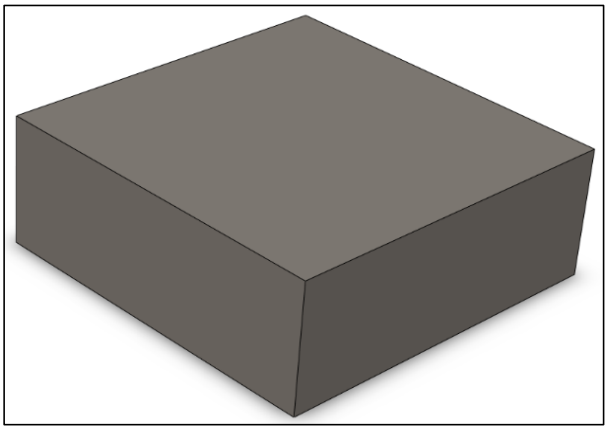

Crystalline Silicon wafers (100) of type n were used to produce HET cells. These wafers have a Resistivity of 1-5 Ω.cm, a Thickness of ~180 µm and a Surface of 149 cm^2 (pseudo-square 12.5 cm x 12.5 cm)

2) Surface texturing (wet chemical etching):

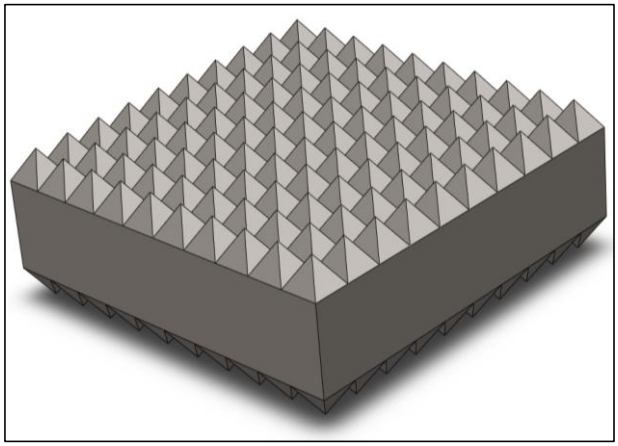

KOH solution is utilized to texture the silicon surface, hence superficial pyramids appear. The planes of the pyramids are orientated in the direction (111), have ~10 nm height and allow both to reduce the external reflection of the light and to improve the light confinement into the cell. This way, more light can be absorbed. By removing the first 10-20 µm on each side of the wafer, this step also permits to remove the highly defective regions resulting from the wafer sawing process. Afterwards a RCA (Radio Corporation of America) cleaning is made, followed by a quick immersion in hydrofluoric acid (HF), to remove the native silicon oxide at the surface and to ensure a momentary passivation creating Si-H bonds at the surface right before the first a-Si:H thin films are deposited.

3) Intrinsic Thin layer: undoped hydrogenated amorphous Silicon [a-Si:H (i)] deposition: (Orange color)

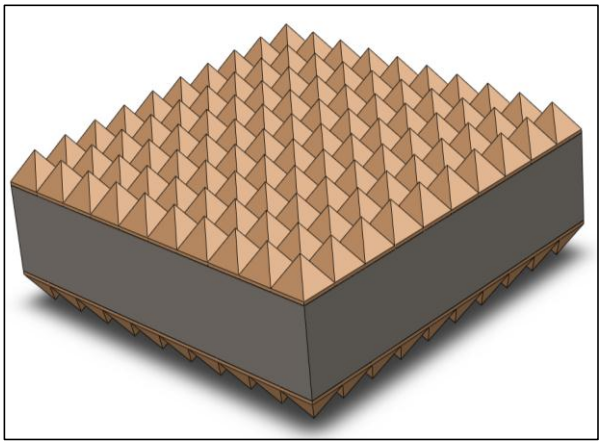

The thin layers of a-Si:H(i) [~5 nm] are deposited with the PECVD technique in the JUSUNG equipment at ~200 °C. The thickness is about 5-10nm. These a-Si:H (i) layers which are deposited onto the front and back side of the wafer, ensure a very good passivation of the surface of the c-Si(n). Its very small thickness allows the passing of electrons to the a-Si:H(n) layer at the front side and the passing of holes to the a-Si:H(p) layer at the back side.

4) N-doped hydrogenated amorphous silicon [a-Si:H (n)] thin film deposition (Front Surface Field - FSF): (Blue color)

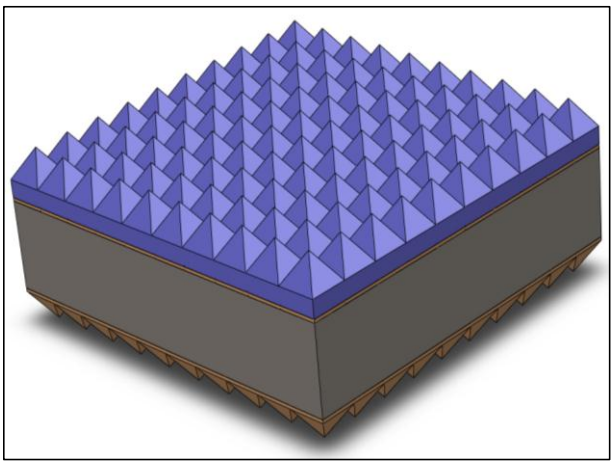

The a-Si:H(n) thin film [of a few nm] is deposited by PECVD onto the intrinsic thin layer of a-Si:H. Doping is made with PH_3 gas. Its role is to repel the minority carriers (holes) by creating an electric field between the c-Si substrate and the a-Si:H (n) layer. This so-called Front Surface Field (FSF) thus it prevents the recombination of holes at the front surface by keeping them away from it.

5) P-doped Hydrogenated amorphous silicon [a-Si:H(p)] thin-film deposition (emitter):
(Turquoise color)

PECVD is used to make the a-Si:H(p) thin film[of a few nm] at the back side of HET solar cell. This a-Si:H (p) film and the c-Si(n) make the pn-heterojunction which is the core of the solar cell functioning.

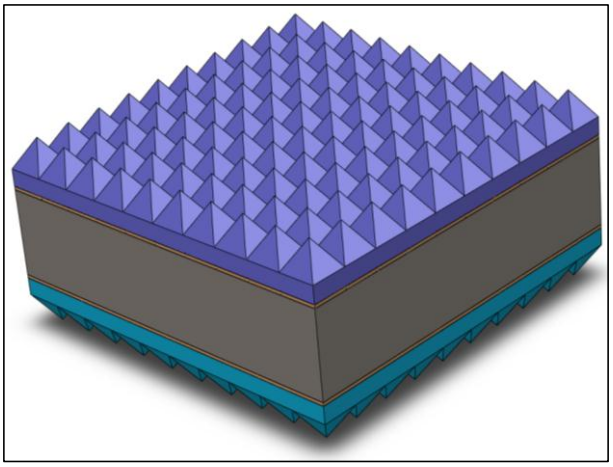

6) ITO thin film deposition:
(Red color)

ITO thin film [~100 nm] was made by PVD, more precisely by magnetron sputtering, also in the JUSUNG equipment. The a-Si:H is not a good electrical conductor and it does not act as anti-reflective coating, that is why HET solar cells must have another film to overcome these constraints. ITO is a transparent conducting oxide: with adequate deposition conditions and thickness it can act as anti-reflective coating on silicon, show high transparency and high electrical conductivity.

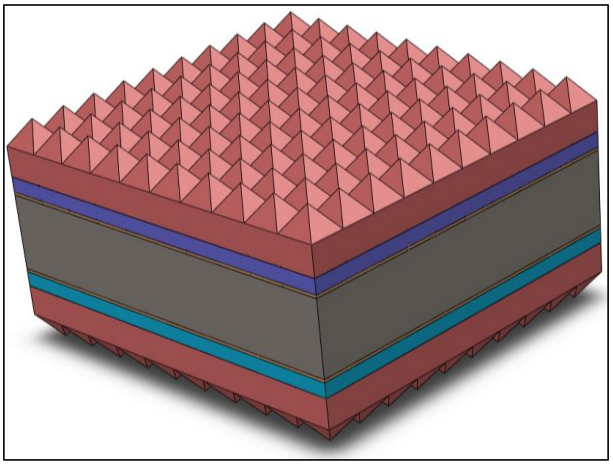

7) Metallic grid deposition:
(Grey color)

Finally, a metallic grid [few tens of µm thick] is deposited onto both faces of the solar cell. Aluminum or Silver inks are deposited by screen printing. This solar cell configuration is called 'bifacial' because it can absorb light from both sides. At the front side, it receives the solar radiation from the Sun and at the rear side, it receives reflected light from external neighboring surfaces.

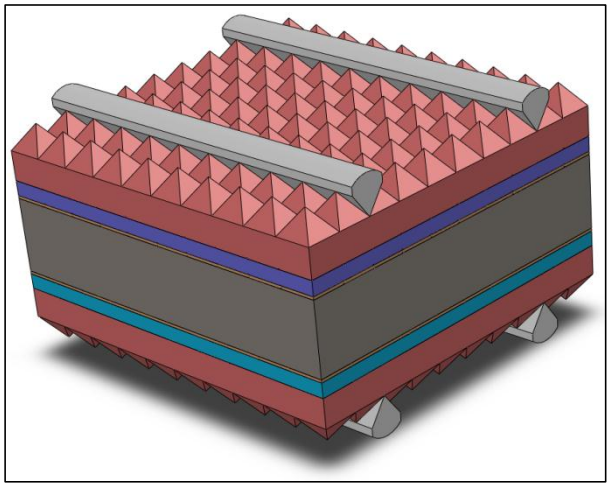

2.2.3 Inverted and standard emitter HET solar cell

At LHET, two different kinds of HET solar cell are fabricated: The inverted emitter and the standard emitter solar cell. The difference is only the position of the emitter used in each solar cell. Standard emitter solar cells have the a-Si:H (p) emitter at the front side, while for inverted emitter solar cells it is at the back side. In other words, the 'p-n heterojunction' is at the rear side for inverted emitter HET solar cell and at the front side for the standard emitter HET solar cell, as it is presented in Figure 2-9. During this internship, only HET solar cells with inverted emitter were treated by ELA.

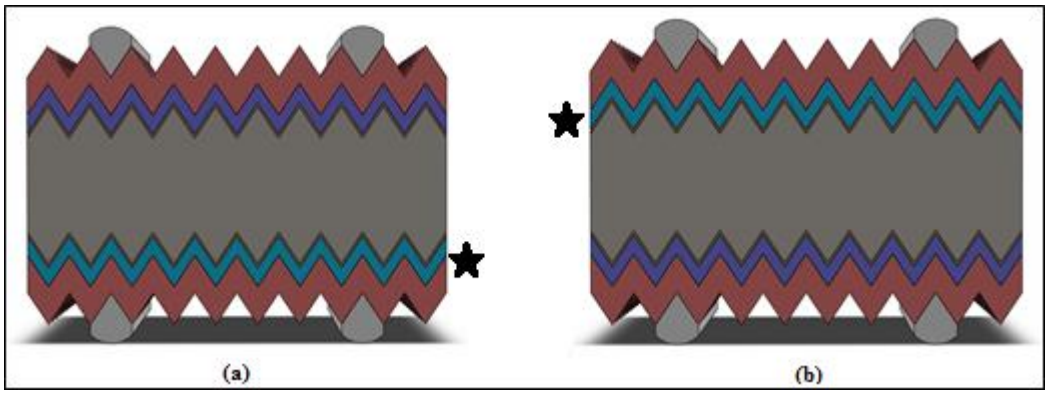

Figure 2-9. Stars in the figure point up the position of the emitter layer. A) HET solar cell with inverted emitter, the a-Si:H(p) is at the rear side. B) HET solar cell with standard emitter, the a-Si:H(p) at the front side.

2.3 HET solar cell

In the previous sections, the principal characteristics of solar cell have been described and the main steps of the fabrication of a crystalline silicon HET solar cell have been mentioned as well. In this section, some of the crucial characteristics of a crystalline silicon HET solar cell are presented. HET solar cells with intrinsic amorphous thin layer or abbreviating HIT® Solar cells (heterojunction with intrinsic thin layer) were designed by SANYO in the early 90s (Panasonic, 2014). The Figure 2-10 shows the principals parts of a HIT solar cell with inverted emitter. From now and on, the term "amorphpous /crystalline silicon HET solar cell" or simply HET solar cell will be used to refer to a HIT® solar cell.

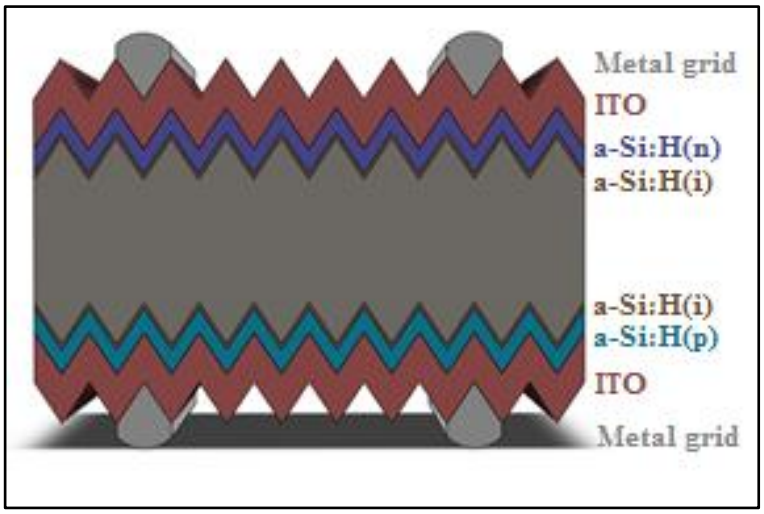

Figure 2-10. Parts of a HET solar cell with inverted emitter.

2.3.1 Operation of a HET solar cell

A model used to describe a real HET solar cell is the two-diode model whose equivalent circuit and can be seen in Figure 2-11.A. The current density-voltage characteristic curve of the two-diode model can be presented as (Green, 1992):

$$J(V) = J_{01}\left[exp\left(\frac{q(V - R_s.J)}{n_1 kT}\right) - 1\right] + J_{02}\left[exp\left(\frac{q(V - R_s.J)}{n_2 kT}\right) - 1\right] + \frac{V - R_s.J}{R_{sh}} - J_{ph} \quad (2\text{-}5)$$

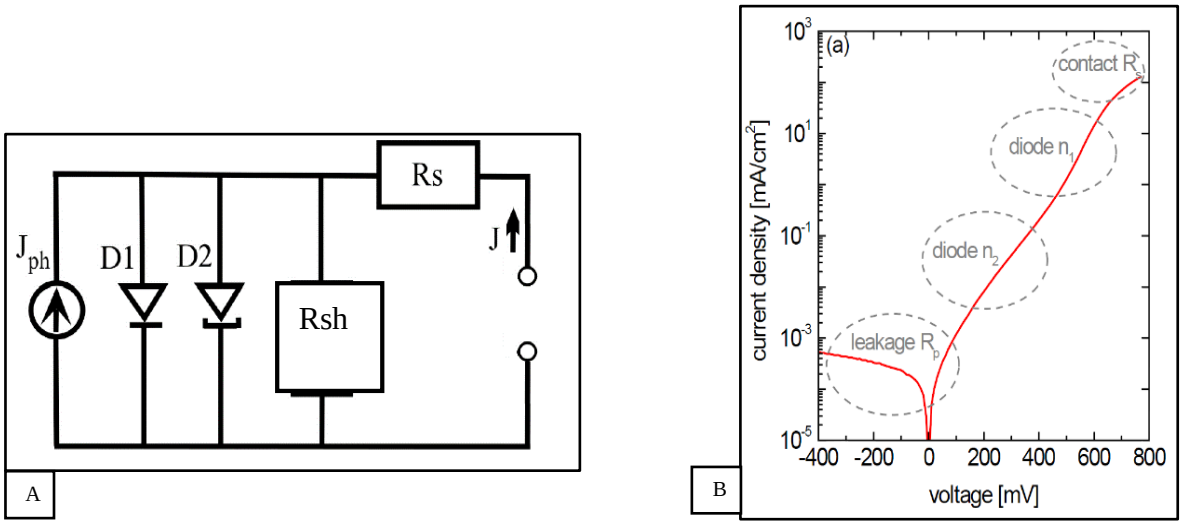

Figure 2-11. A) Equivalent Circuit for two diode model of a real solar cell with series and shunt resistance. B) Dark current density - voltage characteristic curve of a HET solar cell. (Martín, 2012)

Where J_{01}, J_{02} are diodes saturation current densities, V is the voltage applied to the junction, R_s is the series resistance, R_{sh} is the shunt or parallel resistance and n_1 and n_2 are the 2 diodes ideality factors. A current density-voltage curve measured in dark is shown in Figure 2-11.B and can be related to eq. (2-5) without illumination, i.e. $J_{ph}=0$ (no generated photocurrent). The main diode (D1) gives information about the diffusion current in the p-n junction at high-forward Bias; its impact is primarily on the V_{oc} parameter and its ideality factor n_1 is between 1 and 2. The second diode (D2) becomes important at moderate Bias (see Figure 2-11.B), gives information about the space charge region (recombination and tunneling); it has an impact on the FF parameter, the smaller J_{02} the better FF, with an ideality factor >2.5 for HET devices.

R_s resistance appears because of the resistance of bulk silicon wafer, metallic contacts (on the front and rear surface), contact resistance at interfaces between metallic contacts and ITO layers and other connections and terminals. R_{sh} resistance appears because of the leakage across the p-n junction due to non-idealities and impurities near the junction, causing a partial short circuit in the junction (near the edges of the cell); parallel or Shunt resistance can be observed (Figure 2-11.B) under reversed Bias and at very low forward Bias. For example, if the edge isolation was not properly made, the front and rear side of the cell will be contacted, producing decrease in R_{sh}, which leads in a change of J(V) curve. To have an efficient solar cell, R_s must be very low and the value of R_{sh} must be as high as possible.

2.3.2 Band diagram of a HET solar cell

A hydrogenated amorphous/crystalline silicon HET solar cell results from the joining of thin films of hydrogenated amorphous silicon with a crystalline silicon wafer. The amorphous silicon has a band gap of $E_g = 1.75$ eV and the crystalline silicon has a band gap of E_g=1.12 eV at 300K, thus giving its name to the cell (heterojunction: different band gaps). In Figure 2-12, a band diagram of a HET solar cell is shown.

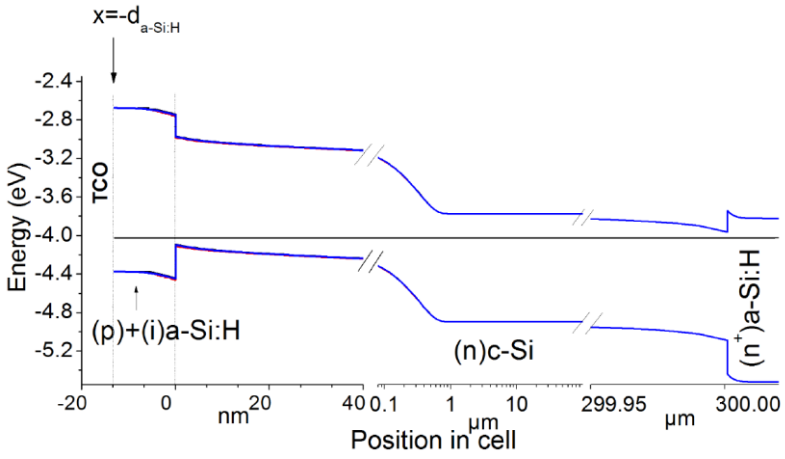

Figure 2-12. Band diagram of a TCO/a-Si:H(p)/ a-Si:H(i)/c-Si(n)/a-Si:H(n) solar cell calculated with AFORS-HET[3] (Varache, 2012)

The thin layer of intrinsic hydrogenated amorphous silicon (a-Si:H(i)) is utilized in a HET solar cell for two reasons:

1. Good defect passivation of the crystalline silicon surface of the wafer (type n), avoiding recombination of charge carriers at the a-Si:H/c-Si interface. As a consequence, the charge carrier lifetime is enhanced (Smets, 2014).

2. The band discontinuities at the a-Si:H/c-Si interface make a blocking layer for holes and electrons thus allowing field effect passivation.

When photons arrive onto the HET solar cell (coming from left to right in Figure 2-12), they are absorbed in the c-Si(n) substrate, creating EHPs. Electrons are forced towards the n-type amorphous silicon layer (on the right), and holes go into the direction of the p-type amorphous silicon layer (on the left). Electrons are carried to the a-Si:H(n) layer as well as holes are drifted

[3] Automate FOR Simulation of HETerostructures is a simulation software used at the Helmholtz-Zentrum Berlin and it is free on demand.

to the a-Si:H(p) through the a-Si:H(i) layers by the strong electric field at the interfaces [a-Si:H(i)/c-Si(n) and c-Si(n)/a-Si:H(i)]. It is known amorphous silicon cannot transport the photogenerated charge carriers to the metallic grid efficiently due to its low electrical conductivity. As a consequence a material like ITO (or other kind of TCO) must be added onto the amorphous silicon layers. Finally, the photogenerated charge carriers are conducted through ITO to be finally delivered into the metal fingers of the solar cell.

2.3.3 Advantages and perspectives in HET solar cells

Nowadays, HET solar cells are being integrated into many buildings and housing constructions to generate clean electricity. Some advantages of the HET solar cells are the following:

- High open-circuit voltage values (see Table 2-1). Thanks to high passivation at the amorphous/crystalline silicon interface (resulting in a higher charge carrier lifetime).
- Low-cost deposition processes such as the utilization of PECVD with temperatures under 200°C (low thermal budget).
- Better performance at higher temperatures thanks to a lower temperature coefficient than conventional homojunction solar cells.

Table 2-1. Values of the principal external parameters of a record HET solar cell at INES (Muñoz D. , 2012).

External Parameter	Value
V_{oc} (V)	0.733
J_{sc} (mA.cm^{-2})	38.7
FF	78.5
Efficiency	22.2
c-Si(n) thickness (µm)	~150
Area (cm^2)	103

Some of the perspectives for the HET solar cells, particularly regarding the transparent electrodes, are the following:

- Improvement of electrical conductivity and optical transparence of the TCO either by using higher-performing material than ITO or by using novel approaches to improve ITO like ELA which is the principal motivation of this internship.
- Replacement of ITO in the middle term by cheaper materials such as AZO since the cost of ITO is very high and continues to increase due to indium scarcity.

3 EXCIMER LASER ANNEALING (ELA)

Excimer laser is a tool which is widely used in refractive correction surgery. The term excimer refers to an excited dimer as Ar_2*, Kr_2*, Xe_2*, etc; whereas exciplex refers to an excited complex such as ArF*, KrF*, XeCl*, etc. In our case, an exciplex laser made of XeCl was utilized to anneal the ITO thin films in HET solar cells. The term excimer is used in this manuscript even though the correct term is exciplex, because ELA technique is usually cited in literature for both kinds of lasers. In this chapter, the principle of work of an excimer laser is described followed by a description of the state of the art of recent research, then the complete list of the laser treatments made is presented as well.

3.1 XeCl Excimer Laser

The XeCl excimer EXCICO® laser (λ = 308 nm) is a laser with wavelength of 308 nm (4.03 eV). In this section, first of all, the functioning of a laser is described and then different steps of producing light with the excimer laser are analyzed.

A laser is a source of monochromatic (same color or same wavelength) and coherent (same direction) light. The principal parts of a laser are shown in

Figure 3-1:

- Gain Medium which produces the amplification of photons (photon emission) by stimulated emission. The gain medium can be a gas or a solid material where its electrons can occupy the levels of energy E_1 or E_2 (E_2>E_1).

- Laser pumping energy which is the energy necessary to excite constantly the gain medium and to ensure that the gain medium may amplify light.
- Laser cavity (optical reflectors).

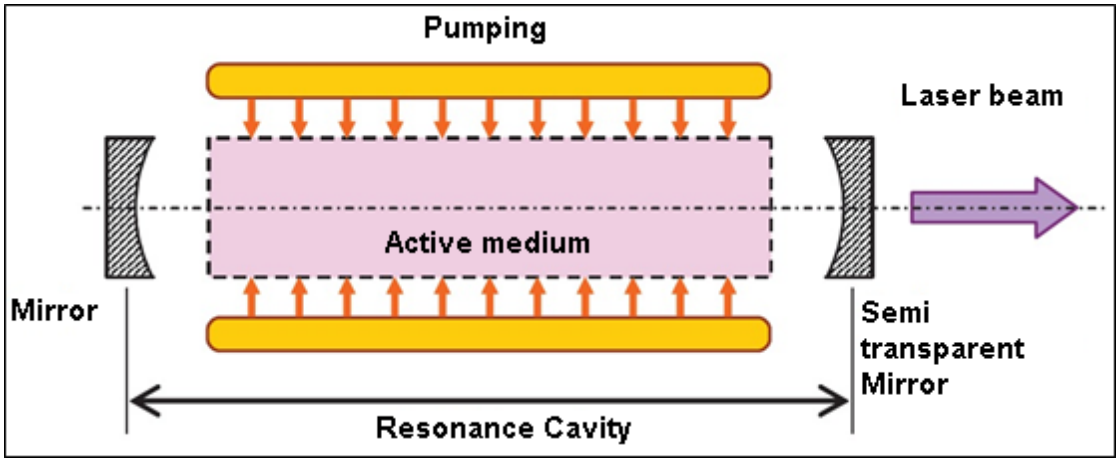

Figure 3-1. Schema of the principal parts of a laser.

An electronic transition occurring between two levels of energy can be due to absorption or emission (stimulated or spontaneous) of a photon. This photon has energy equal $h\nu=E_2-E_1$. Three different electronic transitions are depicted in Figure 3-2.

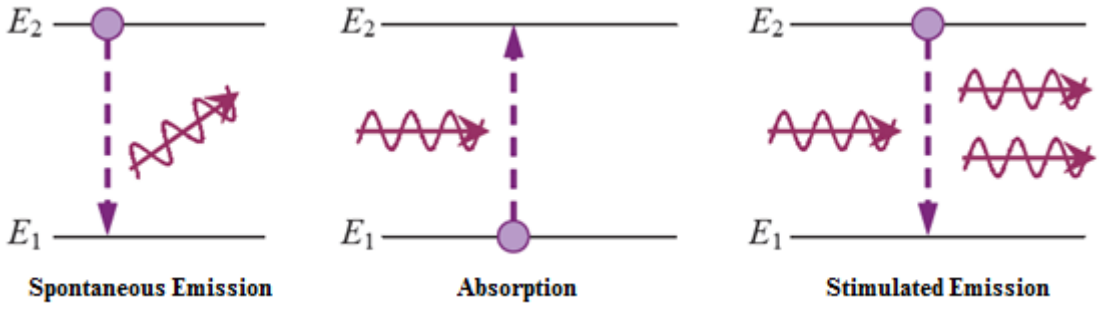

Figure 3-2. Different kinds of electronic transitions that may occur in the gain medium.

The spontaneous emission is produced for example in a mercury discharge lamp whose emission spectrum is composed by many wavelengths. These wavelengths are produced by different electronic transitions resulting in light waves with random directions. The spontaneous emission is not the primary source of light in a laser system. The stimulated emission is produced when a higher number of the electrons of the gain medium are in an excited state (E_2) rather than in the lower energy level (E1): we have then a "population inversion". These electrons interact with incident photons of certain energy, producing electronic transitions to a lower level of energy (E_1) and emitting extra photons. That is why the stimulated emission amplifies the incident photons of the gain medium, as it is shown in Figure 3-2.C. The energy and momentum of these emitted photons are the same (Legeay, 2011).

The gain medium of the XeCl excimer laser is composed by a mixture of gazes at a pressure of 2.8 bars with Neon ~99%, Xenon 0.5 %, HCl 0.05 %, H_2 0.02 %. The main parts of an excimer laser are shown in Figure 3-3.

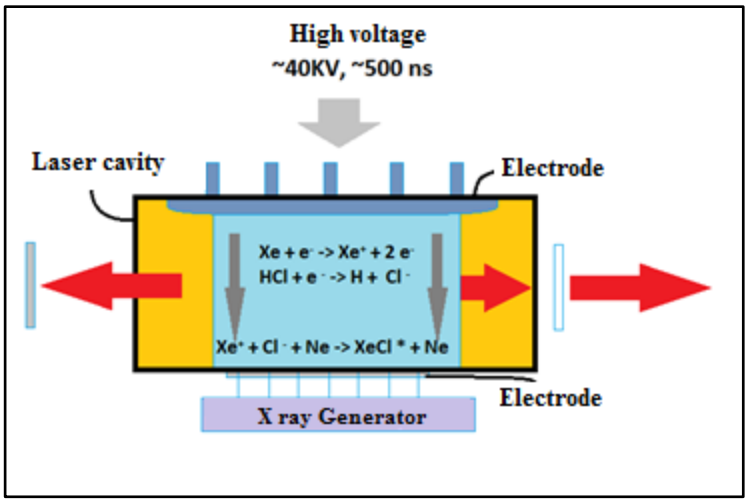

Figure 3-3 Main parts of Excico laser Cavity.

The generation of light with a wavelength of 308 nm with the excimer laser involves the following steps (see Figure 3-4):

1) Since Xenon gas is a noble gas and is very difficult to ionized, X-rays are injected in the laser cavity to ionized Xenon atoms and create electrons.
2) Then, a pulsed high voltage (~40KV, ~500 ns) is applied between electrodes (see Figure 3-4.A) to create different ions in the gas mixture:

$$Xe + e^- \rightarrow Xe^+ + 2e^-$$
$$HCl + e^- \rightarrow H + Cl^-$$

3) Next, the Xe+ and Cl- react to form XeCl* (excited state), as follows:

$$Xe^+ + Cl^- \rightarrow XeCl^*$$

4) Last, the laser light comes out when the the XeCl* molecule transits to its fundamental state i.e. XeCl. However, the XeCl molecule is unstable and immediately dissociates in its primary components.

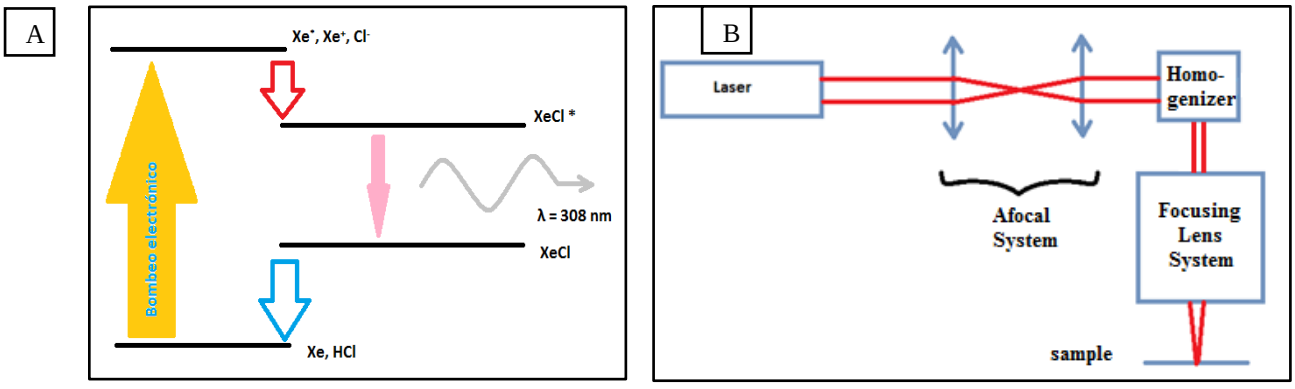

Figure 3-4.A) Schema of the principal steps to produce light in the excimer laser. B) Parts of the optical system which are used to focalize the laser light.

The light which is produced in the gain medium passes through an optic system as indicated in Figure 3-4.B. The afocal system ensures the total divergence of all the light coming from the laser cavity. Then this light goes through the homogenizer which eliminates many of the irregularities of the laser beam and finally, the focus concentrates the light to treat the surfaces.

3.2 State of the Art in ELA

Various research groups have studied excimer laser annealing as a method to get better quality of TCOs such as ITO and AZO. In this section, some of these works are discussed:

Martín de Nicolás *et al.* studied the influence of laser annealing onto ITO thin films at different laser fluences. ITO thin films were deposited by DC sputtering at different oxygen (Φ_0) flows and T_{dep}=180°C. The square resistance of 90 nm thin films (Φ_0=2.5%) on Corning glass substrate was sharply decreased from 500 $\Omega.\square^{-1}$ to 8 $\Omega.\square^{-1}$ with almost no changes in the index of refraction for energy densities from 0 to 350 mJ.cm^{-2}. While XRD analysis showed that ITO thin films have initially two preferential directions (111) and (100), after the ELA, it can be seen that these directions don't coexist anymore with an increment of (111) direction. ITO/a-Si:H/c-Si precursors were also fabricated to study the passivation quality by Quasi-steady state photoconductance (QSSPC): no degradation in V_{OC} was observed for laser fluences lower than 200 mJ.cm^{-2}. Last, Heterojunction solar cells with ITO thin films as charge carrier collector were annealed with laser fluences up to 150 mJ.cm^{-2}: data showed that no change in performance occurred (Martín de Nicolás, 2012). Another work on thin film ELA of ITO for flexible display was done by Chung *et al*: Square resistance of ITO thin films were decreased from 191 to 25 $\Omega.\square^{-1}$for laser fluences from 0 up to 150 mJ.cm^{-2}, the optical transmittance in visible increased from 70 to 85% in the same range of used energy densities (Chung, 2004).

Johnson *et al*. have demonstrated the effect of ELA on 1 µm AZO films deposited by RF sputtering at Room temperature. They observed an improvement in transparency (optical properties) for optimized laser fluences of 500-700 $mJ.cm^{-2}$ with no changes in conductivity (constant electrical properties) for AZO films deposited on Corning Eagle glass. They also prepared hydrogenated microcrystalline silicon pin solar cell whose photocurrent density (up to 2.2 $mA.cm^{-2}$) was increased after the AZO thin films were laser annealed with optimized laser fluences and chemically etched (Johnson, 2011). Boukhicha *et al.* explored the influence of thin film laser annealing on 1µm opaque AZO films deposited by RF at different pressures and oxygen flows. After optimal laser annealing (700 $mJ.cm^{-2}$), Transmission increased from 70 to 80 % in range of photovoltaic interest, however only low pressure and low oxygen-content samples maintained acceptable electrical properties after etching process ($< 11\ \Omega.\square^{-1}$) (Boukhicha, 2014). Charpentier *et al.* combined ELA with chemical etching texturing (LaText process) on Room Temperature sputtered AZO thin films. Above 500 $mJ.cm^{-2}$, AZO thin films have domains separated by cracks. A subsequent etching step removes material from the cracks leading to an increase of the resistivity. However some samples retained an acceptable sheet resistance ($< 15\ \Omega.\square^{-1}$). When LaText is introduced into a-Si:H and µc-Si:H device structures, it significantly reduced reflectivity, allowing better light trapping (Charpentier, 2014).

3.3 ELA treatments

Excimer laser annealing (ELA) was performed on several samples. The ELA treatments can be separated in three groups: Study of ITO properties after ELA, study of external parameters in HET solar cells after ELA and study of AZO and IOH properties after ELA. The energy densities which are used in ELA are listed in the tables below. The spot of the excimer laser of the Brand Excico (XeCl, 308nm and 150 ns) was ~ 15 ± 2 mm^2.

ITO was deposited onto Corning glass [ITO/g] and silicon substrate [ITO/Si] in order to study its properties before and after laser annealing. The glass substrates had dimensions 25 x 25mm [ITO/g] whereas the Silicon substrates were of different size (two or three times bigger than the laser spot and manufactured by Czochralski Method) since they were small pieces of a c-Si(n) wafer (100) [ITO/Si]. To measure the change in sheet resistance due to different ELA energies or to repetitive pulses with the same energy density, different ELAs were tested (see Table 3-1 and Table 3-2). The laser annealed ITO/g samples were characterized by Hall Effect measurement, spectrophotometry and four point probe measurement. The laser-annealed ITO/Si samples were characterized by Ellipsometry. SEM observations were also made in ITO/g and ITO/Si samples to observe changes in microstructural characteristic of thin films surfaces. ITO/g and ITO/Si samples were deposited by magnetron sputtering with the same parameters in ITO PVD chamber of the JUSUNG system (see Figure 2-8). Consequently the initial optical and electrical properties are similar in all samples. The different ELAs for ITO/g and ITO/Si are summarized in Table 3-1 and Table 3-2. To measure the impact of ELA on amorphous silicon, some precursors (IP-ITO) of ITO/a-Si:H(p)/ a-Si:H(i)/c-Si (n)/a-Si:H(i) were prepared to perform passivation measurements. The different ELAs applied to these precursors are presented in Table 3-3.

R&D solar cells (R-x) were manufactured in the R&D clean room at INES with the steps described in section 2.2.2, with a surface of 12.5 x 12.5 cm (pseudo-square). Pilot line solar cells

(LF-x) were fabricated in a semi-industrial factory also at INES with a surface of 15.6 x 15.6 cm (pseudo square). The different ELAs applied to these HET solar cells are summarized in Table 3-4 and Table 3-5.

AZO samples were deposited on glass (AZO/g) and silicon substrates (AZO/Si). AZO/g and AZO/Si were prepared by magnetron sputtering in one of the PVD chambers of the JUSUNG equipment; samples with two different thicknesses (100 nm and 300 nm) were submitted to laser treatment. The different ELAs applied AZO/g and AZO/Si are showed in Table 3-6 and Table 3-7.

IOH samples were deposited on glass (IOH/g) and silicon substrates (IOH/Si). IOH/g and IOH/Si were prepared by magnetron sputtering with an Indium oxide target in an Ar:H atmosphere at room temperature (RT) and at 150°C. These samples were made at LETI-Grenoble. The different ELAs applied to IOH/g and IOH/Si are summarized in Table 3-8,

Table 3-9 and Table 3-10.

3.3.1 ELA treatments for ITO

Table 3-1. Energy densities applied to ITO/g and ITO/Si.

SAMPLE		Energy Density ($mJ.cm^{-2}$)
ITO/g-1	ITO/Si-1	100
ITO/g-2	ITO/Si-2	50
ITO/g-3	ITO/Si-3	150
ITO/g-4	ITO/Si-4	200
ITO/g-5	ITO/Si-5	250
ITO/g-6	ITO/Si-6	300
ITO/g-7	ITO/Si-7	350
ITO/g-8	ITO/Si-8	400
ITO/g-9	ITO/Si-9	450
ITO/g-10	ITO/Si-10	500
ITO/g-11	ITO/Si-11	75
ITO/g-12	ITO/Si-12	125
ITO/g-13	ITO/Si-13	175
ITO/g-14	ITO/Si-14	225
ITO/g-15	ITO/Si-15	275
ITO/g-16	ITO/Si-16	325

Table 3-2. Energy densities applied to ITO /g and ITO/Si for repetitive pulses.

SAMPLE		Energy Density ($mJ.cm^{-2}$)
ITO/g-17	ITO/Si-17	2 x 50[4]
ITO/g-18	ITO/Si-18	2 x 100
ITO/g-19	ITO/Si-19	4 x 50
ITO/g-20	ITO/Si-20	3 x 100
ITO/g-xi_01	ITO/Si-xi_01	2 x 300
ITO/g-xi_02	ITO/Si-xi_02	3 x 300
ITO/g-xi_03	ITO/Si-xi_03	5 x 300
ITO/g-xi_04	ITO/Si-xi_04	7 x 300
ITO/g-xi_05	ITO/Si-xi_05	10 x 300
ITO/g-xi_06	ITO/Si-xi_06	2 x 250
ITO/g-xi_07	ITO/Si-xi_07	3 x 250
ITO/g-xi_08	ITO/Si-xi_08	5 x 250
ITO/g-xi_09	ITO/Si-xi_09	7 x 250
ITO/g-xi_10	ITO/Si-xi_10	10 x 250

[4] In red, the number of ELA treatments with the same Energy Density.

3.3.2 ELA treatments for R&D and Pilot line cells

Table 3-3. Energy densities applied to IP-ITO precursors

SAMPLE	Energy Density ($mJ.cm^{-2}$)
IP-ITO-1	100
IP-ITO-2	100
IP-ITO-3	200
IP-ITO-4	425
IP-ITO-6	500
IP-ITO-7	300
IP-ITO-8	400
IP-ITO-5	2 x 400
	3 x 400
	5 x 400

Table 3-4. Energy densities applied to front and rear side of PILOT LINE HET solar cells.

SAMPLE	Front ($mJ.cm^{-2}$)	Rear ($mJ.cm^{-2}$)
LF-15	100	-
LF-13	-	100
LF-12	200	-
LF-11	-	200
LF-10	300	-
LF-9	-	300
LF-8	400	-
LF-7	-	400
LF-6	500	-
LF-5	-	500
LF-4	100	100
LF-3	200	100
LF-2	100	300
LF-1	100	200

Table 3-5. Energy densities applied to front and rear side of R&D HET solar cells.

N°	Front ($mJ.cm^{-2}$)	Rear ($mJ.cm^{-2}$)
R-9	-	100
R-8	150	-
R-7	-	150
R-6	200	-
R-4	-	200
R-3	250	-

3.3.3 ELA treatments for AZO and IOH

Table 3-6. Energy density applied to AZO-100nm/g and AZO-100nm/Si.

SAMPLE		Energy Density ($mJ.cm^{-2}$)
AZO-100nm/g-89	AZO-100nm/Si-89	400
AZO-100nm/g-105	AZO-100nm/Si-105	300
AZO-100nm/g-112	AZO-100nm/Si-112	200
AZO-100nm/g-113	AZO-100nm/Si-113	100

Table 3-7. Energy density applied to AZO-300nm/g and AZO-300nm/Si.

SAMPLE		Energy Density ($mJ.cm^{-2}$)
AZO-300nm/g-114	AZO-300nm/Si-114	400
AZO-300nm/g-115	AZO-300nm/Si-115	300
AZO-300nm/g-116	AZO-300nm/Si-116	200

Table 3-8. Energy density applied to IOH-RT/g and IOH-RT/Si.

SAMPLE	Energy Density ($mJ.cm^{-2}$)
IOH-RT/g-21	300
IOH-RT/g-161	100
IOH-RT/Si-2.1	300
IOH-RT/Si-2.2	400
IOH-RT/Si-2.3	500
IOH-RT/Si-2.4	600

Table 3-9. Energy density applied to IOH-RT/SiO_2/Si.

SAMPLE	Energy Density ($mJ.cm^{-2}$)
IOH-RT/SiO_2/Si-4.1	300
IOH-RT/SiO_2/Si-4.2	200
IOH-RT/SiO_2/Si-4.3	50
IOH-RT/SiO_2/Si-4.4	100

Table 3-10. Energy density applied to IOH-150°C/g and IOH-150°C/Si.

SAMPLE	Energy Density ($mJ.cm^{-2}$)
IOH-150°C/g-201	100
IOH-150°C/Si-1.1	300
IOH-150°C/Si-1.2	400
IOH-150°C/Si-1.3	500
IOH-150°C/Si-1.4	600
IOH-150°C/Si-1.5	700

4 CHARACTERIZATION OF ITO AND OTHERS TCOS TREATED BY ELA

In this chapter, a summary of physical properties of ITO will be presented, then the equipment that was used to characterize the samples is described and the results and observations are shown at the end.

4.1 tin-doped indium oxide or ITO

Tin-doped Indium Oxide or more commonly called Indium Tin Oxide (ITO) is a transparent conducting oxide and has been studied for more than 30 years primordially for its use as transparent electrode. It has been widely used in industry to fabricate electronic devices such as liquid crystal screens, photodiodes, antistatic coatings, photovoltaic solar cells, etc. The indium is a rare element on earth and its extraction is more and more expensive. The boom of flat screens has almost depleted the mineral deposits: this fact increased prices from 70$/Kg in 2001 to 1000$/Kg in 2006 and 600$/Kg in 2010 (Edison Investment Research, 2014). One of the materials that could be used as a substitution for ITO because of its similar physical properties is Aluminum doped Zinc Oxide (ZnO:Al or commonly called AZO). At INES, AZO is still at research level.

ITO can be prepared by many techniques such as isostatic pressing, physical vapor deposition (PVD), chemical vapor deposition (CVD), pyrolysis, sol-gel deposition, etc. At INES, ITO is prepared by magnetron sputtering with specified conditions to minimize absorption in the visible range of solar spectrum, as can be seen in Figure 4-1 (extinction coefficient is a good indicator of absorption).

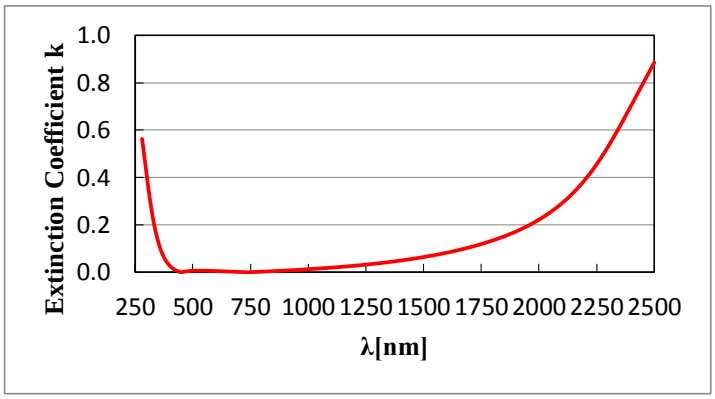

Figure 4-1. Extinction Coefficient for ITO prepared at INES vs Wavelength

4.1.1 Physical Properties

Indium Oxide as a bulk material is yellow and has a fusion point of 1913°C. It has a bixbyite structure (space group Ia3) which has a centered cubic structure with 80 atoms.

ITO is an n-doped degenerate semiconductor with a direct band gap of 3.5 - 4.3 eV. In a degenerate semiconductor the Fermi level is inside the conduction band: in this way ITO has a quasi-metallic behavior. ITO is a degenerate semiconductor thanks to two main doping mechanisms: the vacancies of oxygen and the substitution of Indium by Tin. Therefore, free charge carriers are produced by the vacancy of a divalent oxygen (getting 2 electrons) and the replacement of a trivalent ion (In3+) by a tetravalent ion (Sn4+) (getting 1 electrons).

The high conductivity of ITO thin films (2-5x 10^{-4} Ω.cm) is due to its huge concentration of charge carriers (>10^{20} cm^{-3}) and to its mobility few tens of $cm^2V^{-1}s^{-1}$), despite the fact that in a polycrystalline semiconductor the mobility is limited by three main diffusion mechanisms: diffusion by ionized impurities, diffusion by neutral impurities and diffusion by grain boundaries.

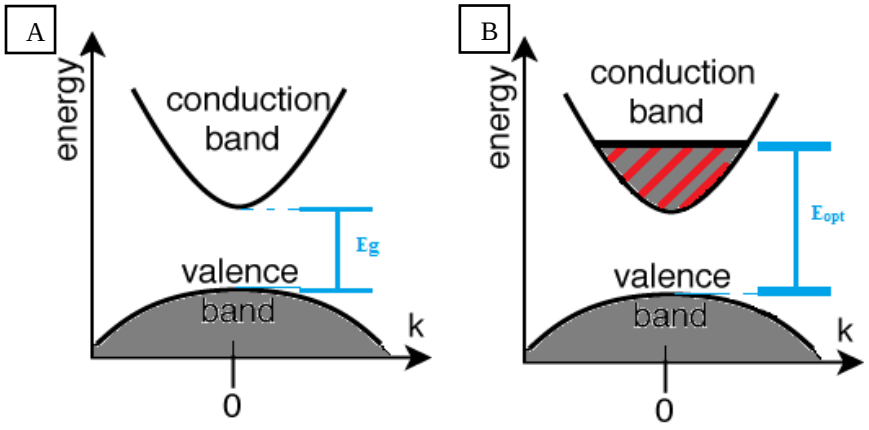

Figure 4-2. A) Band diagram for non-doped In_2O_3 and B) the effect of tin doping.

The band diagram of intrinsic Indium Oxide (In_2O_3) at 0 K is presented in Figure 4-2.A. The Fermi level (E_F) is localized in the middle of the band gap (E_g ~ 3.5eV), the conduction band is empty and the In_2O_3 is transparent and insulating. If some little doping is introduce to In_2O_3, the donor levels appear near the minimum of the conduction band. For a certain quantity of donors (N), the donor levels are combined with the conduction band and E_F is thus in the conduction band: this critical value is Nc ~ $2.3x10^{19}cm^{-3}$ (Gupta, 1989). For N >Nc the semiconductor behaves like a metal according to non-metal/metal Mott's transition.

Thanks to its high bandgap, ITO, like other TCOs, is highly transparent in the visible range. However, in the near-IR and IR regions, the excitation of the free carriers generates absorption by the layer due to intraband transitions within the conduction band. As the number of free electrons is increased, the absorption in the near-IR is increased and the absorption edge in the near IR is shifted to shorter wavelength values. At some point, free carrier absorption starts to have an impact on the spectral range of interest for solar cells. We can then easily understand that TCOs suffer from a compromise between conductivity: carrier concentration has to be sufficiently high for the TCO to be conductive but should not be too high in order to avoid to high absorption in the near IR. As the conductivity is also directly proportional to the carrier mobility, a good way to optimize the conductivity-transparency compromise of TCOs is to have a layer with the highest mobility.

4.2 Characterization Tools

In this section, four techniques of characterization will be described: Four probe technique, Hall Effect Measurement, Ellipsometry and Spectrophotometry.

4.2.1 Sheet Resistance by four probe technique

The sheet resistance R□ is a scalar physical quantity which is measured in thin films. The Resistance of any sample can be written as:

$$R = \frac{\rho . l}{A} = \frac{\rho . l}{w . d} = \frac{\rho}{d} . \frac{l}{w} = R_{\square} . \frac{l}{w} \qquad (4\text{-}1)$$

Where ρ is the resistivity, l is the length, w is the width, d is the thickness and A is the area of the cross section. R□ is defined as:

$$R_{\square} = \frac{\rho}{d} \qquad (4\text{-}2)$$

The R□ depends on the material properties and the thickness of the sample and its SI unity is $\Omega.\square^{-1}$.

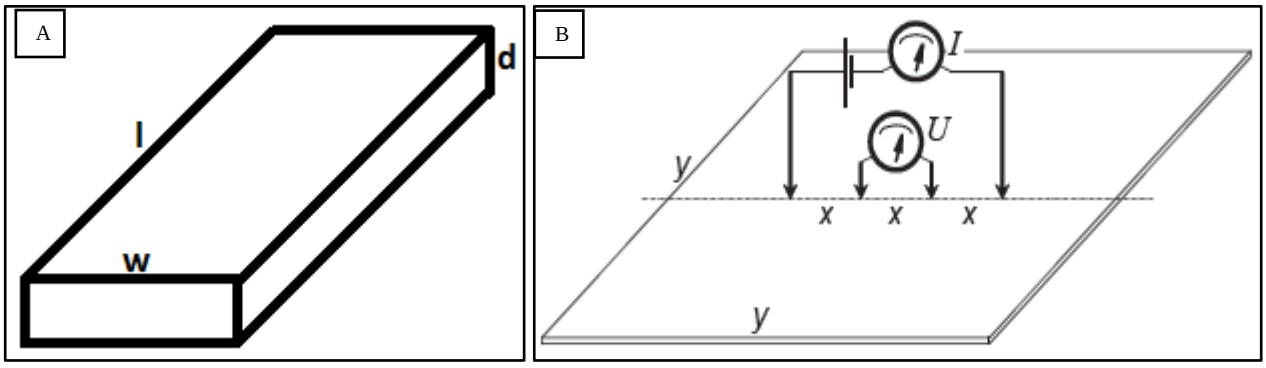

Figure 4-3. A) Sample with dimensions w, l, and d. B) Four probes measurement.

In order to measure the R□ of a thin film, the four probes must contact the thin film surface as it can be seen in Figure 4-3.B. Then a current I passes through the external probes while the potential V is measured between the middle probes.

Van der Pauw showed that V, I and R□ are related by (Van der Pauw, 1958):

$$R_{\square} = \frac{\pi}{\ln 2} \frac{V_{measured}}{I_{measured}} \tag{4-3}$$

The R□ is measured with the Napson-5 four point probe resistivity measurement system. The four probes head of the NAPSON equipment is shown in Figure 4-4. Samples of ITO thin films on glass and on silicon type n substrate were measured before ELA treatments as presented in Table 4-1, thickness of ITO is ~100 nm.

Table 4-1. Initial values of ITO/g and ITO/Si.

SAMPLE	R□ ($\Omega.\ \square^{-1}$)
ITO/g initial	100
ITO/Si initial	90

Figure 4-4. Four probes head of the NAPSON equipment.

4.2.2 Hall Effect Measurement: mobility (μ_H) and carrier concentration (N)

4.2.2.1 Hall Effect

The Hall Effect is shown in Figure 4-5 (Sze, 2006). When an electron travels under the action of an external electric field E_x (current I in the sample) which is perpendicular to the magnetic field B_z, this electron experiences a Lorentz force F in the " - y" direction, deviating the electron from its original trajectory.

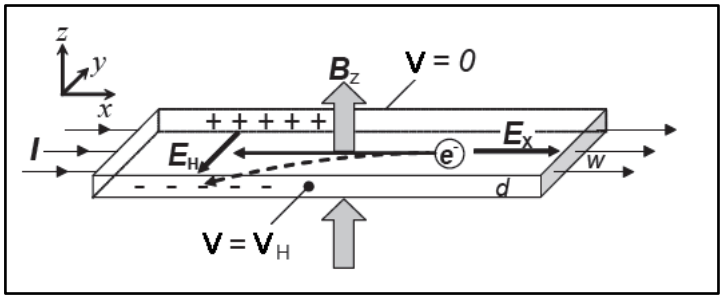

Figure 4-5. Sample under a magnetic field B_z, and illustration of the hall voltage V_H (Legeay, 2011).

If the sample is insulated in the y direction, charge carriers start to accumulate on the lateral walls. These charge carriers create an electric field E_H, and this electric field produces a force which is opposed to the Lorentz force (produced by the magnetic field B_z). As a result of the accumulation of charge carriers, an electrical potential $V_H = w\ E_H$ appears between lateral walls (this tension V_H can be measured with a voltmeter). The width and the thickness of the sample are w and d respectively.

$J_x = I /w.d$ is the current density along the x axis and $J_x = \sigma\ E_x$, with:

$$\sigma = Ne\,\mu_e \qquad (4\text{-}4)$$

Where N is the concentration of charge carriers (electrons in the case of an n-type semiconductor, *e* is the fundamental charge of the electron and μ_e is the mobility of free electrons (conducting electrons). The Hall field is: $E_H=A_H B_z \times J_x$, where A_H is the Hall constant of the material.

$$A_H = \frac{V_H \cdot d}{B \cdot I} \tag{4-5}$$

In a n-doped and non-degenerated semiconductor, the Hall constant is:

$$A_H = \frac{f_H}{N \cdot e} \tag{4-6}$$

The value of f_H depends on diffusion mechanisms of charge carriers. ITO is considered a **n-doped and degenerate semiconductor** (majority carriers are electrons and due to its doping level it can be treated as a conductor), in this case $f_H \approx 1$, then:

$$\mu_e \approx \mu_H = \frac{\sigma}{N \cdot e} = \frac{\sigma \cdot A_H}{f_H} = \sigma A_H = \frac{\sigma \cdot V_H \cdot d}{B \cdot I} \tag{4-7}$$

4.2.2.2 Van der Pauw Method

The Van der Pauw method is used to measure the R□ of uniform thin films. An arbitrary form thin film of thickness d with 4 contacts (m, n, o and p) is shown in Figure 4-6 . A current (I_{mn}) is applied through the m and n contacts and then the electrical potential is measured between contacts p and o ($V_{op} = V_p - V_o$).

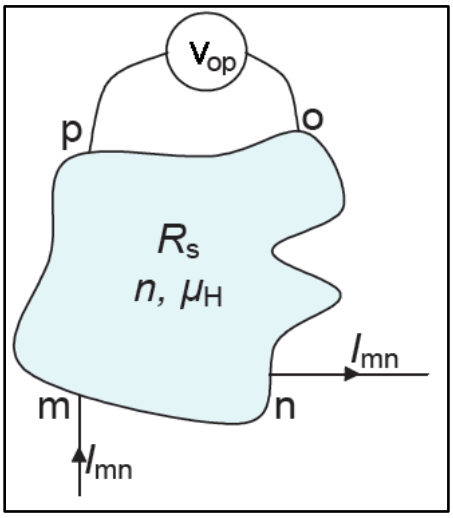

Figure 4-6. Arbitrary shaped thin film.

We define $R_{mn,op} = V_{op} / I_{mn}$, and in the same way $R_{no,pm} = V_{op} / I_{mn}$. Therefore Van der Pauw demonstrated the following relation (Van der Pauw, 1958):

$$exp\left(-\frac{\pi R_{mn,op}}{R_{\square}}\right) + exp\left(-\frac{\pi R_{no,pm}}{R_{\square}}\right) = 1 \qquad (4\text{-}8)$$

If the direction of the current I change, we have: $R_{mn,op} = R_{nm,po}$ and by a reciprocity relation we also have: $R_{mn,op} = R_{op,mn}$. Finally, we only have two values for eight possible measurements:

$R_A = R_{mn,op} = R_{nm,po} = R_{op,mn} = R_{po,nm}$

$R_B = R_{no,pm} = R_{on,mp} = R_{pm,no} = R_{mp,on}$

In no-symmetry conditions $R_A \neq R_B$, then eq. (4-8) becomes:

$$exp\left(-\frac{\pi R_A}{R_{\square}}\right) + exp\left(-\frac{\pi R_B}{R_{\square}}\right) = 1 \qquad (4\text{-}9)$$

At the end, the R□ can be obtained by solving numerically eq. (4-9).

4.2.2.3 N y μ_H Measurements

Sheet resistance of a sample of ITO/g is measured by Van der Pauw method, while the n value is measured by Hall Effect and finally μ_H is deduced from these two measurements. Both measurements are made using the same pinboard of the HMS-5000 Hall Effect Measurement System (Figure 4-7.B). The sample must be squared and uniform (see Figure 4-7.A).

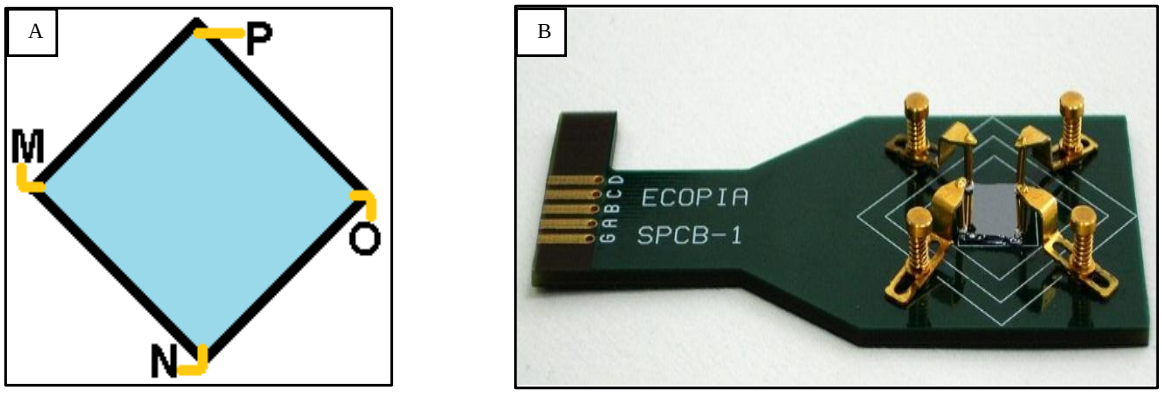

Figure 4-7. A) ITO/g sample. B) Pinboard of HMS-5000 Hall the measurement system

Van der Pauw demonstrated that a variation in the magnetic field perpendicular to the sample produces a variation in the $R_{mo,np} = V_{np} / I_{mo}$. This means that $\Delta R_{mo,np}$ can be used to calculate the Hall constant A_H (Van der Pauw, 1958):

$$A_H = \frac{d}{B} \Delta R_{mo,np} \qquad (4\text{-}10)$$

The HMS-5000 equipment can provide N y μ_H values in this way:

- To calculate n, the equipment applies a magnetic field perpendicularly to the sample first in one direction and then in the opposite direction while making a current I_{mo} flowing between the m and o contacts and measures $\Delta R_{mo,np}$. The procedure is repeated to measure $\Delta R_{np,om}$, $\Delta R_{om,pn}$ and $\Delta R_{pn,mo}$. The average Hall coefficient is deduced from these measurements and eq. (4-11).The operator just has to enter the thickness of the thin film and the value of n is deduced from eq. (4-6)
-
- To calculate μ_H, the equipment measures $R_{mn,op}$, $R_{nm,po}$, $R_{op,mn}$, $R_{po,nm}$ $R_{no,pm}$, $R_{on,mp}$, $R_{pm,no}$ and $R_{mp,on}$ and then calculates R□ using eq. (4-10). From this and with the sample thickness, one gets the value of the conductivity σ and finally μ_H can easily be obtained from eq.(4-7)

4.2.3 Ellipsometry

Ellipsometry is an optical characterization technique that uses the interaction of polarized light with the Surface of a material to determine its dielectric function. It can be used to characterize the refraction index (n), the extinction coefficient (k) and the thickness (d) of thin films (from Å to µm) among other properties.

This technique is not going to be described in detail in this report due to its high complexity; however the principle is explained in Figure 4-8.B. When a light ray (E_i) which has a linear polarization interacts with a surface making a certain incident angle, this ray can be expressed as the combination of two components –s (perpendicular component) and –p (parallel component) in respect to incidence plane. Then the incident ray is reflected by the surface, changing its components, now with an elliptic polarization (E_r). The characteristics of the polarization depend on the thickness of the film, the properties of the material, the variation of the incident angle and the wavelength of the incident ray. In our case, we used the method of constant angle.

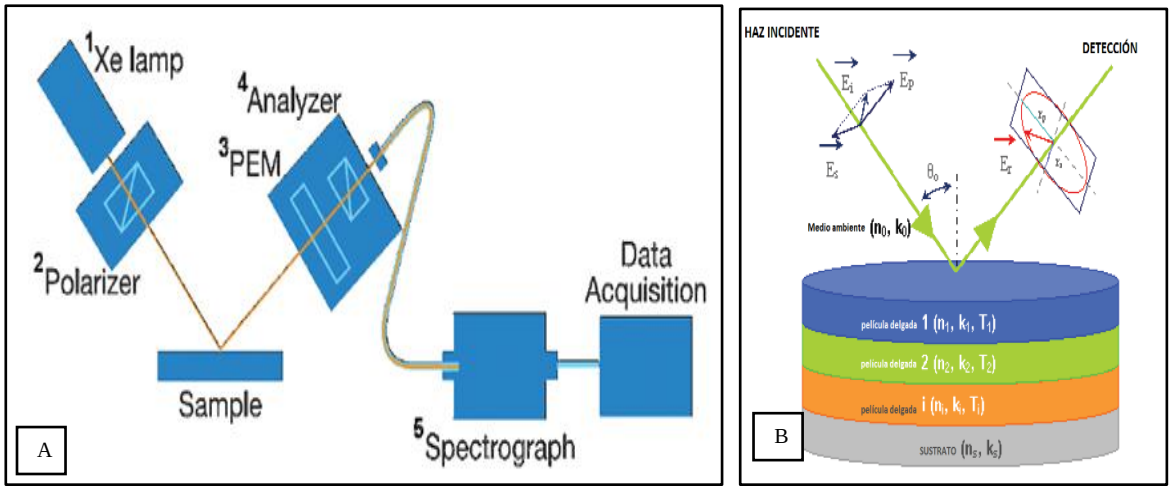

Figure 4-8. A) Parts of an ellipsometer (Muñoz D. , 2008). B) Principle of work of an ellipsometer.

The ellipsometer is a Horiba Jobin-Yvon equipment and its principal parts are: 1) a source of light, 2) a polarizer, 3) a photoelastic modulator (PEM), 4) an analyzer (another polarizer), 5) a monochromator and a detection system, as presented in Figure 4-8.A.

Ellipsometry does not directly measure the n, k and d values of the thin film. It utilizes a model or the combination of dispersion models (Drude, Tauc-Lorentz, Cauchy…) whose parameters will be changed until the simulation coincides with the pseudo-dielectric function $\langle \tilde{\epsilon}\ (\omega) \rangle$ of the sample (substrate and thin film), see eq.(4-11). The model used must be coherent with the nature of the material (semiconductor, insulator or conductor) whereas the pseudo-dielectric function takes into account the response of the material and the response of the substrate. As a consequence, the optical behavior of the substrate must be known (transmission and reflectivity) (Keita, 2012). The expression of the pseudo dielectric function is:

$$\langle \tilde{\epsilon}\ (\omega) \rangle = \sin\theta \left\{ 1 + \left(\frac{1-\rho}{1+\rho} \right)^2 . \tan\theta \right\} \tag{4-11}$$

Where the incident angle is θ =70° and ρ is the ratio of reflection coefficients:

$$\rho = \frac{r_p}{r_s} = \tan(\Psi)\ e^{-i\Delta} \tag{4-12}$$

Ψ and Δ are the ellipsometric angles which are measured by the ellipsometer and they are related to the index of refraction, extinction coefficient, thickness, etc. A model commonly used for ITO is the Drude-Lorentz dispersion model:

$$\epsilon(\omega) = \epsilon_\infty + \frac{{\omega_p}^2}{-\omega^2 + i\Gamma_d\omega} + \frac{(\epsilon_s - \epsilon_\infty)\omega_t^2}{{\omega_t}^2 - \omega^2 + i\Gamma_0\omega} + \sum_{j=1}^{2} \frac{f_j\omega_{0j}^2}{{\omega_{0j}}^2 - \omega^2 + i\gamma_j\omega} \tag{4-13}$$

To measure ITO optical properties the ellipsometer makes these steps: First of all, it measures the ellipsometric angles (Ψ and Δ) and then it fits the parameters ($\omega_p, \omega_t, \epsilon_s$, etc.) in

eq. (4-13) until $\epsilon(\omega) = \langle \tilde{\epsilon}_{ITO}(\omega) \rangle$. Afterwards, it can calculate the index of refraction and the extinction coefficient solving $\epsilon_1 = n^2 - k^2$ and $\epsilon_2 = 2nk$, where $\epsilon(\omega) = \epsilon_1 + i\,\epsilon_2$.

4.2.4 Spectrophotometry

The measurement of Transmission (T) and the reflectivity (R) are made with a spectrophotometer Perkin-Elmer Lambda UV-VIS-IR.

When a measurement of Transmission is made, the spectrophotometer makes a ratio between the quantity of radiation that passes through a sample and the quantity of incident radiation for a given a wavelength. For measuring the Reflectivity, the ratio between reflected radiation and incident radiation is made. Finally, Absorption is A=1-T-R.

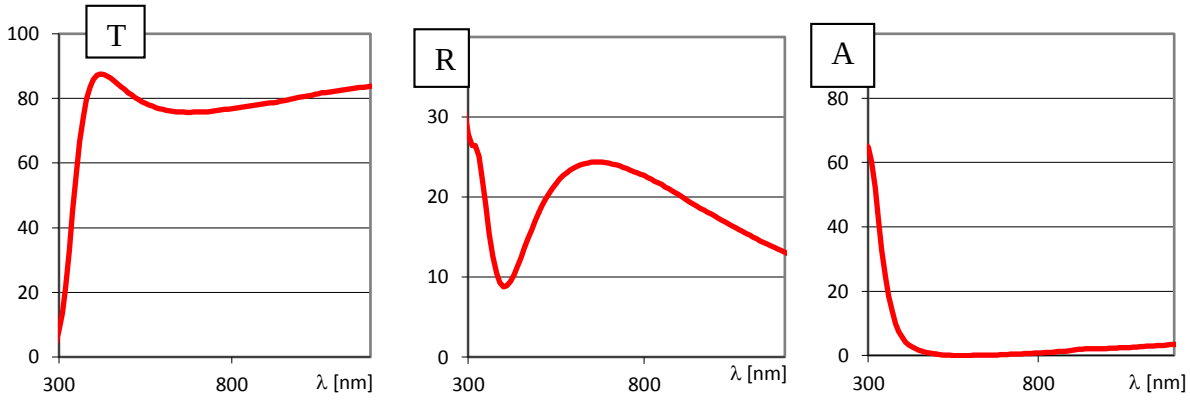

Figure 4-9. Transmission, Reflectivity and absorption spectrums of ITO on glass.

Furthermore the effective transmission, effective reflectivity and effective absorption can be calculated with eq. (4-14) in the range of importance of a solar cell <300, 1200>nm.

$$T_{eff}; R_{eff}; A_{eff} = \frac{\int_{300}^{1200} (T; R; A).\ Solar\ Spectrum\ d\lambda}{\int_{300}^{1200} Solar\ Spectrum\ d\lambda} \qquad (4\text{-}14)$$

Where solar spectrum is the number of photons of the solar spectrum A.M. 1.5 that get to the Surface of the earth for a certain wavelength.

4.2.5 Scanning Electron Microscope (SEM)

A Scanning electron microscope was used to observe the superficial changes or damages after ELA treatments on different samples. The work principle is very simple: an electron beam (primary electrons) is projected on the sample. The interaction between the electrons and the sample generates secondary electrons (electrons from outer shells). Secondary electrons are very sensitive regarding the roughness of the surface, thus allowing to get a cartography of the surface.

4.3 Results and Observations

In this section, ITO, AZO and IOH ELA treatment results will be described and discussed.

4.3.1 ITO results

Sheet resistance (R□) as a function of the energy density of the irradiation is shown in Figure 4-10.A. The R□ of ITO/**g** decreases strongly for energy densities in the range of 175-300 mJ.cm^{-2} whereas for ITO/**Si** samples, R□ decreases more progressively in the interval 250-500 mJ.cm^{-2}. This difference in behavior of laser annealed ITO thin films on different substrates under the same energy density could be explained by the difference in thermal conductivity of the substrates.

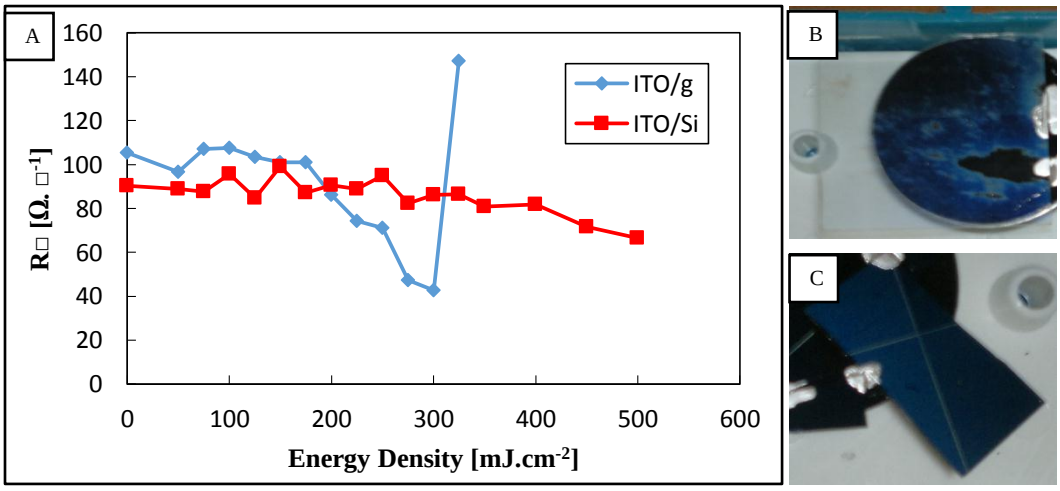

Figure 4-10. A) Sheet Resistance vs Laser fluences. B) ITO/g sample annealed with 500 mJ.cm^{-2}. C) ITO/Si sample annealed with 1000 mJ.cm^{-2}.

Thus, heat evacuation from ITO thin film seems to be more important through Silicon than through glass substrates, hence inducing more heat concentration and producing more changes

in ITO/**g** samples. For laser fluences above 325 mJ.cm^{-2}, R□ increases considerably in ITO/**g** samples because of the high laser energy that produces a degradation of the ITO layer as it can be seen in Figure 4-10.B. For ITO/Si samples the damage can be seen for laser fluences above 500 mJ.cm^{-2}, see Figure 4-10.C.

A mapping of the sheet resistance was made on some ITO/g samples to measure the homogeneity before and after the ELA. As it can be seen in Figure 4-11.B, although the sheet resistance is considerably decreased, the sheet resistance homogeneity is worse than before.

To study the influence of number of shots with the same energy density, different laser treatments were made on ITO/g and ITO/Si samples (see Table 3-2). As it is showed in Figure 4-12, the laser treatments with 50 and 100 mJ.cm^{-2} don't produce a net change in sheet resistance for different number of shots neither in ITO/g (Figure 4-12.A) nor in ITO/Si samples (Figure 4-12.B). Above 250 mJ.cm^{-2}, the sheet resistance experiments a drop for ITO/g and ITO/Si and a good stabilization of the value for a number of shots > 2. We can then conclude that one can change the material properties with one laser shot, but then these become stable upon ELA. The minimum values of sheet resistance after ELA for ITO/g and ITO/Si are respectively 40 Ω.□$^{-1}$ and 70 Ω.□$^{-1}$.

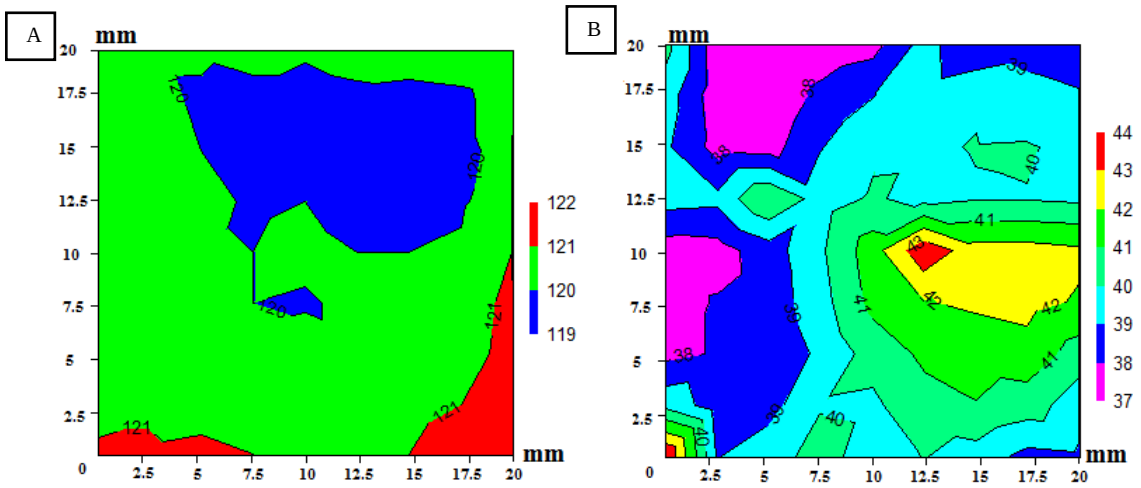

Figure 4-11. Mapping of sheet resistance of ITO/g A) before and B) after laser fluency 300 mJ.cm^{-2}.

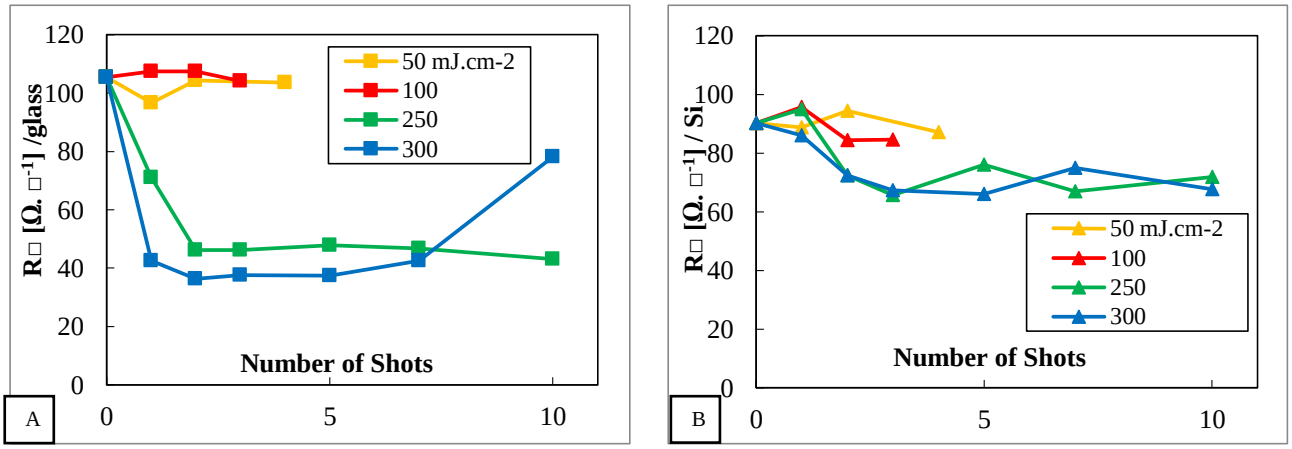

Figure 4-12. Sheet resistance vs Number of shots with the same Energy Density for (A) ITO/g and (B) ITO/Si

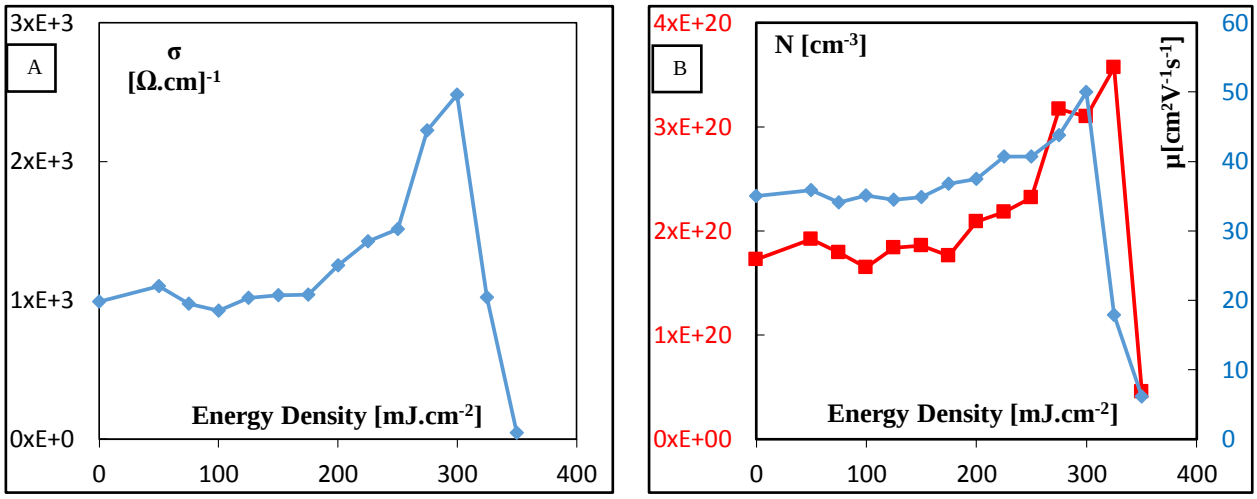

Figure 4-13. A) Conductivity-σ vs Energy Density of ITO/g. B) Concentration-N (red) and mobility-μ (blue) vs Energy Density of ITO/g

In Figure 4-13, there is no change in conductivity (σ), density of charge carrier (N) and mobility (μ) for laser fluences below 175 $mJ.cm^{-2}$ in ITO/g samples, whereas a strong increment of these variables is observed for 175 to 300 $mJ.cm^{-2}$ energy densities: σ increases from $1x10^{-3}$ $\Omega^{-1}.cm^{-1}$, N from $1.7x10^{20}$ to $3.6x10^{20}$ cm^{-3} and μ from 35 to 50 $cm^2.V^{-1}.s^{-1}$. As σ is directly proportional to N and μ, this means σ increases thanks to the increase in both N and μ. The increment in N could be due to recrystallization that would allow a better activation of doping atoms (Sn → Sn^{4+}) or to the diffusion of oxygen atoms out of the layer. The increment in μ could be due to recrystallization or increased grain size. Last, σ, N, μ drop for laser fluences above 300 $mJ.cm^{-2}$ due to damage of the layer mentioned above.

Transmission spectra of ITO/g for different laser fluences are showed in Figure 4-14 . The change in transmission can be observed above 300 $mJ.cm^{-2}$. The transmission increases gradually in the range of interest for the cell functioning <500, 1200> nm for ELA energies from 300 to 400 $mJ.cm^{-2}$. However, for wavelengths above 1500 nm, we can clearly observe a strong decrease in the transmission as the energy of irradiation increases: this can be directly correlated with the increase in carrier concentration (see Figure 4-13.B) and thus in free carrier absorption

in the IR. Furthermore, a dramatic change in transmission can be seen for a 500 mJ.cm^{-2} laser fluence due to a certain thin film degradation after high energy laser annealing.

The absorption experiments a blue shift for energy densities above 250 mJ.cm^{-2}, see red arrow in Figure 4-15.fluences. The Absorption reduction in the UV wavelength range thanks to this blue shift can be explained by the increment of charge carriers in conduction band (see Figure 4-13.B) and is known as the Burstein-Moss effect.

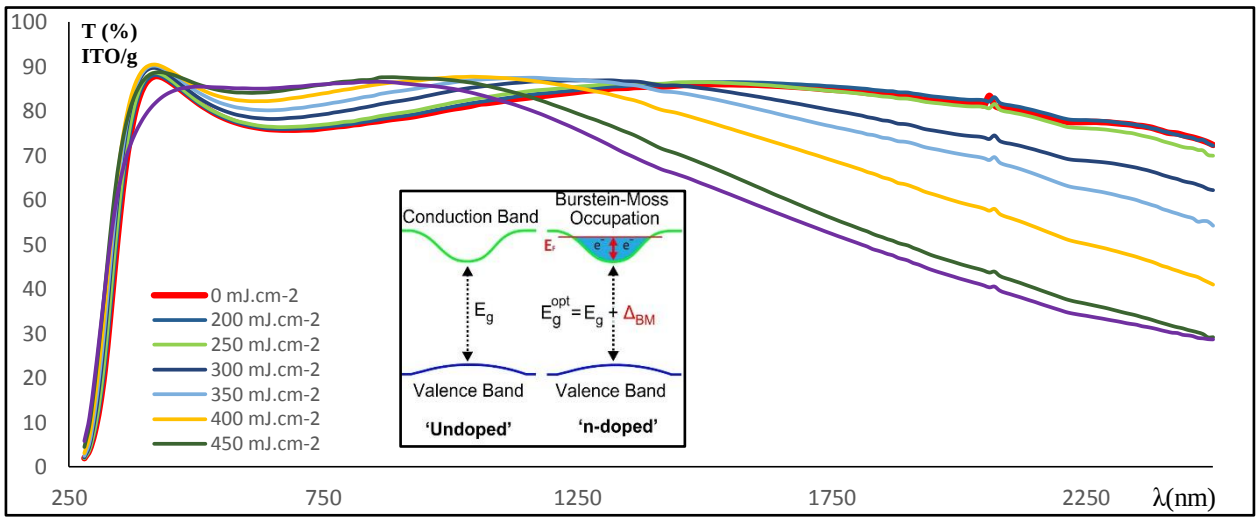

Figure 4-14. Transmission vs wavelength of ITO/g for different energy densities. Inset: Burstein Moss effect

.

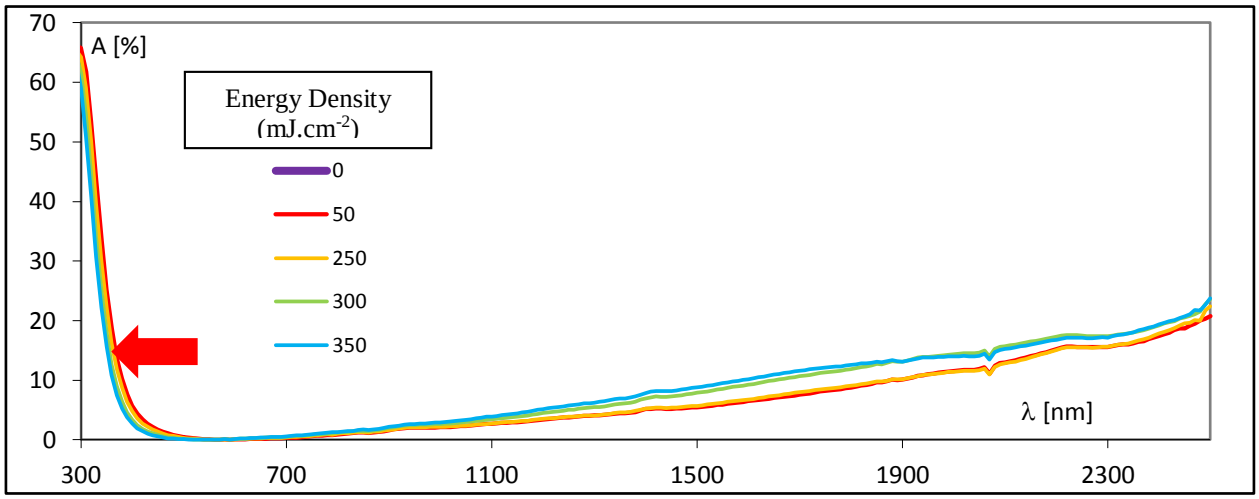

Figure 4-15. Absorption spectrum of ITO/g for different laser fluences.

Table 4-2.Optical band gaps ITO/g samples for different ELA treatments.

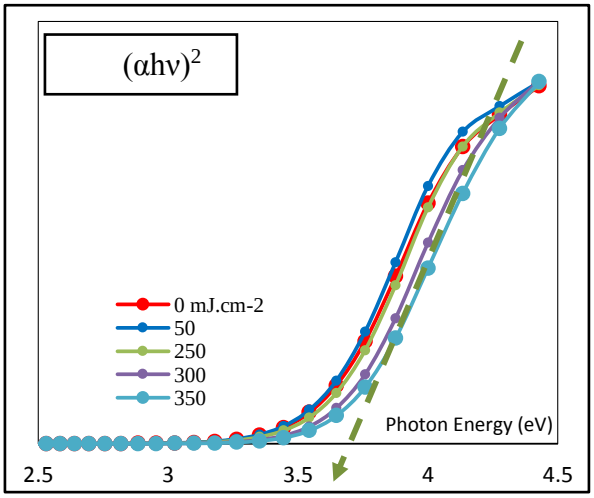

Figure 4-16. Tauc-plot for band gap calculation.

Energy Density ($mJ.cm^{-2}$)	Optical Band Gap (eV)
0	3.57
50	3.58
250	3.60
300	3.65
350	3.69

The Burstein-Moss effect explains the increment of optical band gap or increment of the absorption edge (blue shift) in some degenerate semiconductors of type n (type p) as a result of the occupation of states near the conduction band (valence band) due to a charge carrier augmentation (see Figure 4-15. inset). Tauc plot $[(\alpha h\nu)^2$ vs. photon energy] is used to calculate optical band gap of the ITO/g after ELA, where α is the absorption coefficient, $h\nu$ is the photon energy. In the plot, the curve shows a section of straight line (ex. green dash line) which is extrapolated to the x-axis. The x-intercept of this line gives the optical band gap, see Figure 4-16. The estimated optical band gaps are listed in Table 4-2. The increment of the optical band gap coincides with the blue shift in absorption spectra.

The Teff, Reff and Aeff values of **ITO/g** samples after treatment with different laser fluences are shown in Figure 4-17.A. There is almost no change in these effective values for energy densities below 225 $mJ.cm^{-2}$. For laser fluences from 250 to 300 mJ/cm2, Teff slightly increases while Reff decreases and Aeff stays practically constant: for these fluences, the change in ITO optical properties could be then beneficial for the solar cell performance.

In Figure 4-17.B and Figure 4-17.C, the pseudo dielectric functions of **ITO/Si** samples (optical response from both, substrate and thin film) experiment no deviation from reference sample (0 $mJ.cm^{-2}$) which shows that no change in refractive index after laser annealing occurs in the range 0-325$mJ.cm^{-2}$. This is contradictory to what is observed by spectrophotometry on the **ITO/g** samples and confirms the behavior difference between **ITO/g** and **ITO/Si** samples already observed when measuring electrical properties.

In Figure 4-13.A and Figure 4-17.A, it can be seen that there is an augmentation of conductivity and transmission and a diminution of reflection in the range 200-300 mJ/cm^{-2} showing an improvement in both electrical and optical properties of ITO/g by thin film laser annealing. These results show that ELA seems to be very promising for improving HET solar cell performances via the improvement of ITO.

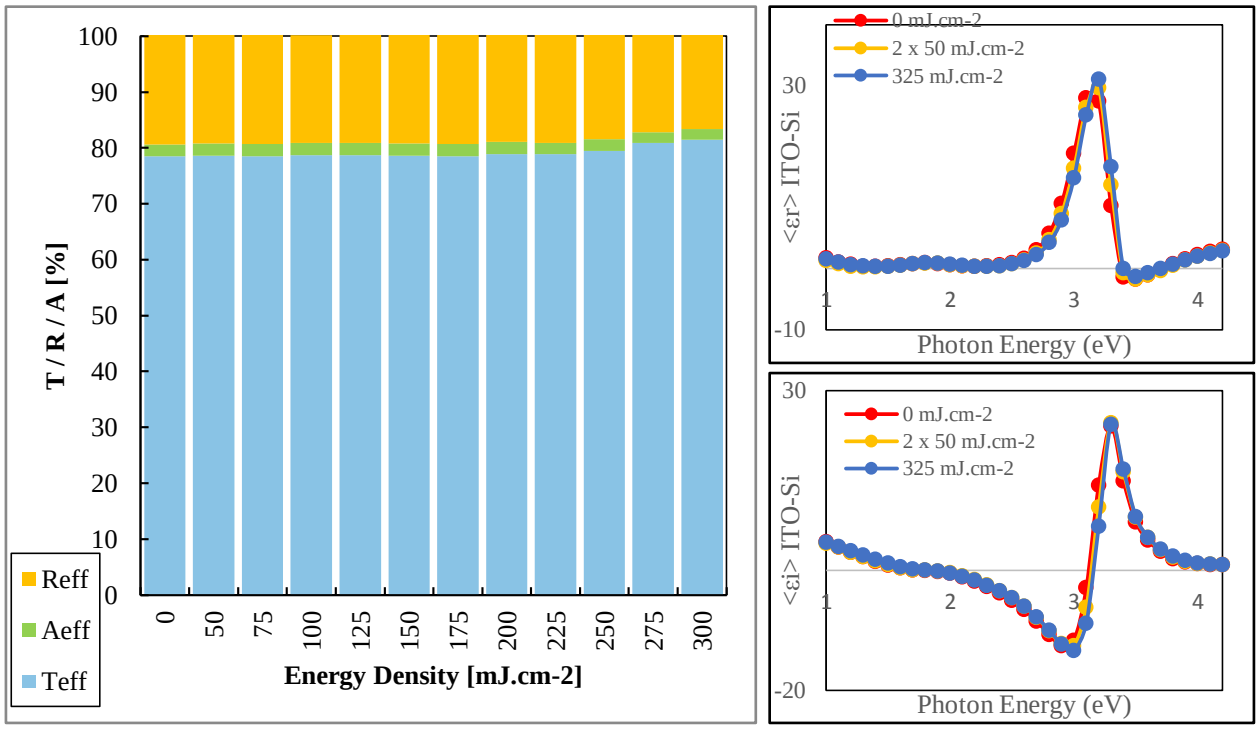

Figure 4-17. A) Effective values for different laser treatments of ITO/g. B) Real part and C) imaginary part of pseudo dielectric function vs. photon energy for ITO/Si.

In order to get a deeper insight into the superficial microstructure of ITO thin films before and after ELA treatments, we performed SEM characterization (see Figure 4-18). In Figure 4-18.A, a reference sample ITO/Si is shown (without laser annealing).

In Figure 4-18(A-H), we can identify domains in the surface of ITO which are located one next to the other with a non-defined shape; domains or grains are made of an ensemble of columnar-like crystals that have grown in only one direction thus permitting to differentiate one domain from the other.

In particular, Figure 4-18.G shows the presence of cracks over the ITO surface treated with an energy density of 750 mJ.cm^{-2} which could be explained by the huge amount of energy that

is given to the sample in a short time; such cracks can be related to the decrease of mobility hence the augmentation of Sheet resistance (see Figure 4-10.A, where values of Sheet resistance for laser fluences above 500 $mJ.cm^{-2}$ are too high to be presented in the graph). In Figure 4-18I and J show scanning electron micrographs of ITO/g treated at 500 $mJ.cm^{-2}$ and ITO/Si treated at 1000 $mJ.cm^{-2}$, respectively; we can see that ITO thin films were totally melted on these substrates. In this way, these two fluences are limiting values for annealing of ITO/g and ITO/Si samples respectively since they can destroy completely ITO thin films.

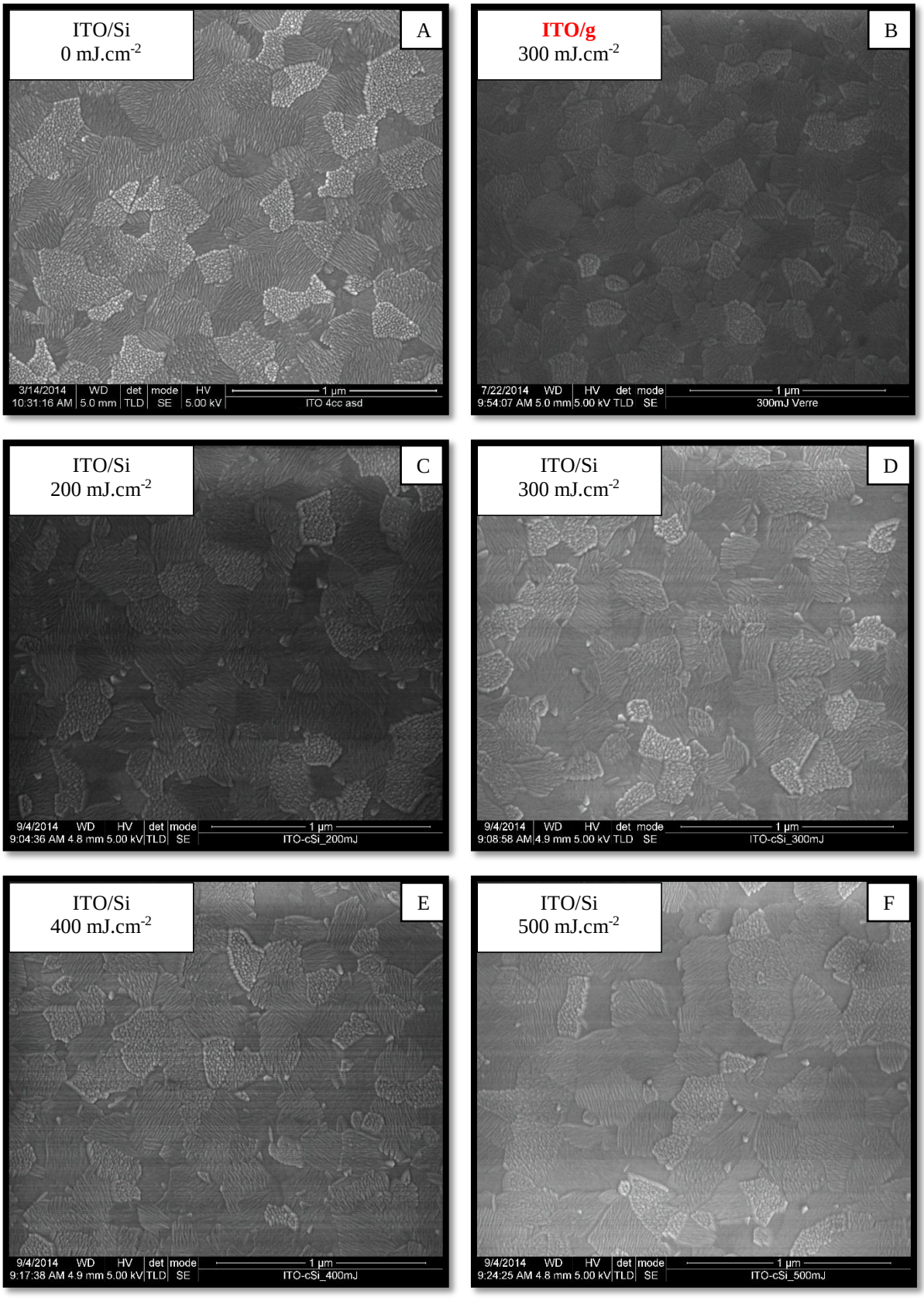

(Continued on the next

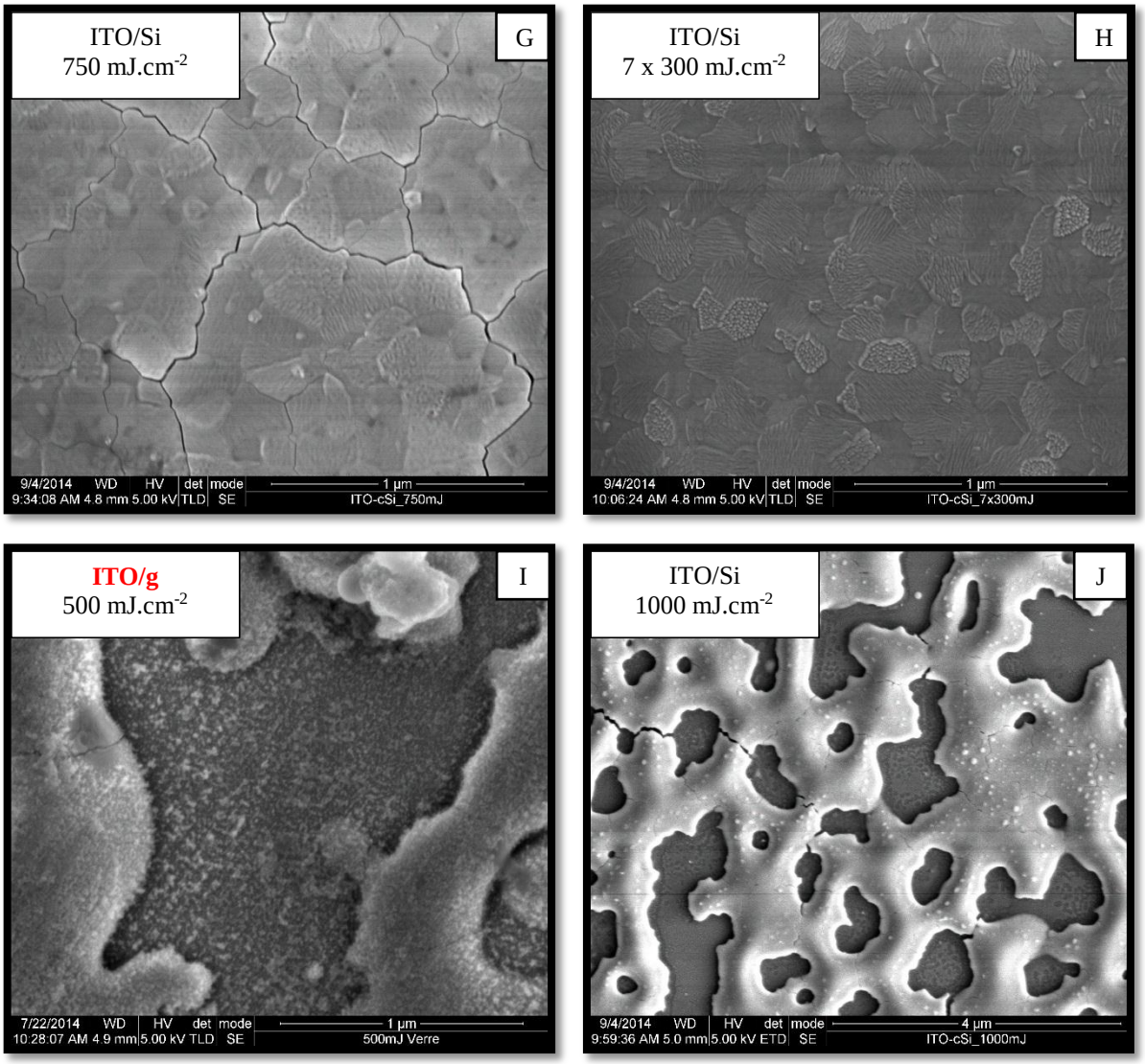

Figure 4-18. SEM Micrographs of ITO/g and ITO/Si samples treated under different energy densities. Description of each samples and the laser fluence used are shown in the box.

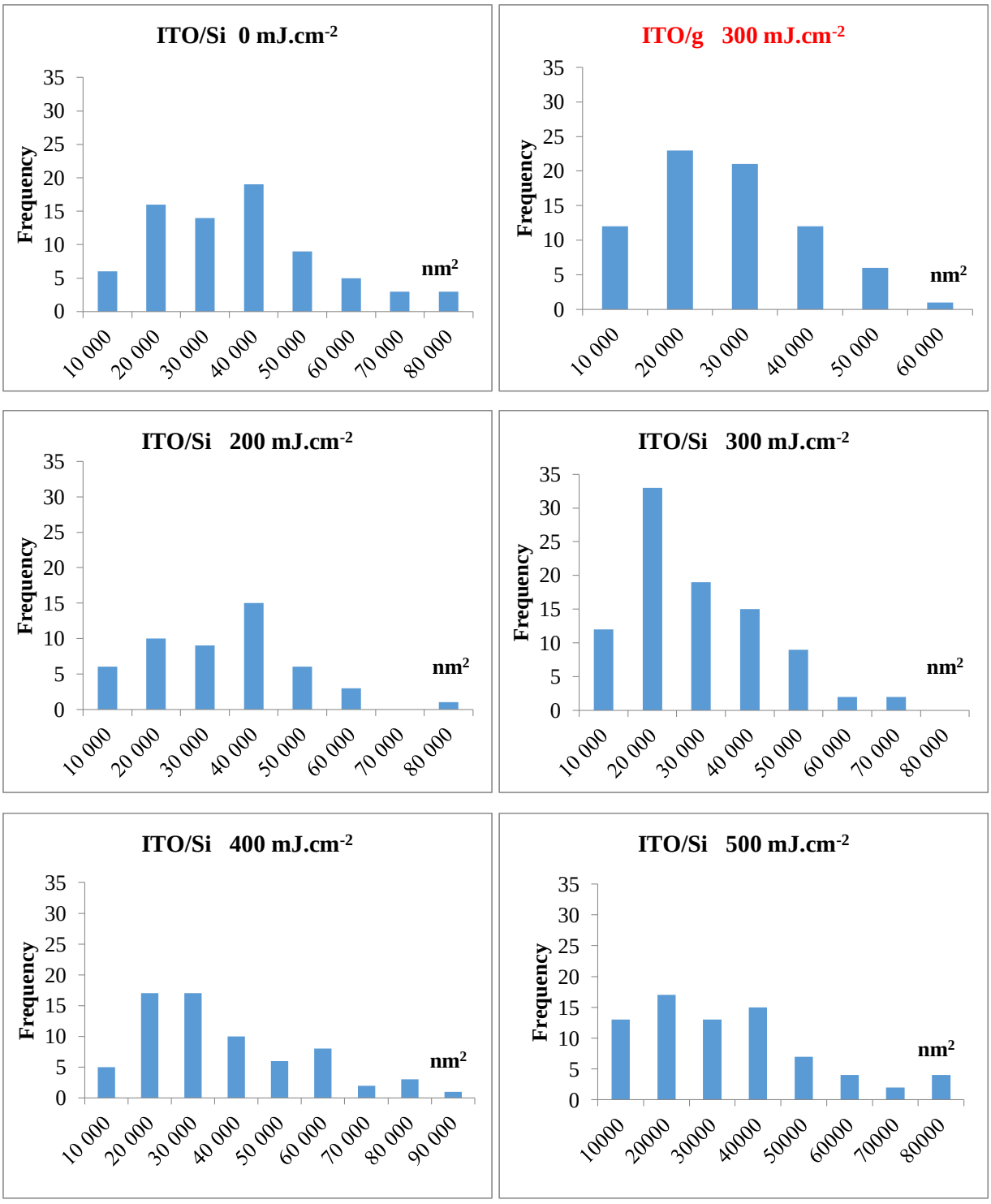

(Continued on the next page)

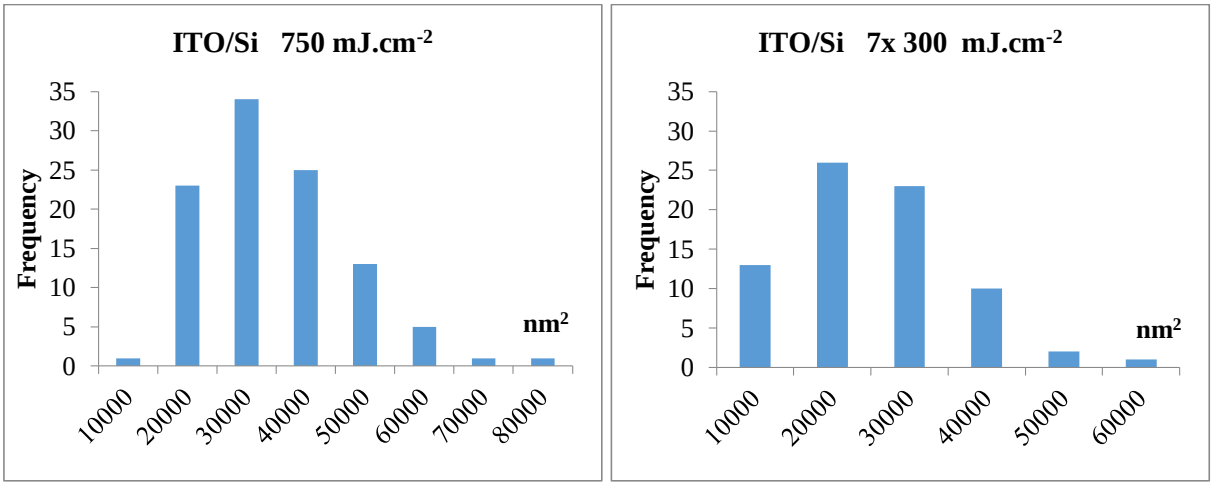

Figure 4-19. Histograms showing the distribution of size [Frequency vs. area (nm^2)] of the domains in the ITO/g and ITO/Si samples after laser annealing (10 000 nm^2= 0.01 μm^2) for different ELA treatments.

The area of the domains (see Figure 4-19 A-H) was measured with an image analysis software (ImageJ) and the corresponding histograms are presented in Figure 4-19. The unit of the area in the graphs is nm^2 but we will use μm^2 to indicate results (10 000 nm^2 = 0.01 μm^2). From the analysis of scanning electron micrographs, we determine the area distribution (size distribution) of domains which is uniformly distributed in the range: 10-80 K nm^2 (0.01-0.08 μm^2). The common size of ITO/g (300 mJ/cm^2), ITO/Si (ELA: 300 mJ/cm^2) and ITO/Si (ELA: 3 x 300 mJ/cm^2) is approximately 20K nm^2 which would indicate that grains mostly grow at this size.

4.3.2 AZO results

AZO was deposited onto glass (AZO/g) and silicon (AZO/Si) substrates with two thicknesses 100nm (AZO-100, see in .A) and 300nm (AZO-300, see in .B) and was also submitted to laser annealing (see laser fluences in Table 3-6 and Table 3-7). Like for ITO samples, we observe a difference of behavior of the film properties when performing the same ELA on different substrates that may also be explained by the difference in thermal conductivity of silicon and glass substrates as in ITO samples. There is an increment in sheet resistance for AZO-100/Si and AZO-300/Si with laser fluences above 300 $mJ.cm^{-2}$. However, there is no net change in sheet resistance neither for AZO-100/g nor AZO-300/g samples for irradiation below 200 $mJ.cm^{-2}$. It can be seen that there is a minimum at 100 $mJ.cm^{-2}$ for AZO-100/Si (125 $\Omega.\square^{-1}$), see Figure 4-20 .A.

Unlike for ITO/g samples, for AZO-100nm/g, there is almost no change in conductivity at fluences below 200 $mJ.cm^{-2}$ (see blue line in Figure 4-21.A), which confirms what was observed with 4-point probe measurement of $R_{\square}$ on glass. N experiments a slight increment and µ decreases as the laser fluence increases from 0 to 200 $mJ.cm^{-2}$, thus compensating each other and explaining the flat tendency observed for the conductivity. Above 200 $mJ.cm^{-2}$, the samples started to degrade: µ decreases drastically (see Figure 4-21.B), possibly because of the sample starting to crack like it was observed on ITO on Figure 4-18 G.

For AZO-300nm/g, there is a slight decrease of the conductivity from 570 to 510 $\Omega^{-1}.cm^{-1}$ when increasing the fluence from 0 to 300 $mJ.cm^{-2}$ (see red line in Figure 4-21.A). While N does not experiment any change below 400 $mJ.cm^{-2}$, µ value decays progressively thus explaining the reduction of the conductivity. Above 300 $mJ.cm^{-2}$ there is a strong degradation of thin AZO thin films resulting in a drastic reduction of the mobility and thus of the conductivity (see Figure 4-21.C).

The behavior of AZO electrical properties upon laser annealing is then completely different from what happens with ITO material: almost no change in conductivity for AZO vs. strong increase for ITO, degradation of the mobility of AZO layers vs. strong increase for ITO layers.

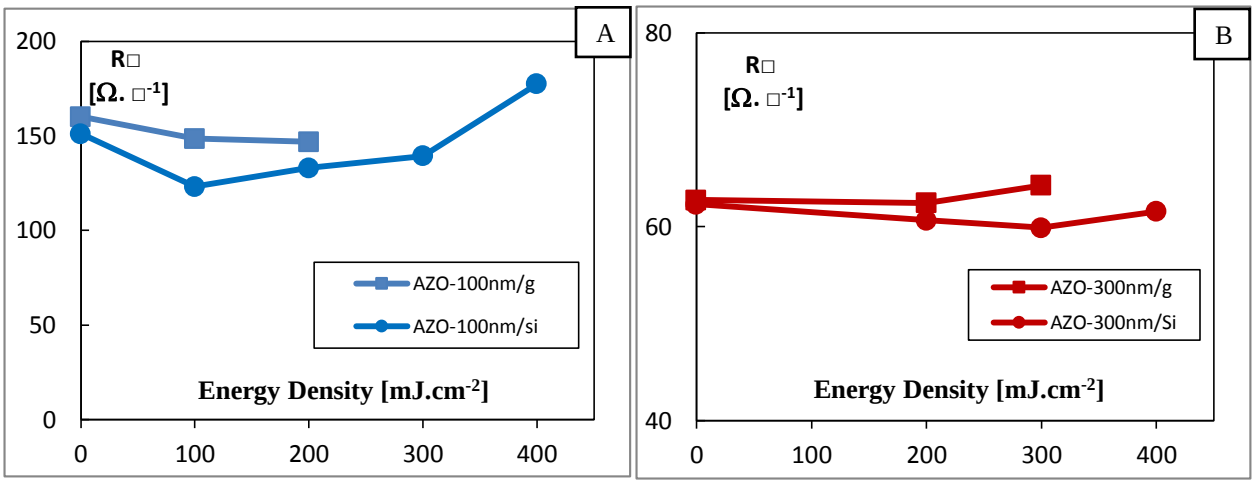

Figure 4-20. Sheet resistance vs. energy densities of: A) AZO-100nm and B) AZO-300nm

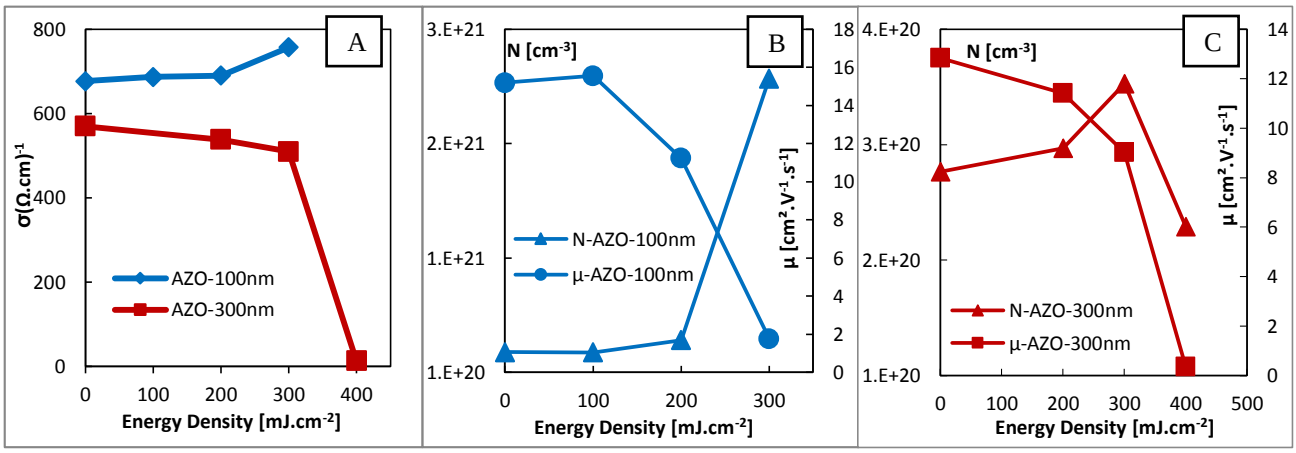

Figure 4-21. A) Conductivity. Concentration and mobility; after laser annealing of B) AZO-100nm/g and C) AZO-300nm/g

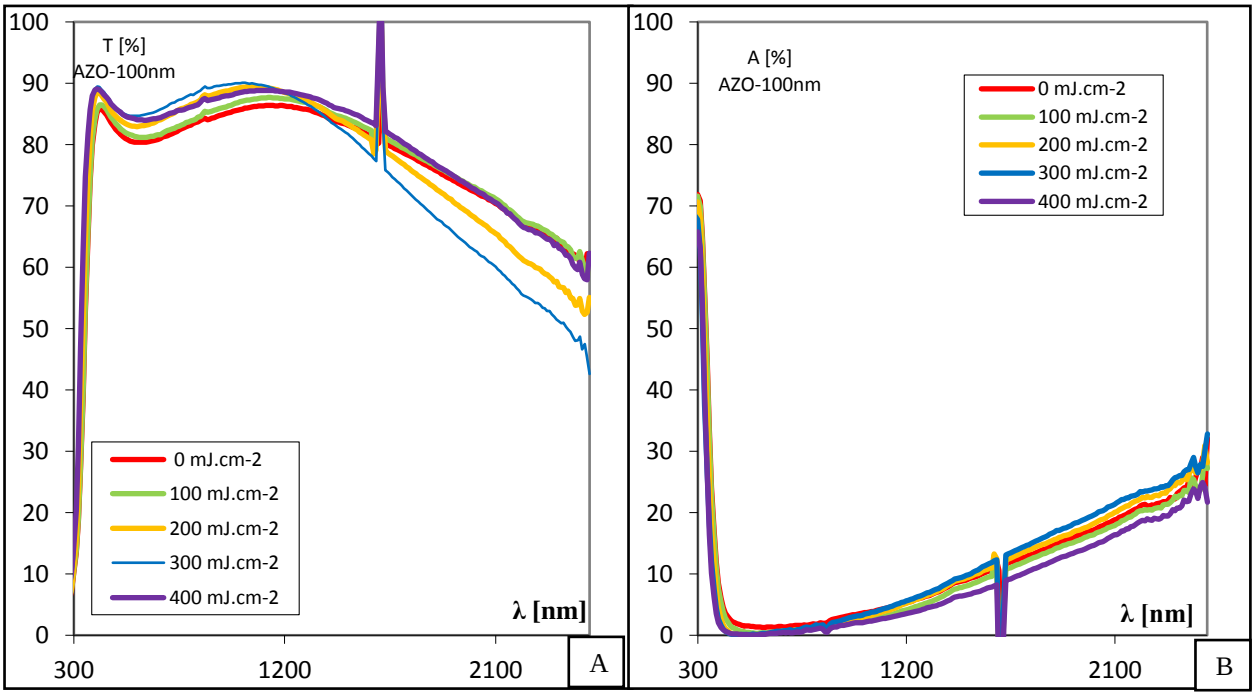

Figure 4-22. A) Transmission and B) Absorption spectra of AZO-100nm/g for different laser fluences.

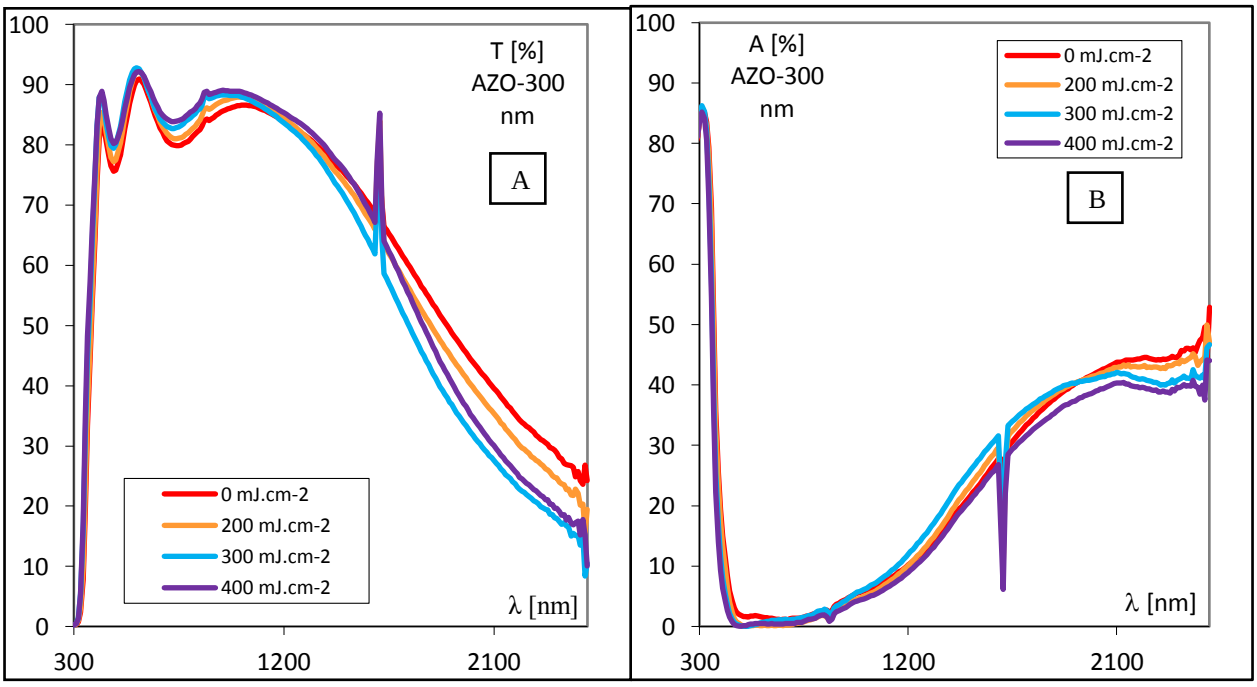

Figure 4-23. A) Transmission and B) Absorption spectra of AZO-300nm/g for various laser fluences.

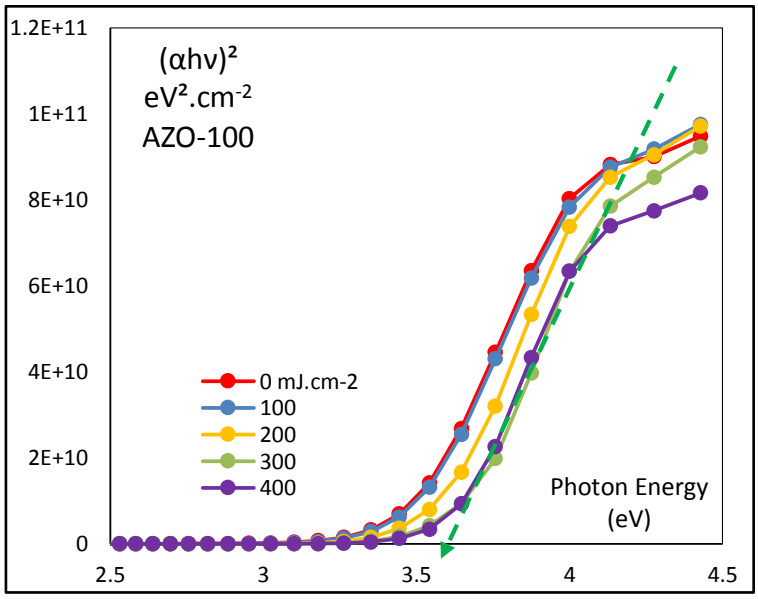

Figure 4-24. Band gap estimation of AZO-100nm/g using Tauc plot

Table 4-3.Optical band gaps of laser annealed AZO-100nm/g

AZO-100nm ($mJ.cm^{-2}$)	Optical Band Gap (eV)
0	3.44
100	3.46
200	3.55
300	3.64
400	3.62

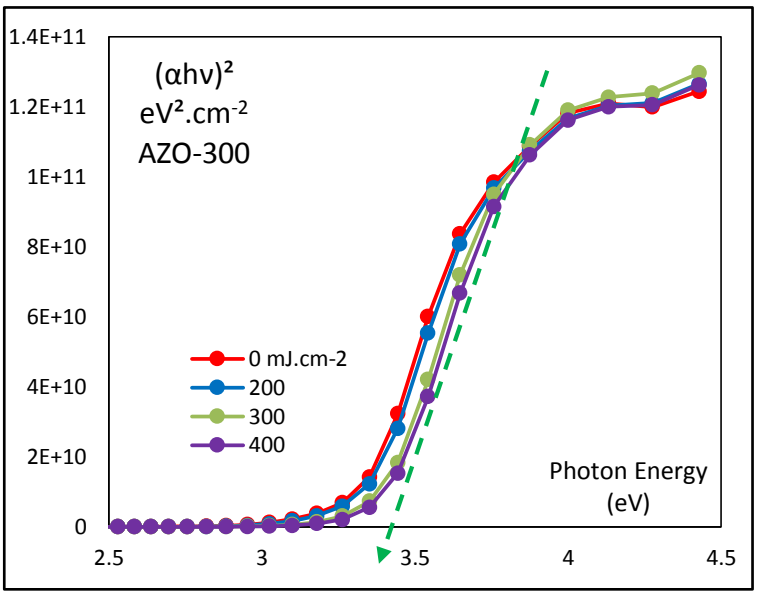

Figure 4-25. Band gap estimation for AZO-300nm/g using Tauc plot

Table 4-4. Optical band gap of laser annealed AZO-300/g

AZO-300nm ($mJ.cm^{-2}$)	Optical Band Gap (eV)
0	3.32
200	3.34
300	3.37
400	3.39

- AZO-100nm/g

In the range of photovoltaic interest (300-1200nm): Transmission (*T*) increases when fluences are incremented from 100 to 300 mJ.cm^{-2} (see Figure 4-22.A). Absorption (*A*) experiments a blue shift (see Figure 4-22.B) for laser fluences below 300 mJ.cm^{-2} which is confirmed by the calculation of optical band gap with Tauc plot (Figure 4-24): this can again be explained by the Burstein-Moss effect, like in the case of ITO. Last, the effective Absorption between 300-1200 nm slightly decreases for values below 300 mJ.cm^{-2} (see Figure 4-27.A).

In the IR range (1200-2500nm): Absorption increases while transmission decreases for laser fluences from 100 to 300 mJ.cm^{-2} because of increased free carrier absorption. Transmission augments and Absorption drops for 400 mJ.cm^{-2} probably as a result of the film degradation

- AZO-300nm/g

In the range of PV interest: Transmission (*T*) increases for laser fluences from 0 to 400 mJ.cm^{-2} (see Figure 4-23.A) while Absorption (*A*) experiments a blue shift (see Figure 4-23.B) that can again be explained by the Burstein-Moss effect.

In the IR range: Transmission decreases for laser fluences from 0 to 300 mJ.cm^{-2}, again due to increased free carrier absorption as N slightly increases (see Figure 4-23.A). For Absorption, it can be seen two ranges: <1200, 2000>nm where Absorption augments for energy densities below 300 mJ.cm^{-2} because of free carrier absorption and <2000, 2500>nm where Absorption decreases proportional to the energy density (see Figure 4-23.B).

For both thicknesses of AZO layers, the augmentation of Absorption in the IR range is related to increment of concentration of charge carriers, as already mentioned: this increase in N can result from activation of doping atoms (aluminum) in Zinc oxide thanks to the energy brought by the laser or from the diffusion of Oxygen atoms outside the Zinc oxide lattice thus creating more oxygen vacancies, after the heating of the layer resulting from laser annealing. (see Figure 4-27).

Pseudo dielectric functions resulting from ellipsometry measurements in **silicon substrates** are shown in Figure 4-26 for AZO-100nm/**Si** and AZO-300nm/**Si**. The absence of variability of the pseudo dielectric function (and thus of optical parameters n, k) confirms the very few changes in the sheet of the AZO thin films on Si samples under the different ELA. The different thickness in AZO samples can be confirmed by the oscillations in pseudo dielectric functions (compare Figure 4-26.A and Figure 4-26.C) and the greater Aeff for AZO-300 than for AZO-100.

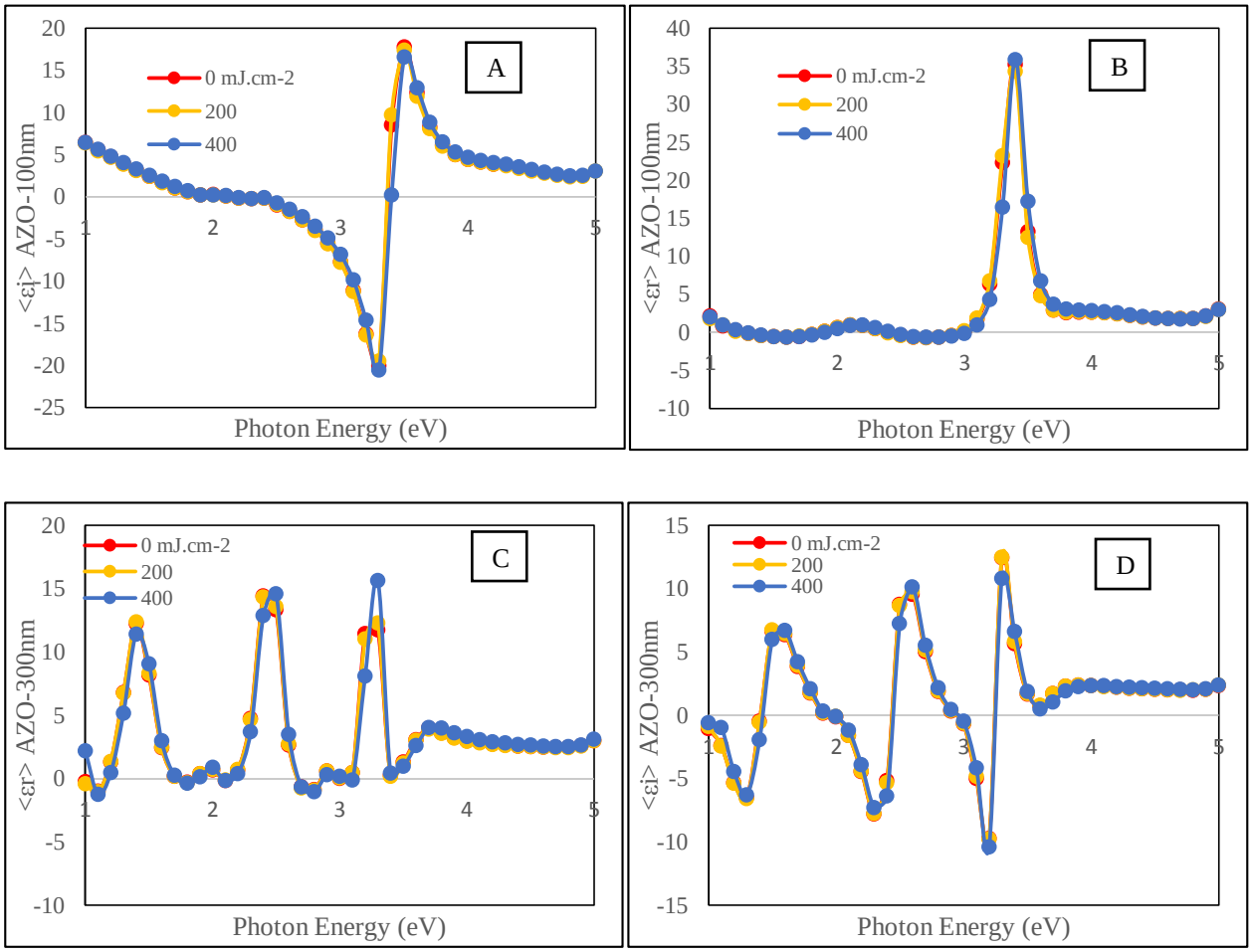

Figure 4-26. Pseudo dielectric functions of AZO-100/Si [A), B)] and AZO-300/Si [C), D)].

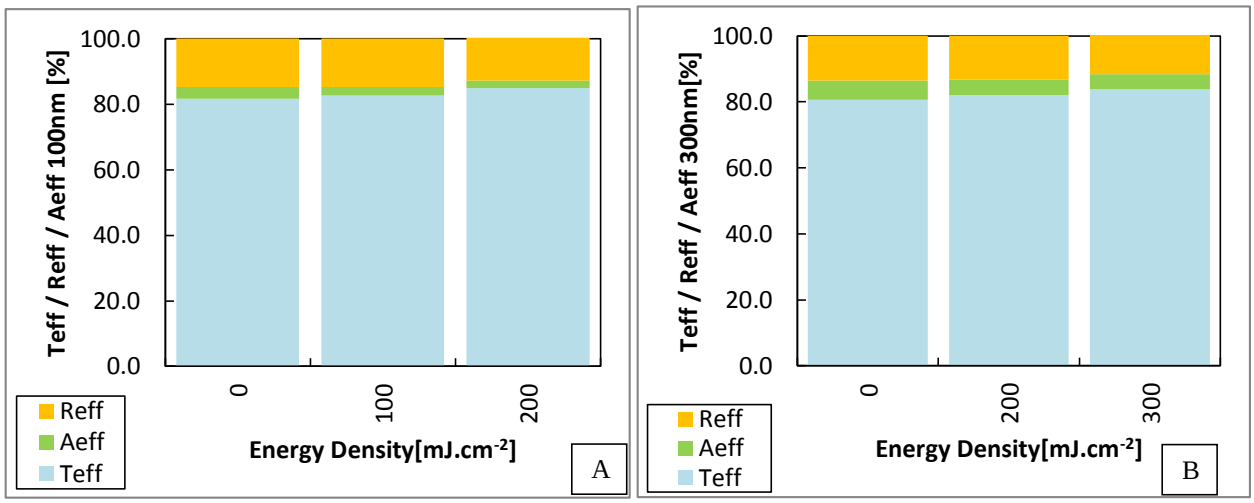

Figure 4-27. Effective Transmission, reflectance and absorption of: A) AZO-100/g; B) AZO-300/g

4.3.3 IOH results

Only some laser treatments and characterizations were made on IOH layers due to the limited quantity of samples, in particular for glass samples. There were three kinds of IOH samples:

- IOH deposited at room temperature onto glass (two samples) and Silicon (IOH-RT). ELA fluences are shown in Table 3-8.
- IOH deposited at 150°C onto glass (only 1 sample) and Silicon (IOH-150°C). ELA fluences are presented in Table 3-10.
- IOH deposited onto Silicon substrates with a SiO2 thin film of 500 nm at RT (IOH-RT/SiO_2/Si). ELA fluences are summarized in
- Table 3-9.

Sheet resistance ($R_{\square}$) measurements were made on all samples as it can be seen in Figure 4-28.A:

- Sheet Resistance of IOH-RT/g increases when applying a fluence of 100 $mJ.cm^{-2}$ In the case of IOH-RT/Si samples, sheet resistance is almost constant for ELAs below

400 mJ.cm^{-2} and a strong degradation can be seen above 400 mJ.cm^{-2} (see Figure 4-28.C).

- Sheet Resistance of IOH-150°C/g does not change when applying a fluence of 100 mJ.cm^{-2}. In the case of IOH-150°C/Si, sheet resistance decreases progressively for increasing laser fluences from 300 mJ.cm^{-2} until 500 mJ.cm^{-2}. An improvement of the sheet resistance is achieved with apparently no damage of the surface of the samples in that range. Unfortunately, we did not have enough IOH-150°C/g samples to make Hall Effect measurements which would have confirmed these observations and explained the improvement of the conductivity with the evolutions of the mobility and concentration of charge carriers. For a laser fluence of 700 mJ.cm^{-2} the layer starts to degrade (see Figure 4-28 C).

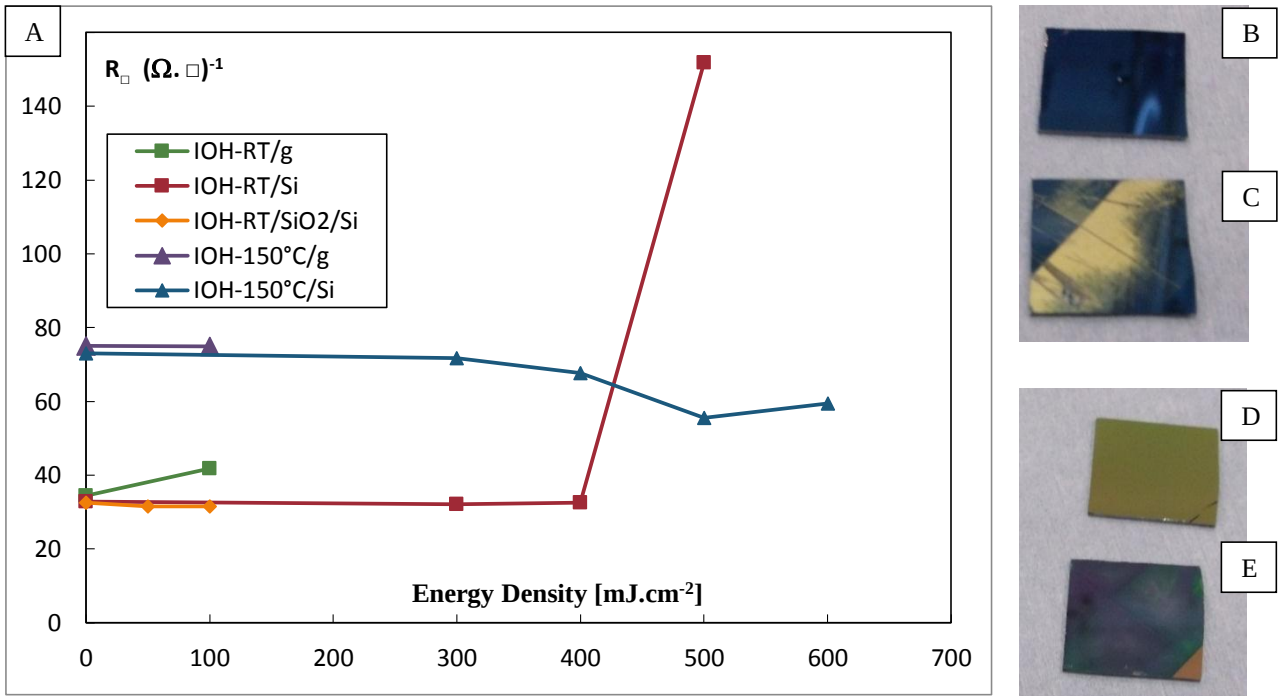

Figure 4-28. A) Sheet resistance of IOH samples for various energy densities. **IOH-150°C/Si**, ELA: 300 (B), 700 mJ.cm^{-2} (C). **IOH-RT/SiO$_2$/Si**, ELA: 50 (D), 300 mJ.cm^{-2} (E).

- Sheet resistance of IOH-RT/SiO_2/Si is almost constant for fluences below 100 mJ.cm^{-2}. When applying a fluence of 300 mJ.cm^{-2}, the layer is degraded (notice the change of color between the corner and the rest of the sample that was laser annealed in Figure 4-28.E) and measurement of the resistance is impossible.

Like for ITO and AZO samples, we observe again a difference in the behavior of electrical properties depending on the substrate. Here in particular, we observe a tremendous difference between Si and SiO_2/Si substrates with a degradation threshold at 700 and 300 mJ.cm^{-2} respectively. The only difference between these two substrates is a 500nm thin layer of SiO_2. This comforts the hypothesis that different substrates evacuate heat at different rates. That is why at 300 mJ.cm^{-2}, the laser annealed IOH-RT films suffer different changes on silicon compared to SiO_2/Si substrates as it is shown in Figure 4-28.B (almost no visual change compared to the reference without ELA) and in Figure 4-28.E (sample color changed compared to the reference) respectively.

Reflectance (Figure 4-32 and Figure 4-31) of IOH/Si samples and pseudo dielectric functions (Figure 4-29) were measured to have an idea of the change in optical properties after laser annealing:

- IOH-RT/Si: there is no net change in Reflectance for laser fluences below 400 mJ.cm^{-2}. As of 500 mJ.cm^{-2}, one can observe a change in the reflectance that can probably be attributed to the degradation of the film as some fractures were seen on the film. An important change in the dielectric function can also be observed for fluences superior to 400 mJ.cm^{-2} again probably resulting from the degradation of the layer.
- IOH-150°C/Si: Reflectance is almost constant for laser fluences below 600 mJ.cm^{-2} in the spectral range of interest of the cell. However one can see an increase in the reflectance in the near-IR range that could originate from a change in carrier concentration. Unfortunately we don't have any Hall Effect data to confirm this hypothesis. Furthermore no changes can be seen in pseudo dielectric function for any of the tested energy densities (see Figure 4-29.E and F).

- IOH-RT/SiO_2/Si: For ELAs below 200 $mJ.cm^{-2}$. Reflectance is almost constant for the photovoltaic range of interest but a shift can be noticed in the IR range that could result from a change in carrier concentration, as can be seen in Figure 4-31. For ELA at 300 $mJ.cm^{-2}$, there is a reduction of the number of oscillations in the Reflectance spectra, which probably indicates a reduction of the thickness of the IOH thin film. This thickness reduction could originate from a partial ablation of the IOH layer by the laser.

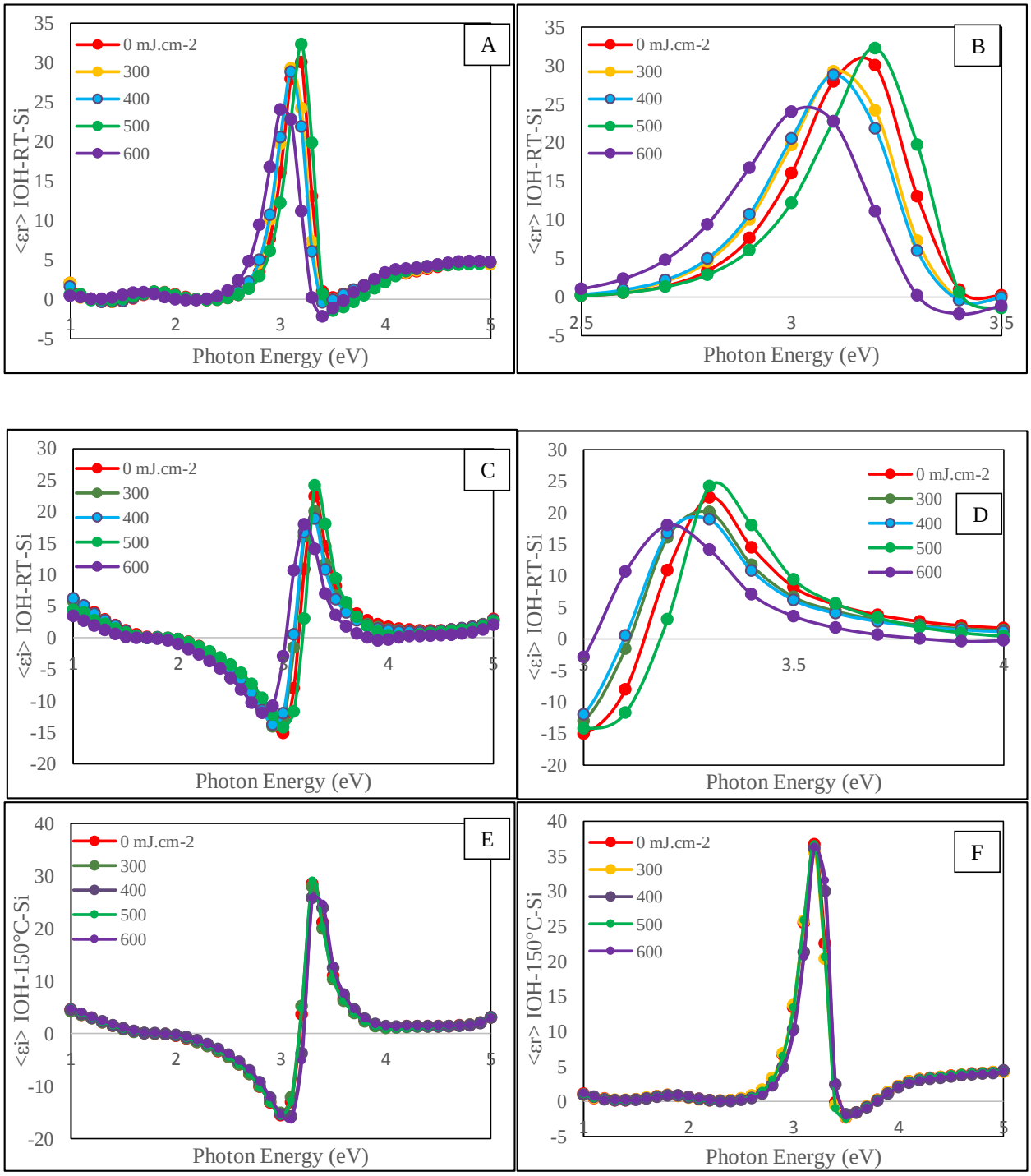

Figure 4-29. Pseudo dielectric functions after laser annealing of IOH-RT/Si [A), C)], Zoom [B), D) respectively] and of IOH-150°C/Si [E), F)].

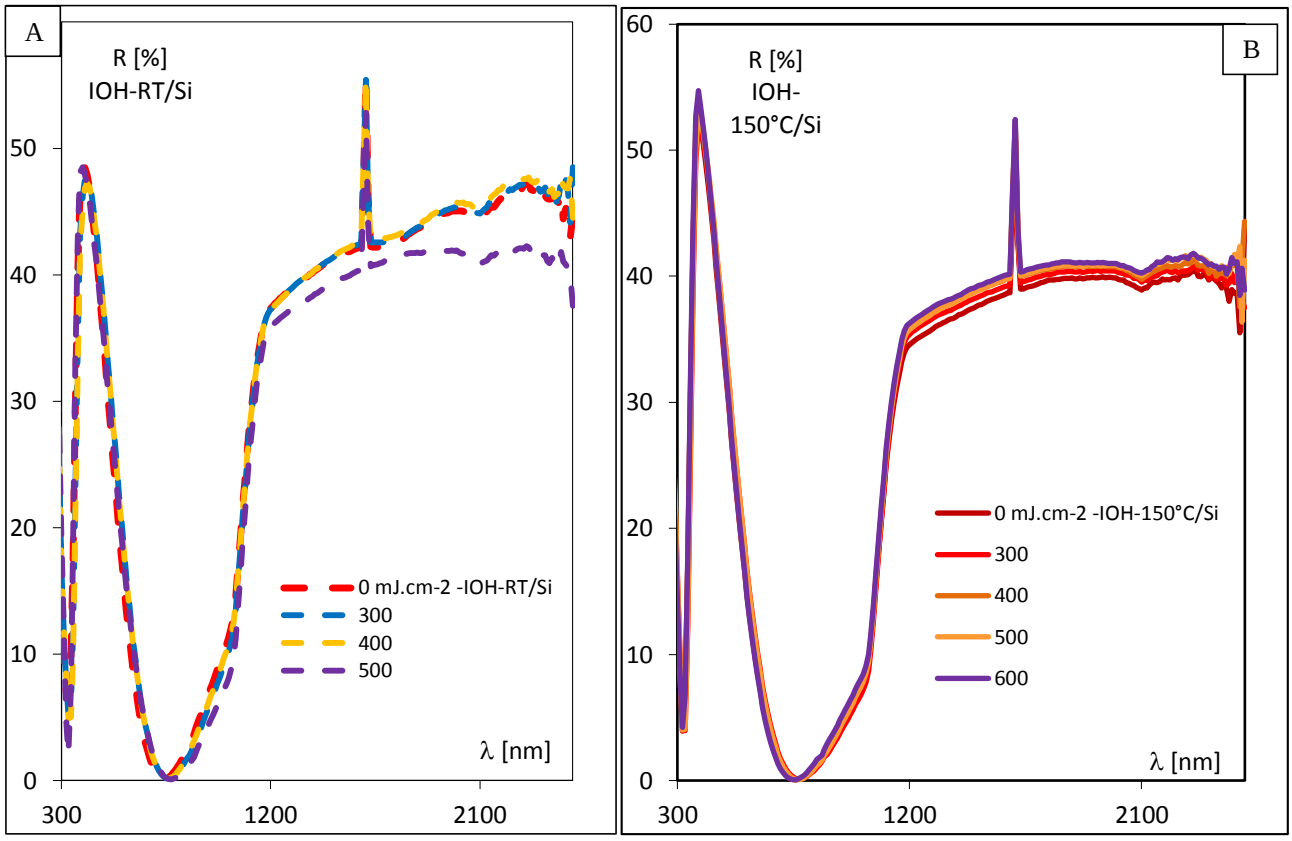

Figure 4-30. Reflectance after laser annealing of A) IOH-RT/Si, B) IOH-150°C/Si.

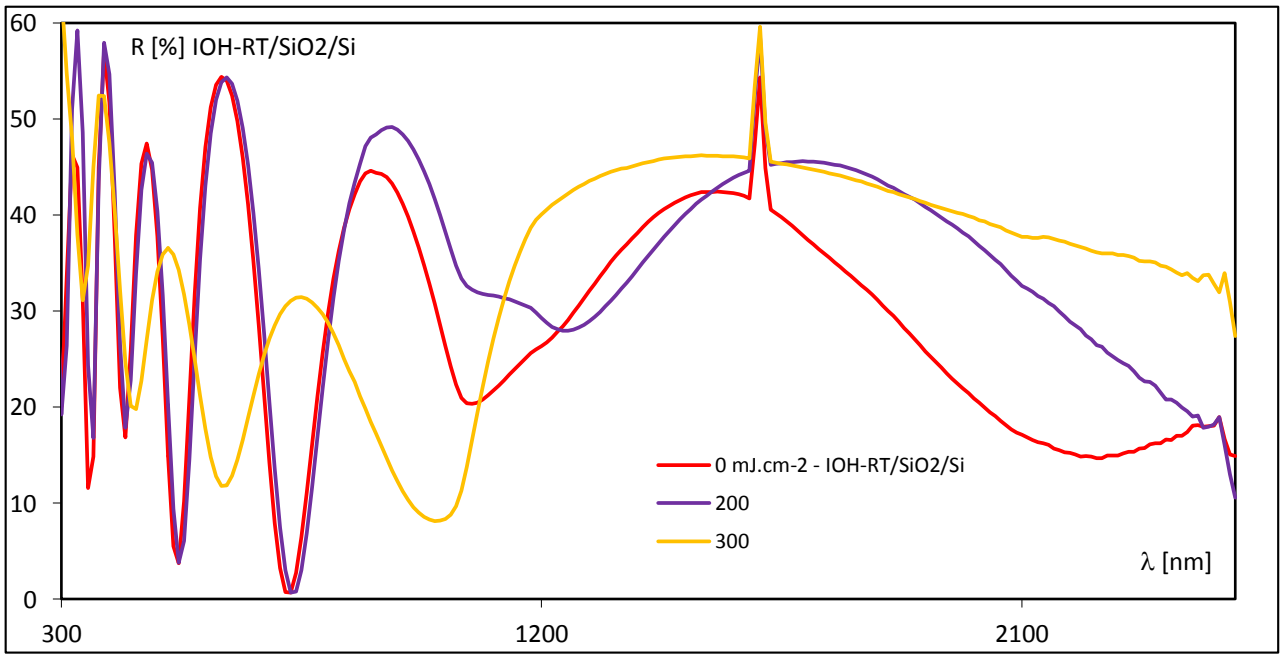

Figure 4-31. Reflectance after laser annealing of IOH-RT/SiO_2/Si.

4.4 Conclusions of Chapter N°4

4.4.1 ITO

4.4.1.1 ITO/g samples

1. The electrical properties (electrical conductivity, carrier mobility and concentration) of ITO/g samples continuously and significantly increase after excimer laser annealing for laser fluences in the range of [175, 300] $mJ.cm^{-2}$ (see Figure 4-10 and Figure 4-13):

σ $(\Omega.cm)^{-1}$		**μ** $cm^2V^{-1}s^{-1}$		**N** cm^{-3}	
Before	After	Before	After	Before	After
991.93	2480	35.9	49.97	1.92×10^{20}	3.1×10^{20}

Table 4-5. Electrical conductivity, carrier mobility and concentration of ITO/g samples before and after a laser annealing of 300 $mJ.cm^{-2}$

Although sheet resistance decreases, the sheet resistance homogeneity slightly degrades as can be seen in Figure 4-11.B. Besides there is no change in sheet resistance after repetitive shots with the same laser fluences which means that there is no accumulative effect of ELA (see Figure 4-12).

2. The optical properties of ITO/g samples in the spectral range of interest of a solar cell improve after laser annealing for energy densities in the range of [250, 400] $mJ.cm^{-2}$ as it can be seen in Figure 4-17.A where Teff increases, Reff decreases and Aeff remains constant.

3. Degradation of ITO/g samples can be seen for laser fluences above 300 mJ.cm^{-2}. This can be seen with naked eye (Figure 4-10.B) or with the drastic decrease of the conductivity (Figure 4-13.A).

4. There is an improvement of both optical and electrical properties of laser-annealed ITO/g samples for laser fluences between 250 and 300 mJ.cm^{-2} with an optimum at 300 mJ.cm^{-2} where the sheet resistance is 43 Ω. □$^{-1}$ and Teff. 81.41%.

5. SEM observations have shown that there is almost no change in thin films surfaces below 300 mJ.cm^{-2} laser treatment. For values above 500 mJ.cm^{-2}, ITO thin film starts to melt (see Figure 4-18 B and I).

4.4.1.2 ITO/Si samples

6. Unlike for ITO/g samples, Sheet resistance only slightly decreases for the range <250,500> mJ.cm^{-2} for ITO/Si samples (Figure 4-10.A). A degradation of the sample is visible to the naked eye for a laser fluence of 1000 mJ.cm^{-2} (Fig. 4-10.C). There is no change in n and k coefficients for energy densities below 325 mJ.cm^{-2} meaning that the optical properties suffer almost no modification upon ELA, contrary to what was observed by spectrophotometry on ITO/g samples (see Figure 4-17.B and Figure 4-17.C).

7. SEM observations showed that there is almost no change in thin films surfaces below 500 mJ.cm^{-2}. For values above 500 mJ.cm-2, thin film starts to crack (see Figure 4-18 G). For values above 750 mJ.cm^{-2}, ITO thin film starts to melt (see Figure 4-18 H and J).

4.4.2 AZO

4.4.2.1 AZO-100nm

1. For AZO-100/g: Unlike for ITO layers, Sheet resistance slightly decreases from 160 to 147 Ω. $\square^{-1}$ for laser fluences below 200 mJ.cm^{-2}. Thin film damage can be seen above 200 mJ.cm^{-2}. There is an increment of the concentration of free carriers (N) below 300 mJ.cm^{-2} that is compensated by a decrease in mobility, contrary to what was observed on ITO/g samples. This is also supported by the increment of the optical band gap observed in the Tauc-plots (Burstein-Mott effect).

2. For AZO-100nm/Si: Sheet resistance has a minimum value of 78 Ω. $\square^{-1}$ for an ELA at 100 mJ.cm^{-2}. Pseudo dielectric function does not change for energy densities below 400 mJ.cm^{-2} (see Figure 4-26.A and Figure 4-26.B) which confirms that there is almost no change in n and k coefficients.

3. Like ITO layers, AZO layers behave different with ELA depending on the substrate.

4.4.2.2 AZO-300nm

4. For AZO-300/g: Sheet resistance slightly increases for laser fluences above 200 mJ.cm^{-2}, and samples start to degrade for laser fluences above 300 mJ.cm^{-2}. There is also an augmentation of N for laser annealing below 300 mJ.cm^{-2} which can be confirmed with the slow increment of the optical band gap in the Tauc-plots.

5. For AZO-300/Si: Values of sheet resistance, pseudo dielectric function do not change up to a laser fluence of 400 mJ.cm^{-2} where the film starts to degrade.

4.4.3 IOH

4.4.3.1 IOH-RT

1. For IOH-RT/g samples the sheet resistance remains almost constant when annealing at a laser fluence of 100 mJ.cm^{-2}. We could not make more ELA treatments because of the lack of samples.

2. For IOH-RT/Si samples, sheet resistance is almost constant for laser annealing below 400 mJ.cm^{-2} and then drastically increases because of the degradation of the film. Reflectance spectra are also the same in the same range of laser fluences, meaning that there is almost no influence of ELA on IOH samples made at room temperature.

4.4.3.2 IOH-150°C/Si

3. For IOH-150°C/g samples, sheet resistance remains almost constant when applying a laser fluence of 100 mJ.cm^{-2}. We could not make more ELA treatments because of the lack of samples.

4. For IOH-150°C/Si samples, there is an improvement of the electrical properties (sheet resistance decreases) when increasing the laser fluence from 0 to 500 mJ.cm^{-2}. However we cannot confirm whether this improvement was due either to carrier concentration or mobility (or both) increase because of the lack of glasses substrates to make Hall Effect measurements. Reflectance spectra are almost the same in the range 300-1200 nm for laser fluences below 400 mJ.cm^{-2}, which would indicate that optical properties (n and k) do not change in the spectral range of the solar cell interest with these energy densities.

4.4.3.3 IOH-RT/SiO_2/Si

5. Sheet resistance remains constant for laser fluences below 100 mJ.cm^{-2} and above this value the IOH-RT thin films degrade as can be confirmed by the diminution of the number of oscillations in reflectance spectra as a consequence of the reduction of the thin film thickness probably due to a partial ablation of the layer.

6. Like ITO and AZO layers, IOH layers behave differently depending on the substrate and in particular, the fact of adding a thin layer of SiO2 (500 nm) on Si substrate leads to a dramatic difference in the behavior of the IOH layers. As it was explained before, this can account for our hypothesis of how different substrates evacuate heat from TCOs at different rates depending on their thermal conductivity.

5 CHARACTERIZATION OF HET PHOTOVOLTAIC CELLS TREATED BY ELA

In this chapter, R&D and Pilot line HET solar cells are described and characterized. The results that are showed here were the main motivation of the internship at INES. First of all, the two different solar cel types treated with ELA are presented, then some of the characterization techniques used in the R&D clean room are described and finally the results and observations from characterization are analyzed, the conclusions are exposed in the next chapter.

5.1 HET solar cells

In chapter 2, the main steps of the fabrication of a crystalline silicon HET solar cell and its principal characteristics have been mentioned (see Figure 2-10). In this chapter, the results of the ELA treatments of R&D and Pilot line HET solar cell are presented.

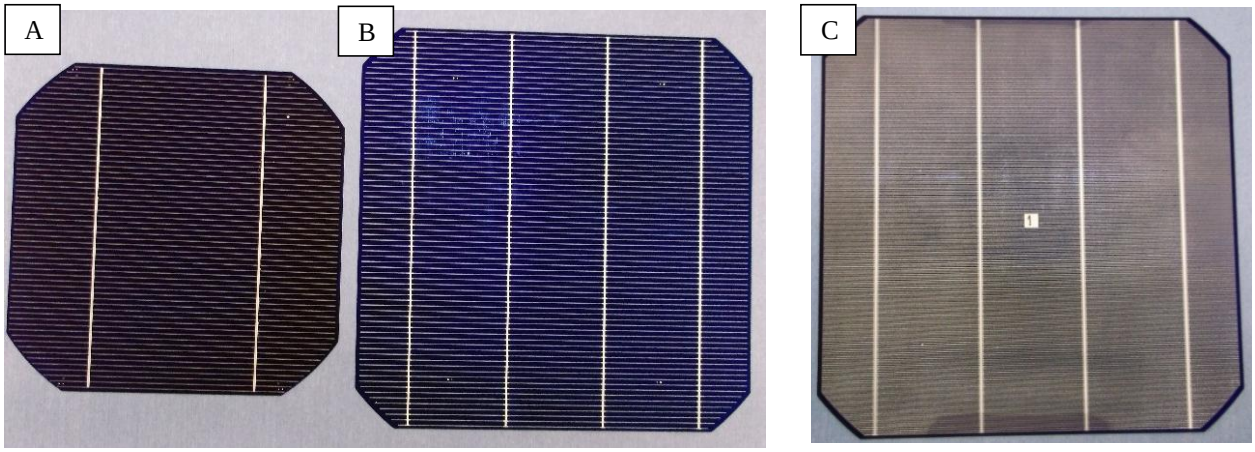

Figure 5-1. A) Restaure HET solar cell (Front Side). Pilot line HET solar cell: B) Front side, C) Rear side

An R&D HET solar cell is shown in Figure 5-1.A. This kind of solar cell has two bus bars and a size of 125 mm pseudo square whereas Pilot line HET solar cell has four bus bars and a size of 156 mm pseudo-square. The rear side of a Pilot line HET solar cell is presented in Figure 5-1.C, it can be seen that there are more fingers on this side, since the transparency of the rear side of a solar cell is a smaller constraint than the transparency of the front side as most of the light will reach the cell at the front side (The configuration of fingers and busses is the same for inverted and standard emitter HET solar cell).

5.2 Characterization Tools

In this section, the techniques used in common for laboratory and industrial characterization of solar cells will be described. Some of them are: measurement of charge carriers' lifetime (Passivation indicator), measurement of the I-V characteristic curve, and pseudo fill factor measurement

5.2.1 Lifetime tester (SINTON device)

The photoconductance lifetime tester WCT-120 of Sinton® Consulting is an electric device which measures the life time of minority charge carriers easily and without contacts. This equipment has three main parts as can be seen in Figure 5-2.A. A Flash lamp which illuminates the sample, a RCL circuit that measures the variation of conductivity in the sample (variation in the number of minority carriers) by measuring the inductive currents in the inductive coil of the RCL circuit and a reference solar cell which measures the incident light intensity.

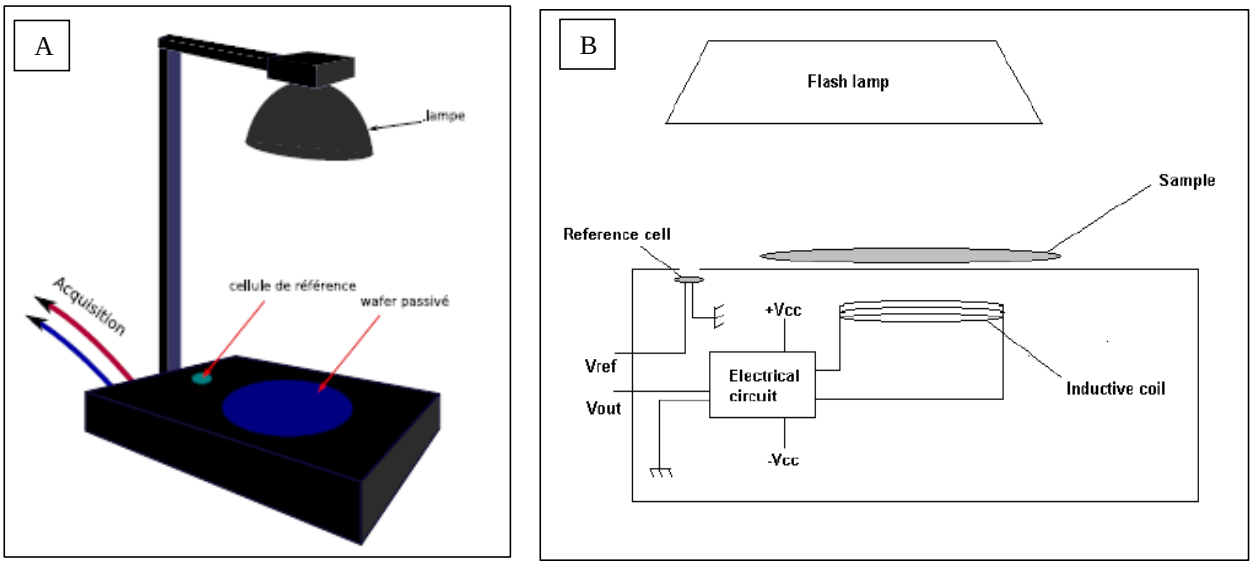

Figure 5-2. A) Part of the lifetime tester WCT-120. B) Simplified diagram of main parts of WCT-120: Flash lamp, RCL circuit (inductive coil) and Reference cell (Favre, 2011)

The variation of conductivity can be related to the increment of the number of minority charge carriers by the following equation (a p-type wafer is supposed as sample):

$$\Delta\sigma = q\left(\Delta n.\mu_n + \Delta p.\mu_p\right) = q\ \Delta n\ (\mu_n + \mu_p) \qquad (5\text{-}1)$$

Since the same number of electrons and holes are generated ($\Delta n = \Delta p$). If the generation rate (G) is known with the reference cell, the life time of minority carriers (τ_{eff}) can be calculated as follows:

$$\frac{d\Delta n}{dt} = G - R = G - \frac{\Delta n}{\tau_{eff}} \qquad (5\text{-}2)$$

with *R* the recombination rate.

The WCT-120 equipment can calculate directly the life time, it is only necessary to enter the resistivity and thickness and select the correct mode of measurement. The modes of WCT-120 are the following:

5.2.1.1 Inductively coupled photoconductance decay mode (IC-PCD) [Short Flash]

If the evolution in time of Δn is known, the change of rate $\frac{d\Delta n}{dt}$ (tangent to the curve) is also known. Last, the life time of minority charge carriers is calculated by using the eq.(5-2). This mode is used for life times larger than ~200 µs.

5.2.1.2 Quasi-Steady State Photo Conductance mode (QSSPC) [Long Flash]

If the time life of charge carriers is shorter than ~200 µs, a longer flash is used to work in a quasi-stationary situation: this can be seen as if the charge carrier concentration would not change in time i.e $\frac{d\Delta n}{dt} = 0$ and from eq. (5-2): $\tau_{eff} = \frac{\Delta n}{G}$

This equipment can also calculate an open circuit voltage with:

$$V_{OC} = \frac{kT}{q} \, ln\left(\frac{(N_d + \Delta n)\Delta n}{n_i^2}\right) \quad (5\text{-}3)$$

Where $\frac{kT}{q} = 25.69$ mV, $n_i^2 = 7.4\text{x}10^{19}$ cm^{-6} (T=298K) and N_d is the doping atom concentration which is calculated from resistivity entered by the user. (Favre, 2011).

5.2.2 Solar Simulator (I-V curve)

The solar simulator is an instrument which measures the current vs. voltage in a solar cell. Its main parts are: a lamp that simulates the A.M 1.5 spectral irradiance at a 1000W.m^{-2} power density, a system to maintain the sample temperature at 25°C, a variable load resistance(R_L), a variable source of voltage, an ampere-meter and a voltmeter (see Figure 5-3).

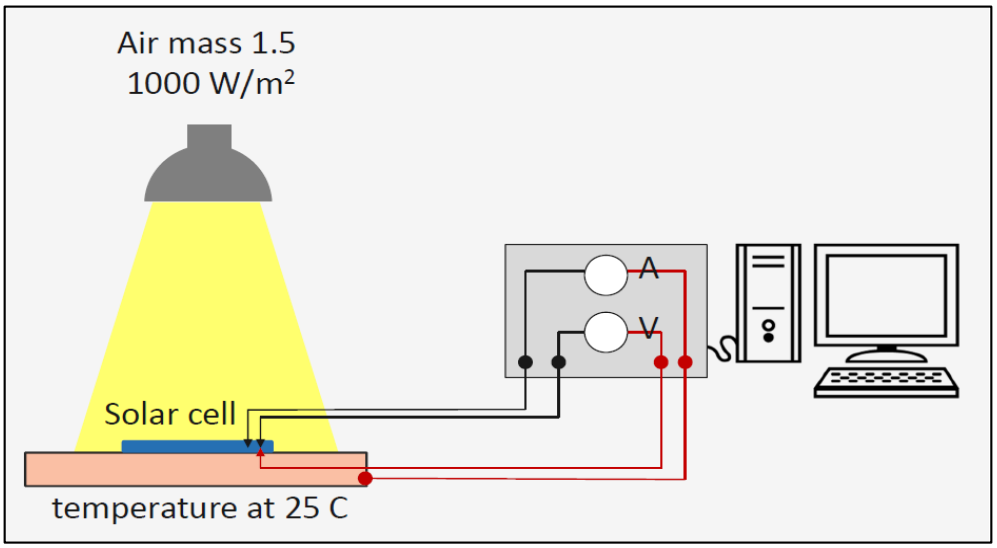

Figure 5-3. Schema of the solar simulator working under illumination for standard conditions: A.M. 1.5, T=25°C.

5.2.2.1 *Measurement of the I-V curve under illumination*

A solar cell under illumination generates a voltage and a current. To measure the I-V curve, it is necessary to connect the solar cell to a variable resistance (R_L) and measure the current and voltage while the resistance is changing, as result a value of current is measured for each value of voltage. For example, if R_L~0, then $I_{measured}=I_{sc}$ and $V_{measured}=0$ or if R_L is very large, then $I_{measured}=0$ and $V_{measured}=V_{oc}$. A common diagram obtained after this measurement is presented in Figure 5-4.A. Other external parameters that can be taken from this measurement are the maximum peak power density, fill factor and the efficiency.

5.2.2.2 *Measurement of the I-V curve under obscurity*

A solar cell is also a diode that is why the current can be measured in the HET solar cell while an external voltage is applied to the solar cell under no illumination. For this measurement, a cover is used to be sure that no external light illuminates the solar cell. Then, the Shunt resistance (R_{sh}) and the series resistance (R_s) are calculated with a fitting software.

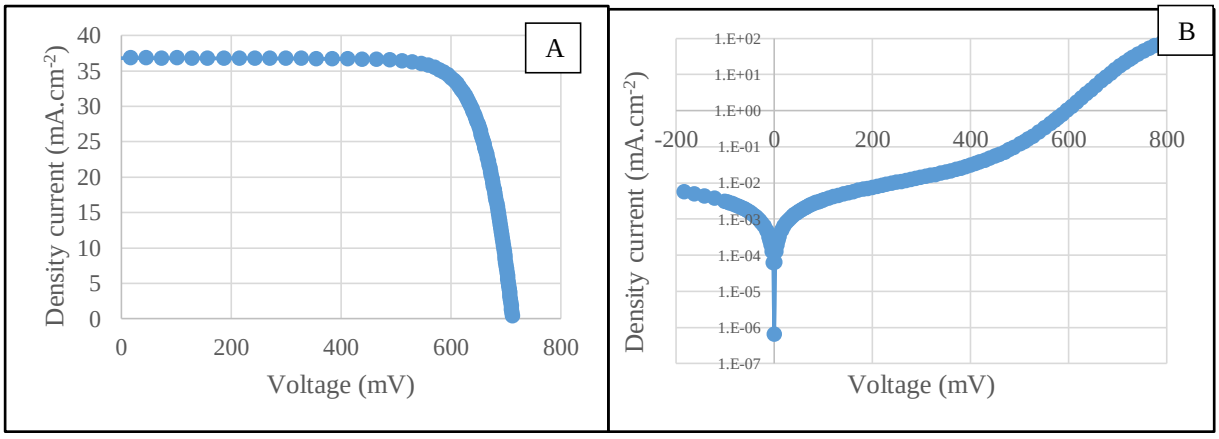

Figure 5-4. A) J-V Characteristic curve of a HET solar cell. B) Dark J-V curve of a HET solar cell.

5.2.3 Pseudo Fill Factor (SunsVoc device)

The device used for this measurement is almost the same as the SINTON device described in section 5.2.1 proposed by the same constructor. The main parts of SunsVoc are: The flash lamp, a reference solar cell which measure the incident light flux, a copper plate which is in contact with the rear side of the sample (solar cell) and a metallic probe hold by the user which is in contact with the front side of the sample (see Figure 5-5).

The SunsVoc device determines primarily the life time charge carriers by measuring the open circuit voltage for different values of incident flux (injection level). Furthermore, SunsVoc device can reproduce an illuminated I(V) measurement, by using the variation of open circuit voltage and of the illumination without taking into account the losses due to series resistances: this allows to calculate the so-called pseudo-fill factor (pFF). The comparison of the FF and the pFF is then a good way to control the quality of TCO thin films and screen printing metallization (Favre, 2011).

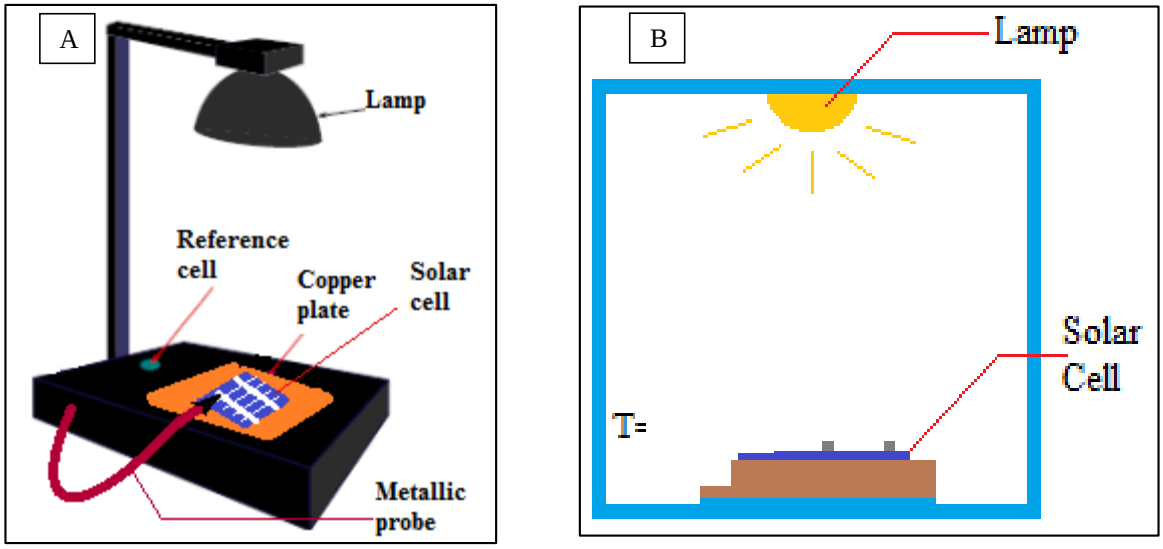

Figure 5-5. A) Principal parts of SunsVoc equipment. B) Schema of aging chamber for solar cells

5.2.4 Solar cell aging

After laser annealing and characterization, the cells were put in an aging chamber to check the evolution of their performances when submitted to illumination during a long time. (see Figure 5-5.B)

5.3 Results of IP-ITO samples

First of all, precursors (IP-ITO) of ITO/a-Si:H(p)/ a-Si:H(i)/c-Si(n)/a-Si:H(i) with c-Si(n) as substrate (150 µm-thick), were fabricated to measure the impact of ITO laser annealing on Silicon interfaces passivation (see Figure 5-6). The life time of charge carriers on c-Si decreases by ~250 µs for laser annealing below 400 mJ.cm^{-2} which may indicate a slight degradation in passivation. The open circuit voltage also decreases by ~10 mV for laser fluences ł w 400 mJ.cm^{-2}. For ELAs above 400 mJ.cm^{-2}, a much larger diminution of life time and V_{oc} is measured which indicate a high degradation of the passivation (see Figure 5-7).

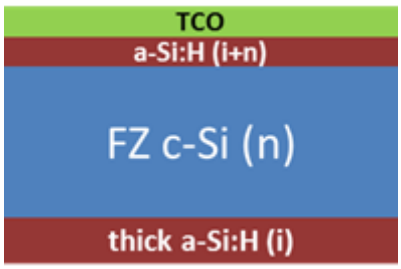

Figure 5-6. Schema of precursor IP-ITO.

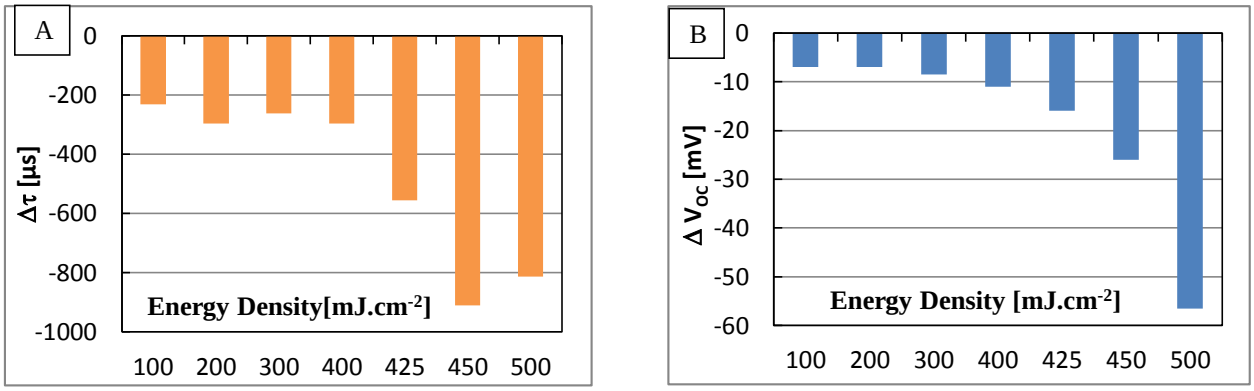

Figure 5-7. Variation before and after laser annealing for IP-ITO precursors: A) Life time variation vs. Energy Density. B) V_{OC} variation vs. Energy Density

5.4 Pilot line HET solar cells

In the following section, the four most important parameters of Pilot line solar cells are described: V_{OC}, J_{SC}, FF and η.

5.4.1 V_{OC} results of Pilot line HET solar cells

There is a very small diminution of V_{OC} for laser fluences below 400 mJ.cm^{-2}, see Figure 5-8. A and B. However there is a huge decrease in open circuit voltage for values above 400 mJ.cm^{-2}.

There is a greater diminution when performing ELA on the rear side than on the front side,which is consistent with the fact that the junction (the fundamental part in a solar cell) is situated at the rear side. This can be explained by the diminution of passivation at the a-Si:H/c-Si interface as it was observed on the precursors in section 5.3 (see Figure 5-8. C).

The aging mechanism shows a little improvement of the V_{OC} (see Figure 5-8.D) because of possible reordering of Hydrogen atoms in the amorphous silicon structure. However, in the case of high energy ELA, full recovery of the passivation was not possible by aging showing that the a-Si:H was probably strongly affected by ELA:

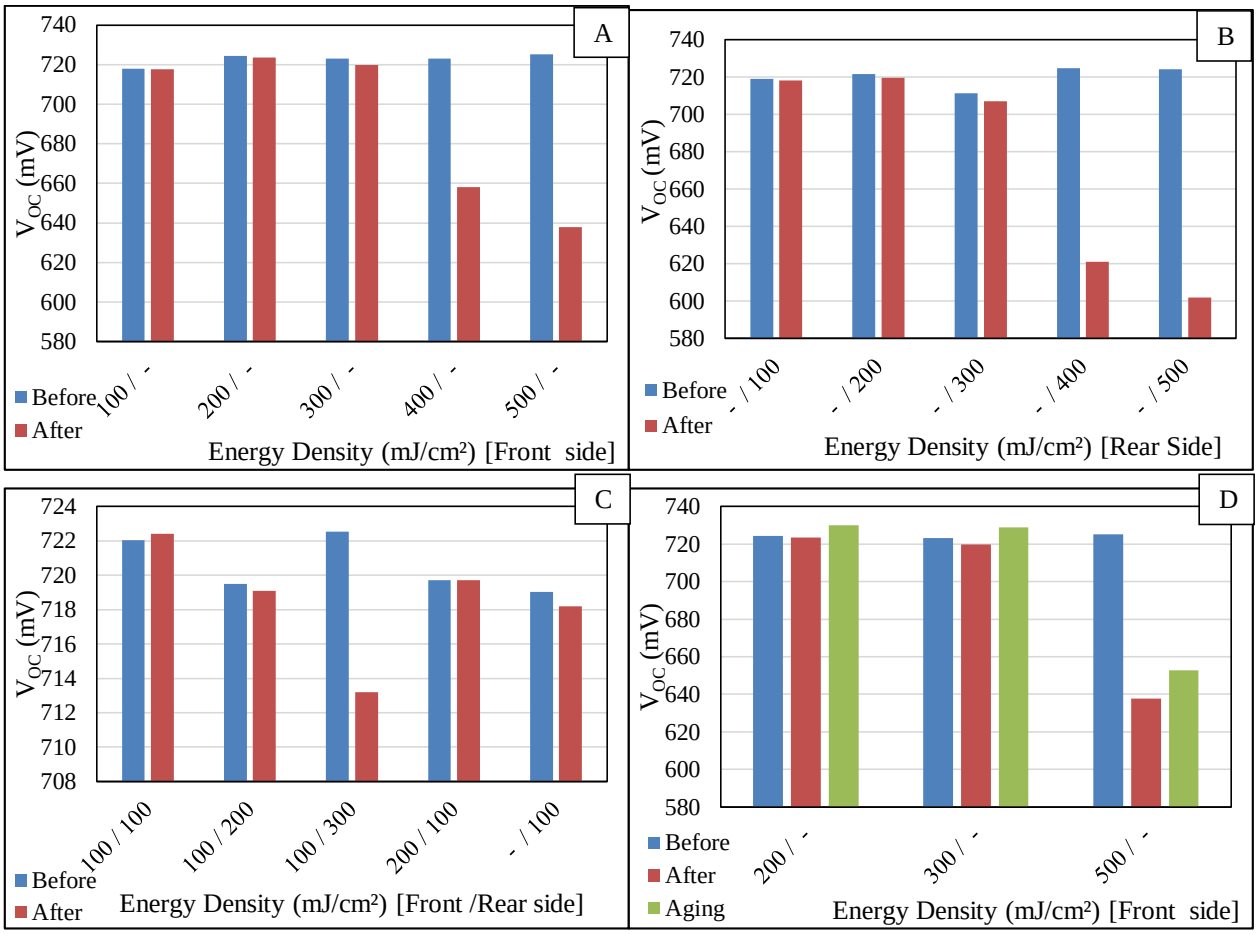

Figure 5-8. Open Circuit Voltage (V_{OC}) vs. laser fluences applied to: A) Front side, B) Rear Side and C) Front and Rear sides of PILOT LINE HET solar cells. D) Aging results of Front side laser annealed solar cells.

5.4.2 J_{SC} results of Pilot line HET solar cells

The Jsc drops down for front side laser treatments above 400 mJ/cm² (see Figure 5-9.A), however there is almost no changes for Rear side treatments below 500 mJ/cm² (see Figure 5-9.B). This can be explained by two reasons: the diminution of the passivation by amorphous silicon due to its degradation which leads to recombination of electrons with holes at the front side and thus the diminution of collected charges, and/or to the degradation of ITO as it was observed in section 4.3.1 for highly energetic laser treatments and thus of its antireflecting properties.

The laser treatment at both sides of the solar cell does not produce any visible change in Jsc (see Figure 5-9.C) because laser annealing was made below 300 $mJ.cm^{-2}$.

Aging produces almost no change in J_{SC} for the cells that were annealed at 200 and 300 mJ/cm². However an increment of more than 1 mA/cm^2 is observed after aging for the cell that was annealed at 500 mJ/cm² as it can be seen in Figure 5-9.D.

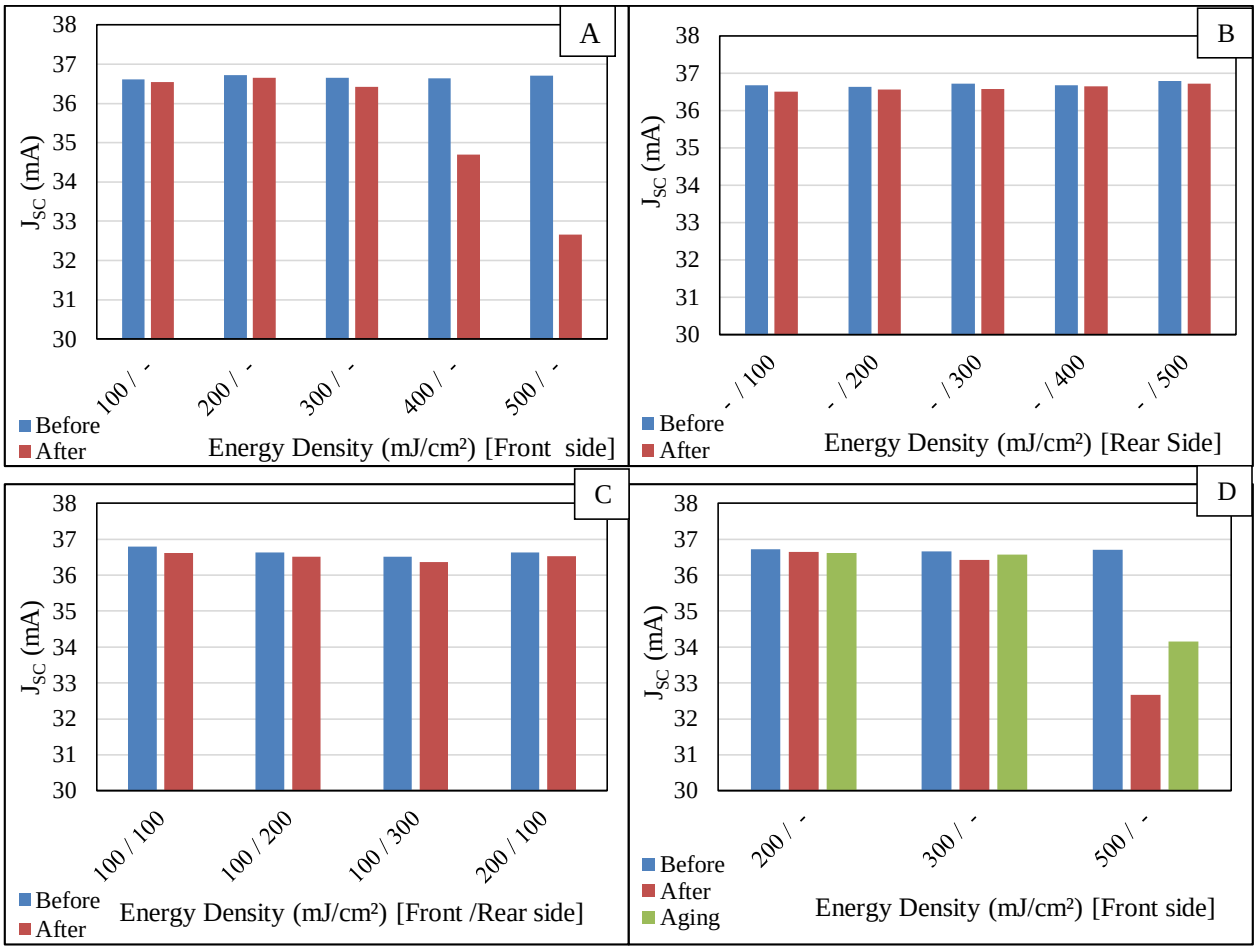

Figure 5-9. Short Circuit Current (J_{SC}) vs. laser fluences applied to: A) Front side, B) Rear Side and C) Front and Rear sides of PILOT LINE HET solar cells. D) Aging results of Front side laser annealed solar cells.

5.4.3 Fill Factor results of Pilot line HET solar cells

In the case of Fill Factor there is a little increment for front side laser treatments above 200 mJ/cm² that might be a result of improvement in ITO conductivity (see Figure 5-10. A). However there is a huge decrease of the FF for rear side laser treatments above 300 mJ/cm² (see Figure 5-10 B).

The FF drops down for rear side treatments probably because p-n junction is damaged by ELA as it was observed for the V_{OC}. This is confirmed for double side laser treatment of 100 mJ/cm² (front side)/300 mJ/cm² (rear side), see Figure 5-10.C, where higher laser fluence in rear side produces a drop in FF.

After Aging step, there is an increment for cells treated with laser fluences below 300 mJ/cm². However the cell treated with 500 mJ/cm² experiments a degradation of the FF upon aging step.

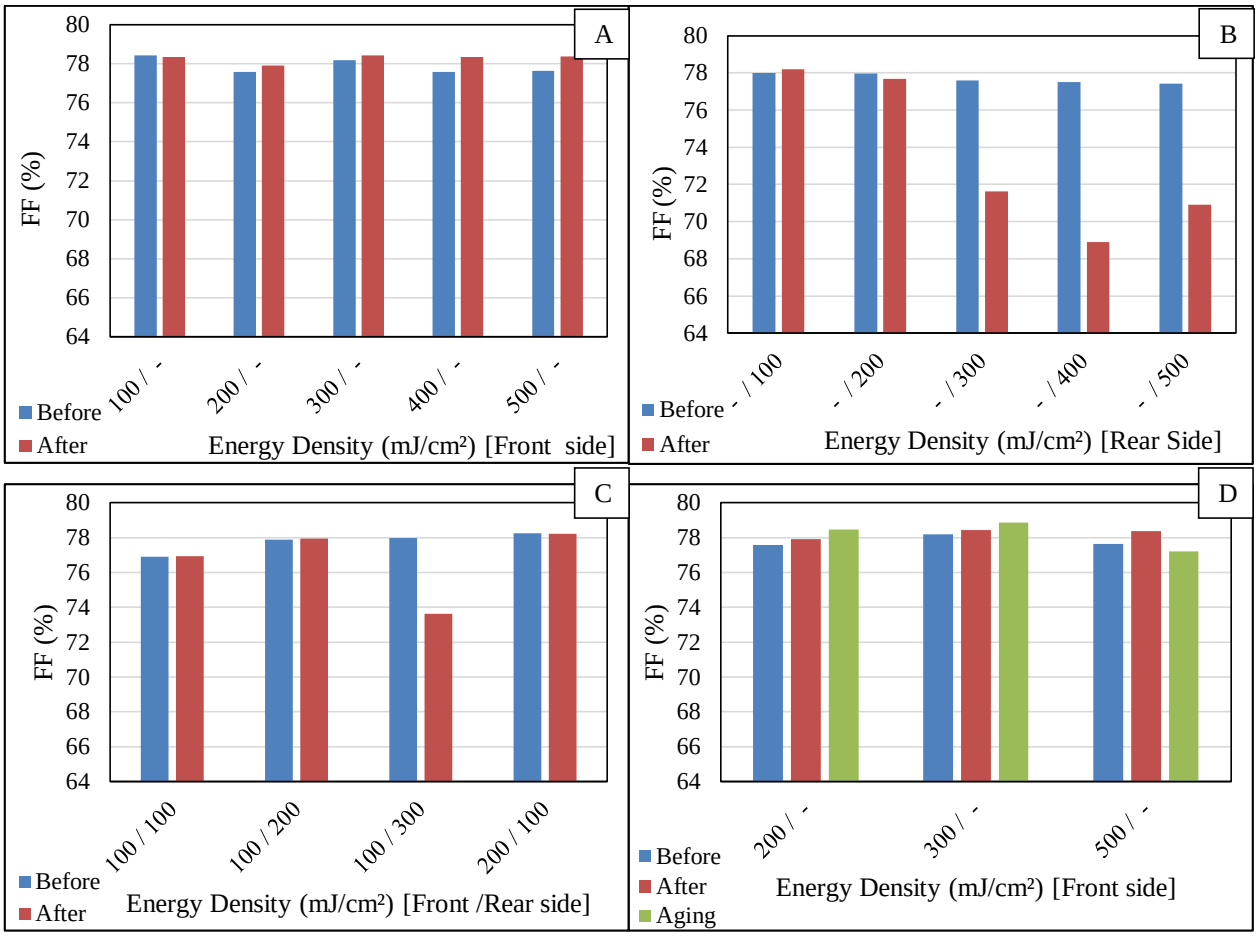

Figure 5-10. Fill Factor (FF) vs. laser fluences applied to: A) Front side, B) Rear Side and C) Front and Rear sides of PILOT LINE HET solar cells. D) Aging results of Front side laser annealed solar cells.

5.4.4 Efficiency results of Pilot line HET solar cells

There is a huge degradation of the efficiency for laser treatments of front or back side above 300 mJ/cm² (see Figure 5-11.A and Figure 5-11.B) as a result of the voltage drop combined to either current (for front side) or FF degradation (for back side).

For double side treatment, there is almost no change in efficiency for ELA below 200 mJ/cm² (see Figure 5-11.C). However the efficiency decreases when ELA exceeds this limit on one side.

After aging step, there is almost no change efficiency even for cells that were treated with ELAs below 300 mJ/cm², see Figure 5-11.D).

The efficiency cell treated with ELA at 500 mJ/cm² slightly recovers upon aging but still remains well below initial efficiency.

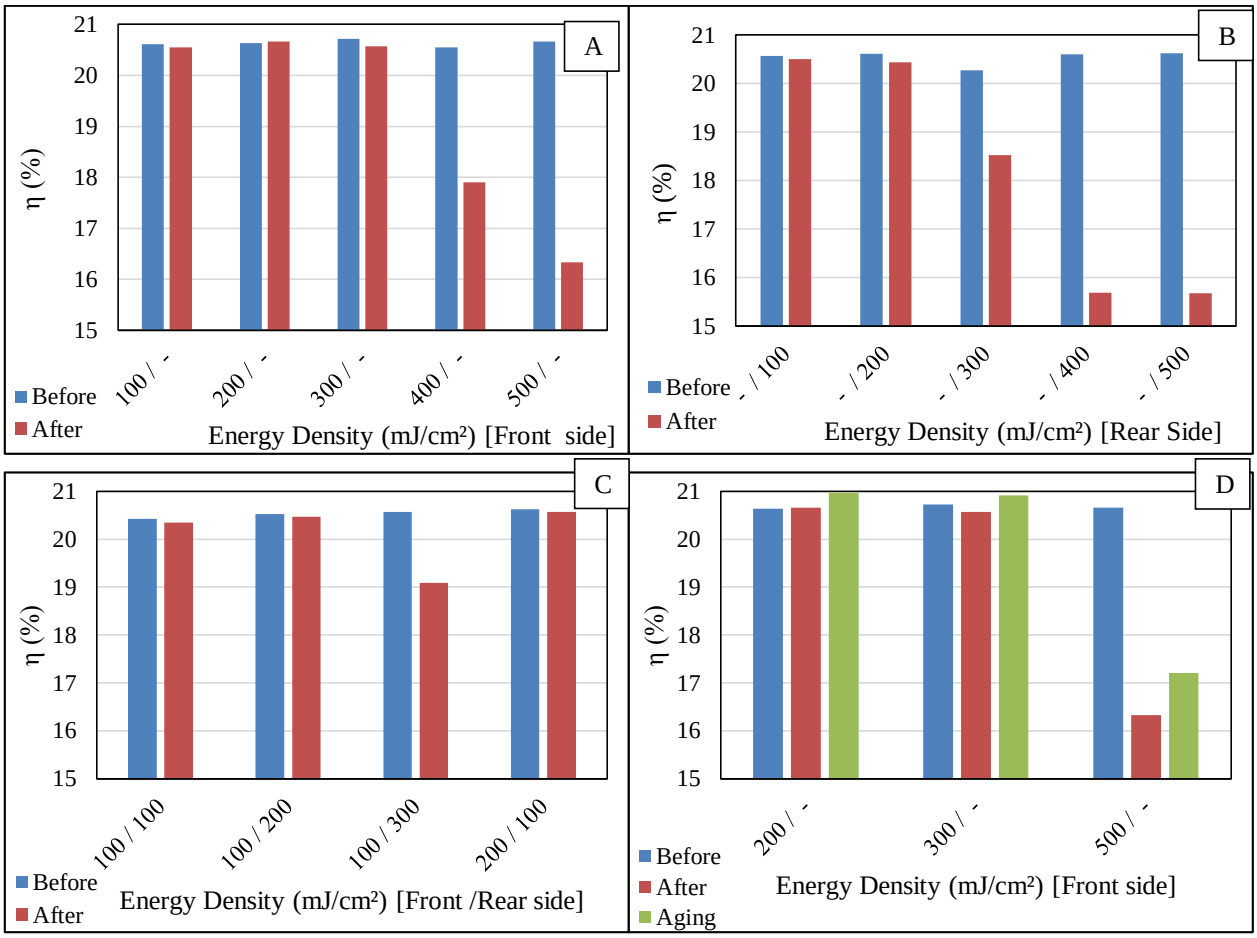

Figure 5-11. Efficiency (η) vs. laser fluences applied to: A) Front side, B) Rear Side and C) Front and Rear sides of PILOT LINE HET solar cells. D) Aging results of Front side laser annealed solar cells.

5.5 R&D HET solar cells

In this section, the external parameters of R&D HET solar cells are described. The laser fluences were chosen after having tested pilot line solar cells. This is why we only used laser fluences below 250 mJ/cm² for front side treatments and below 200 mJ/cm² for rear side laser treatments.

5.5.1 V_{OC} results for R&D HET solar cells

In all cases, V_{OC} only very slightly decreases after ELA treatments (see Figure 5-12.A and Figure 5-12.C): the change in V_{OC} can be seen in Figure 5-12.B (for front side treatments) and Figure 5-12.D (rear side treatments) where we see that it is kept very low probably due to limited damage in amorphous silicon thin films at the low tested ELA energies.

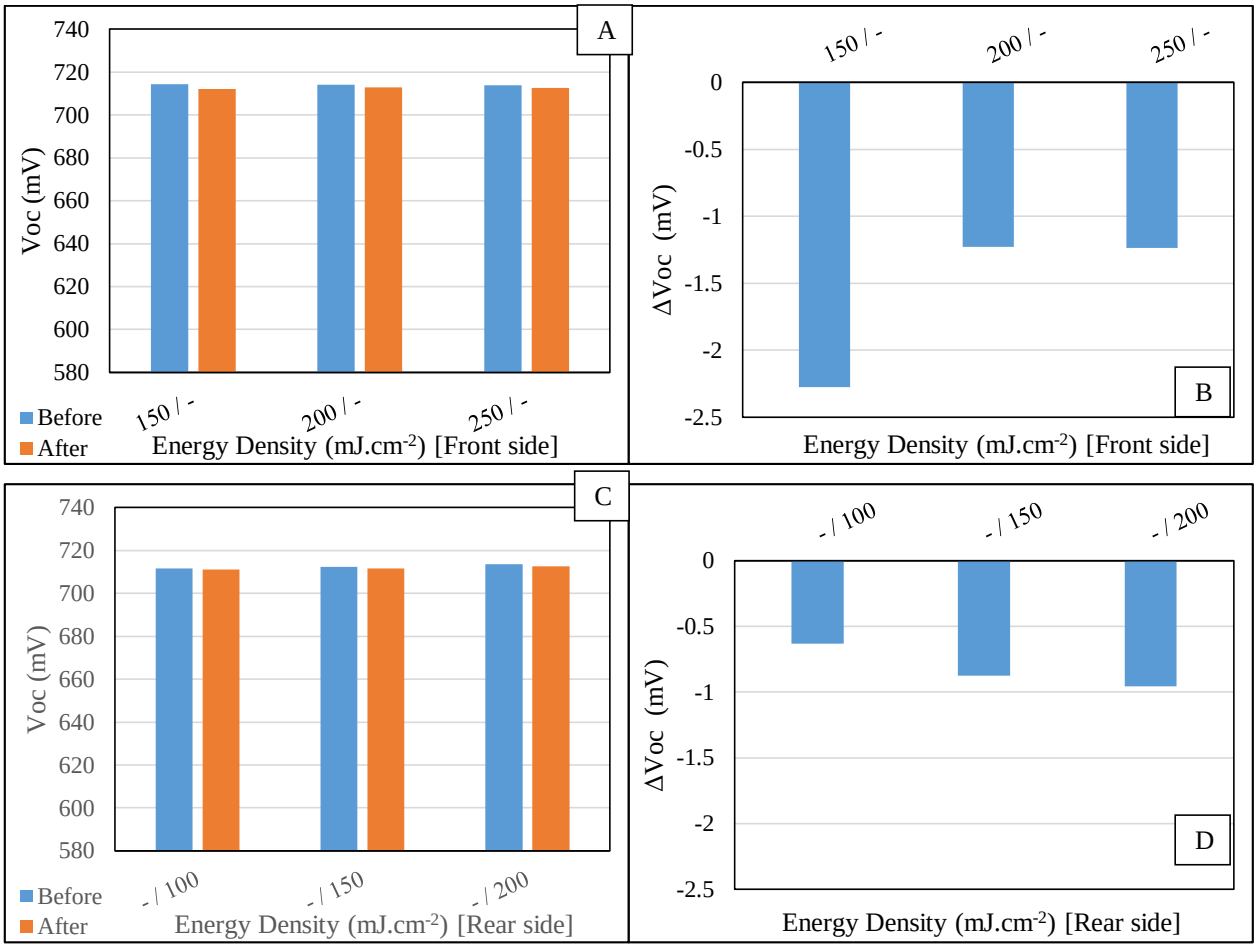

Figure 5-12. Open circuit voltage (V_{OC}) vs. laser fluences applied to: A) Front side, C) Rear Side of R&D HET solar cells. Variation of V_{OC} before and after ELA for: B) Front and D) Rear side treatment.

5.5.2 J_{SC} results for R&D HET solar cells

J_{SC} is slightly increased in all cases (for front side treatments and for rear side treatments, see Figure 5-13): this might be related to the improvement of optic properties in **ITO** after ELA.

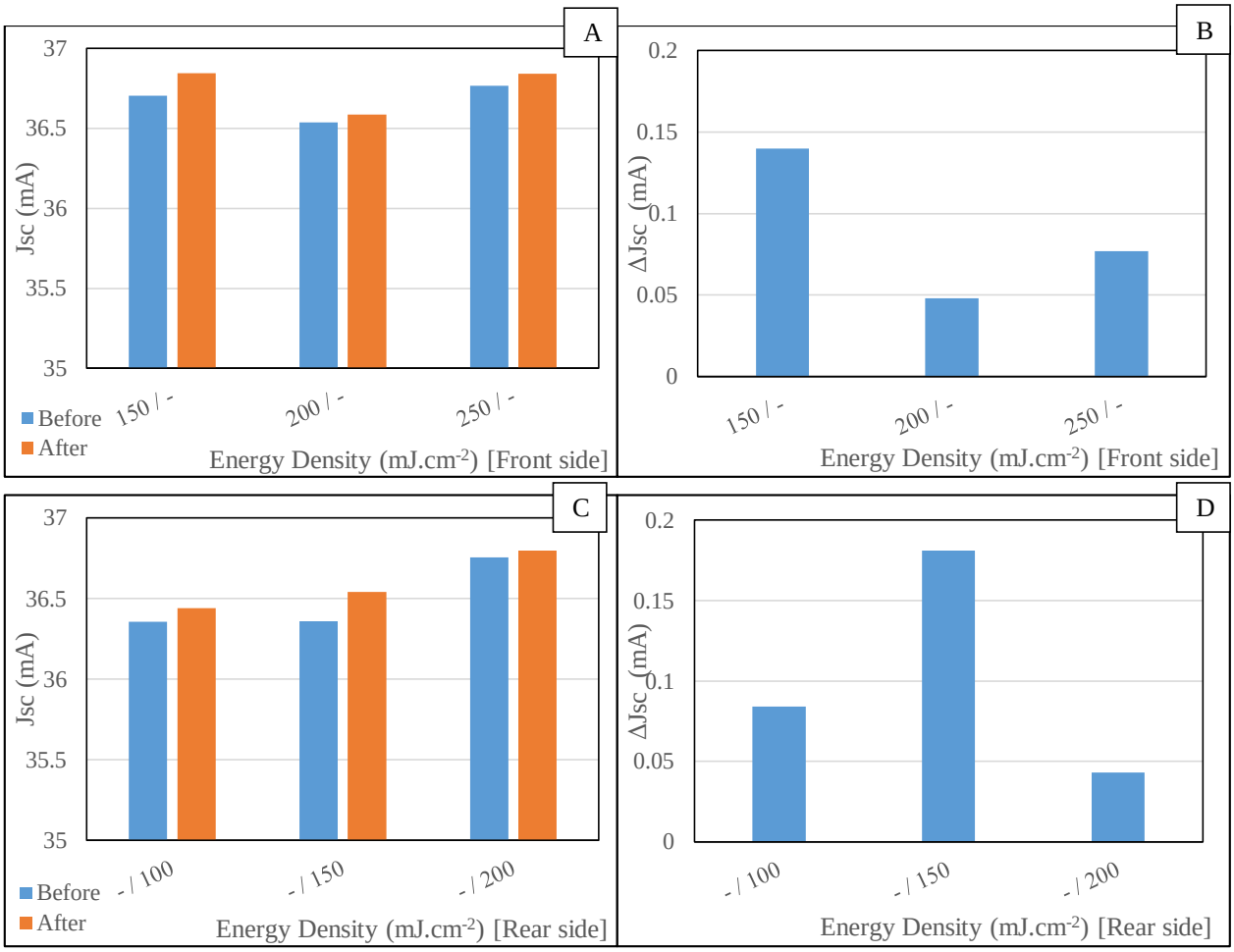

Figure 5-13. Short circuit current (J_{SC}) vs. laser fluences applied to: A) Front side, C) Rear Side of R&D HET solar cells. Variation of J_{SC} before and after ELA for: B) Front and D) Rear side treatment.

5.5.3 Fill Factor for R&D HET solar cells

FF decreases for the most energetic laser annealing treatments: this can probably be explained by the degradation of passivation leading to more recombination (see Figure 5-14.A and C). However this degradation remains very small probably due to the limited ELA energies that were used. However, for the 150 mJ/cm^{-2} Front side treatment (see Figure 5-14.B), there is a slight increase of the FF which can be related to the improvement in R□ of ITO.

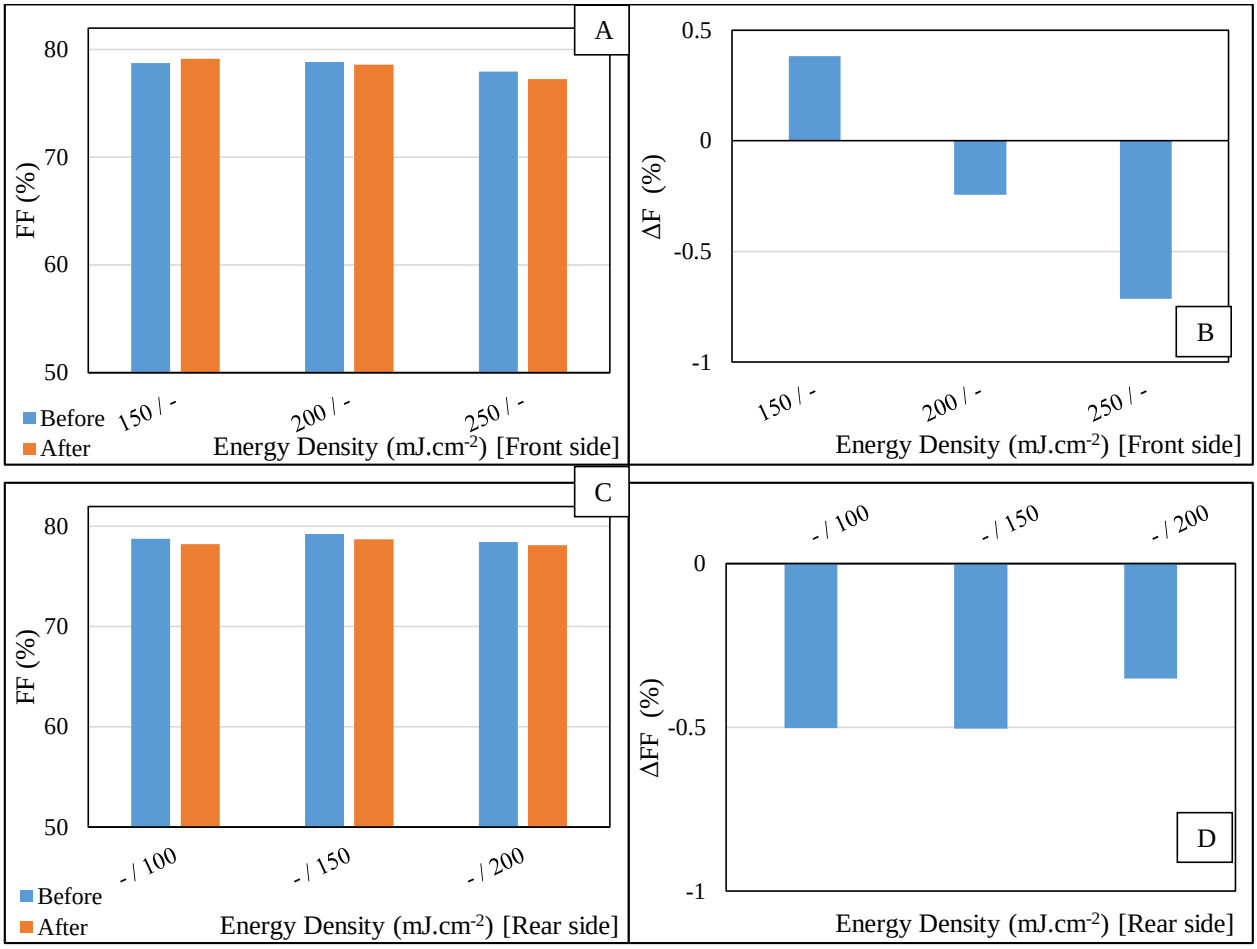

Figure 5-14. Fill Factor (FF) vs. laser fluences applied to: A) Front side, C) Rear Side of R&D HET solar cells. Variation of FF before and after ELA for: B) Front and D) Rear side treatment.

5.5.3.1 Why do values of Fill Factor drop?

Using the SunsVoc device (see section 5.2.3), we could get important information about Rs (series resistance), Rsh (shunt resistance) and pFF (pseudo Fill Factor) that would help us to know what causes the diminution of FF in R&D HET solar cells. The FF diminution could be mainly related to three possible causes:

1. Loss of pFF without diminution of R_{sh} which indicates that the cause is degradation of passivation.

2. Loss of pFF with diminution of R_{sh} which indicates that the cause is degradation of the junction.

3. Increment of Rs which indicates that the cause is the degradation of ITO thin films.

In Figure 5-15, it is shown that FF are not related to pFF values. Furthermore, in Figure 5-16, it can be seen that there is no relation either between pFF and Rsh values for R&D HET solar cells. In this way, Diminution of FF is not related to loss of pFF.

In Figure 5-17, there is a relation between inversed dependence of FF and Rs. However, the augmentation of Rs with different laser fluences does not match with the results for sheet resistance for a silicon wafer for the same values of ELA (see Figure 4-10). This can be explained by the difference between surfaces of substrates. The Surface of HET solar cells is textured with pyramidal motif, producing many reflections of laser beam before being reflected back from the surface. So the ITO thin film could absorb more energy (changing a little bit, ITO) for the same density of energy than for a non-pyramidal textured surface (Silicon wafer, see Figure 4-10).

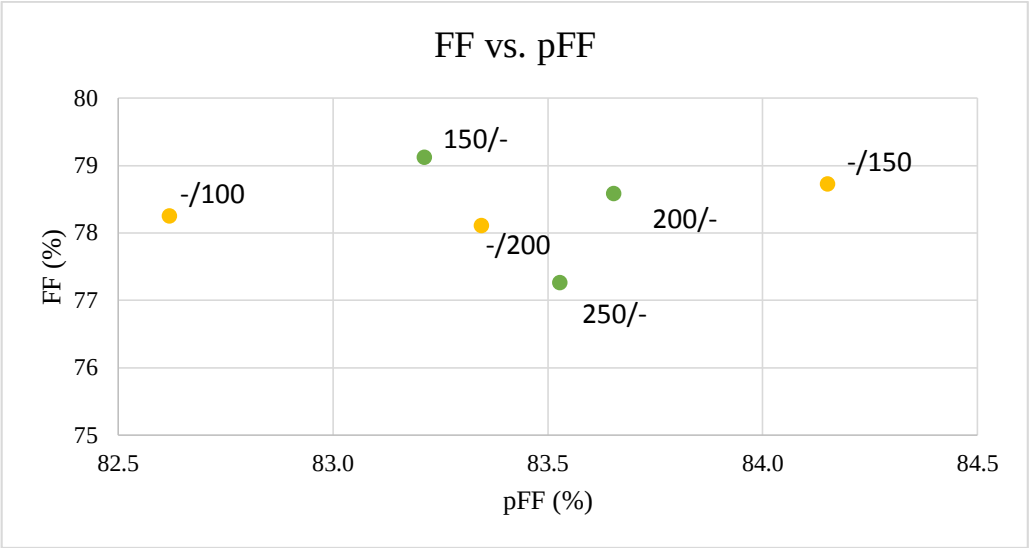

Figure 5-15. FF vs. pFF values for different laser fluences in R&D HET cells.

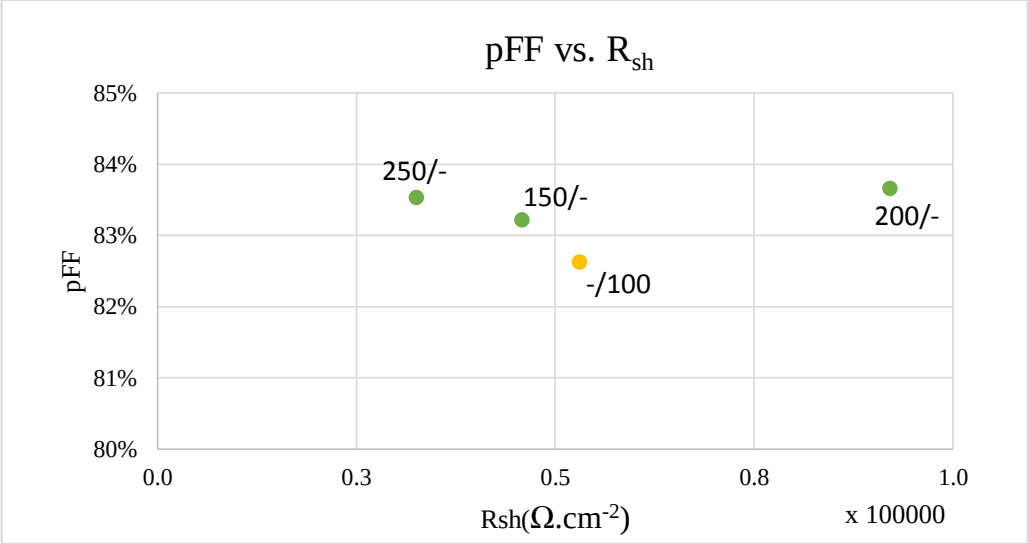

Figure 5-16. pFF vs. Rsh values for different laser fluences in R&D HET cells.

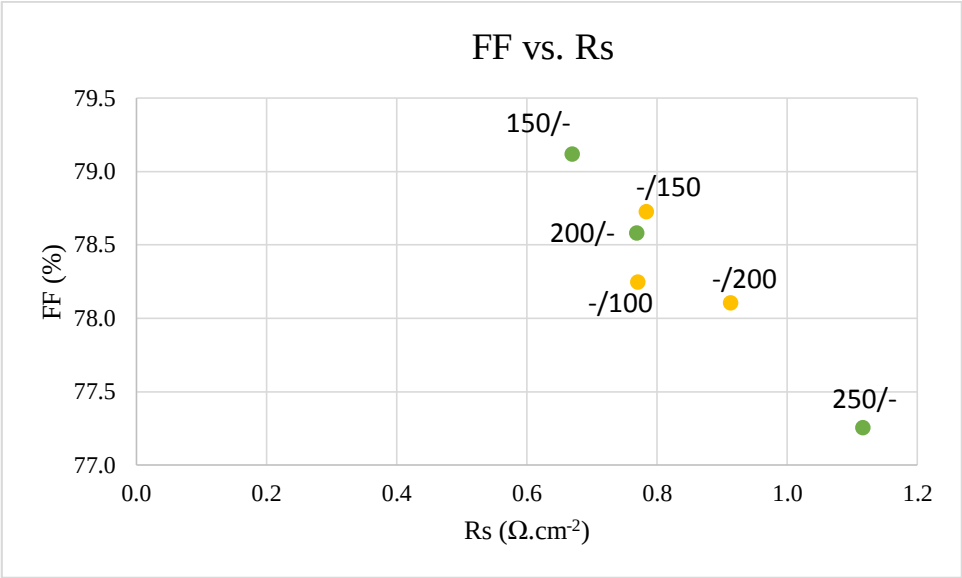

Figure 5-17. FF vs. Rs values for different laser fluences in R&D HET cells.

5.5.4 Efficiency for R&D HET solar cells

Efficiency slightly drops down for the more energetic ELA treatments due to the degradation of the passivation (see Figure 5-18.A and C). However for 150 mJ/cm² front side laser treatment, efficiency increases thanks to both FF and Jsc increase (see Figure 5-18.B) and limited degradation of the V_{OC}.

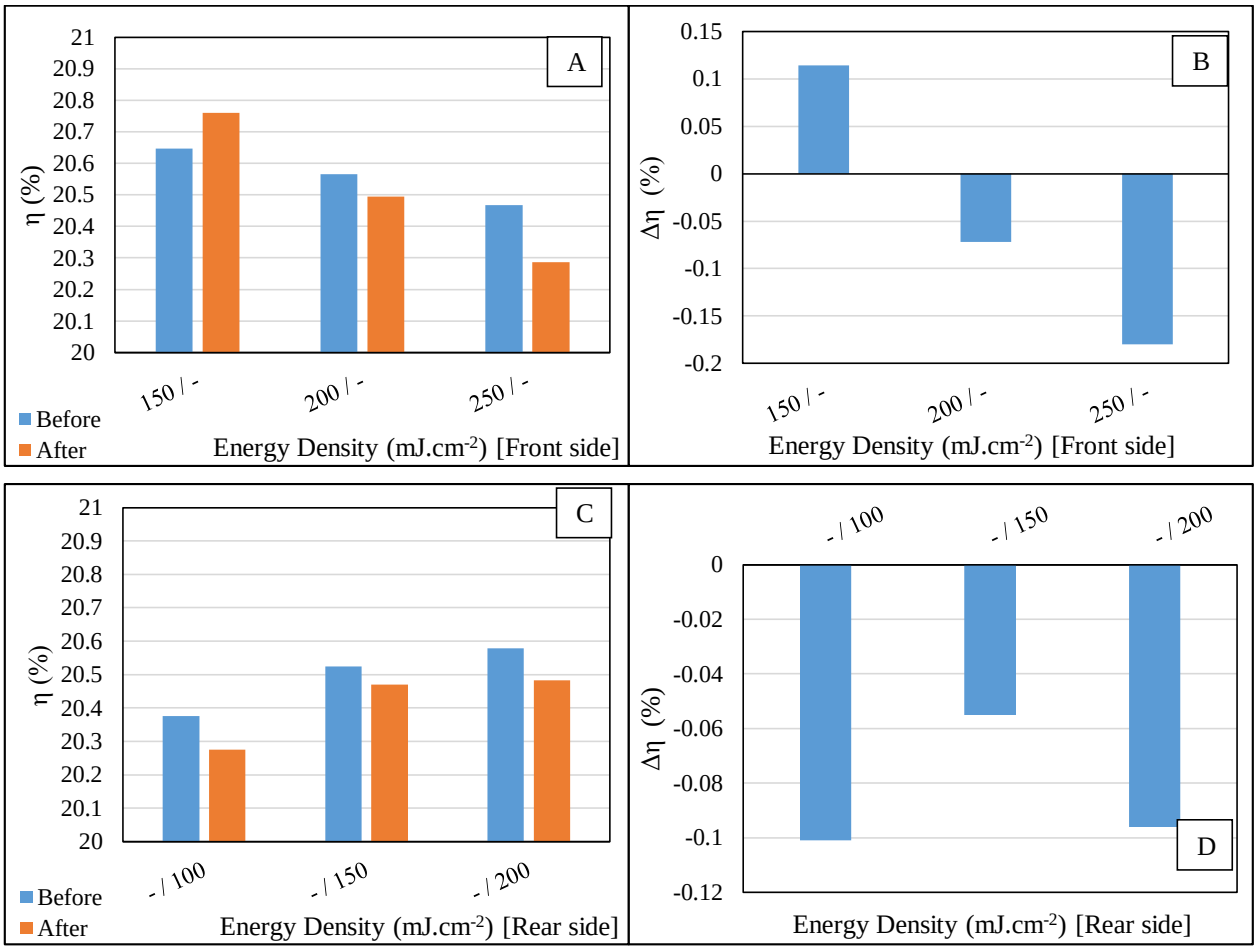

Figure 5-18. Efficiency (η) vs. laser fluences applied to: A) Front side, C) Rear Side of R&D HET solar cells. Variation of η before and after ELA for: B) Front and D) Rear side treatment.

6 CONCLUSIONS

6.1 Characterization of Laser-Annealed TCOs

1. There is a difference in the behavior of ITO, AZO and IOH thin films between glass and silicon substrates for the same energy density used in excimer laser annealing which indicates that laser annealing depends on the substrate. This can be explained in the following way: UV photons of the excimer laser are absorbed in TCOs by electronic excitations which decay in the order of picoseconds (10^{-12}s) by energy exchange between the lattice and free electrons, resulting in localized heating of the material. The heat spreads throughout the material by thermal conduction (Baeri, 1978) and can be evacuated from the TCO thin film into the substrate. The heat evacuation rate depends on the kind of substrate.

It seems that the TCO-glass interface (amorphous substrate) has not as good thermal contact as TCO-Si interface (crystalline substrate). For instance, ITO/g or AZO/g samples are more degraded than ITO/Si or AZO/Si samples at 500 mJ.cm^{-2} which would mean that the heat generated by the laser is not easily evacuated through the glass sample as it is through the Si substrate. This behavior is confirmed by IOH samples deposited on two similar substrates that only differ by the insertion of a thin film of SiO_2: IOH-RT/SiO_2/Si (yellow line in Figure 4-28.A) and IOH-RT/Si (red line in Figure 4-28.A) were laser annealed at 400 mJ.cm^{-2} producing a tremendous damage in IOH-RT/SiO_2/Si (sheet resistance out of scale) whereas IOH-RT/Si sheet resistance did not change.

2. The different materials behave different when submitted to ELA: while ITO shows a strong improvement in both its electrical and optical properties, AZO show only very few

changes and even a degradation of the mobility. IOH deposited at room temperature is also very little influenced by ELA while IOH deposited at 150ºC might have a similar behavior to ITO (which was deposited at 200ºC).

3. ELA of ITO seems to be very promising to enhance the performance of HET solar cells as a significant improvement of both electrical and optical was obtained for the layers deposited onto glass samples. However, since the behavior of the layers submitted to ELA depends on the substrate, it is difficult to estimate how the film will evolve when treated on a solar cell.

6.2 ELA of ITO as a HET solar cell component

1. For laser fluences lower than 200 $mJ.cm^{-2}$, the effect of ELA on cell performance is almost negligible. Since, there is an improvement of about 0.1% (absolute) in the efficiency of R&D HET solar cells for a particular laser fluence of 150 $mJ.cm^{-2}$ applied at the front side of the solar cell. This can be explained by the improvement of both optical and electrical properties of ITO thin films (R□ decreases) leading to an increase in J_{SC} (+0.14 mA/cm^2) and FF (+0.4% absolute) respectively. However, the reproducibility and the improvement of this promising result should be tested with more samples.

2. The results show there is difference of behavior under ELA between R&D and Pilot Line HET solar cells especially regarding the current which systematically increases under ELA for R&D cells while it remains stable or decreases for Pilot Line cells. This might indicate a different sensibility to ELA of ITO thin films produced in different chambers.

3. There is an augmentation of series resistance in R&D even at laser fluences lower than 200 $mJ.cm^{-2}$. This can be explained by the texturized surface of silicon wafers in HET solar

cells. The laser beam is reflected more than once before being completely reflected back from the surface (more energy absorbed) and producing some damage in ITO surface.

4. Pilot line cells had also a decrease in different physical quantities (Voc, Jsc, FF, etc) after laser annealing which can be explained by two phenomenon: degradation of hydrogen passivation or damage of ITO film.

6.3 Recommendations

Additional experiments would help to clarify some aspects of this research. Some of these aspects are listed as follows:

1. Change the deposition parameters of ITO thin films in order to study the influence of e.g. thickness, Oxygen content or deposition temperature in the final film before laser annealing. This might improve the effects of laser annealing.
2. Make ELA on the HET solar cells, before they are screen printed. Because, the ELA can be applied to all the solar cell surface. In this thesis, the ELA treatments were made after metallization which means that the ITO layer under the fingers and busses of the cell are not irradiated (not treated) by the laser.
3. Make a number of laser shots with the same density energy. These density energies must be below laser fluences used in this thesis. The use of more shots and low densities might anneal ITO layers slowly without diminution in passivation.
4. Test the reproducibility of excimer laser annealing on HET solar cells, applying the same energy density treatment to several HET solar cells of similar initial performance to check if the impact on solar cells performance is repeatable.

7 REFERENCES

(2 de September de 2014). Obtenido de Panasonic: http://eu-solar.panasonic.net/en/about-panasonic-solar/almost-40-years-of-solar-experience/

(9 de September de 2014). Obtenido de Edison Investment Research: http://www.edisoninvestmentresearch.com/sectorreports/IndiumGalliumOverview071011.pdf

Baeri, P. (February de 1978). A melting model for pulsing-laser annealing of implanted semiconductors. *J.Appl. Phys, 50*(2), 788-798.

Boukhicha, R. (2014). Influence of sputtering conditions on the optical and electrical properties of laser-annealed and wet-etched room temperature sputtered ZnO:Al thin films. *Thin Solid Thin, 555*, 13-17.

Charpentier, C. (2014). Evolution in morphological, optical and electronic properties of ZnO:Al thin films undergoing a laser annealing and etching process. *Solar Energy Materials & Solar Cells*(125), 223-232.

Chung, W. (2004). Room temperature indium tin oxide by XeCl excimer lasre annealing for flexible displays. *Thin Solid Films, 460*, 291-294.

Favre, W. (2011). Silicium de type n pour cellules à hétérojonctions: caractérisations et modélisations. (PhD. Thesis). Université Paris Sud. France

Green, M. (1992). *Solar cells - Operating Principles Technology and System Application.* Kensington, Australia: University of NSW.

Gupta, L. (1989). Band gap narrowing and the band structure of tin-doped indium oxide films. *Thin Solid Films, 176*, 33-34.

Johnson, E. (2011). Excimer laser annealing and chemical texturing of ZnO:Al sputtered at room temperature for photovoltaic applications. *Solar Energy Materials and solar cells.*(95), 2823-2830.

Keita, A.-s. (2012). *Etude par ellipsométrie spectroscopie des effets de taille sur les propriétés optiques de films minces composites à matrice diélectrique et du silicium nanostructuré.* (PhD. Thesis). Université de Lorraine. France.

Labrune, M. (2011). *Silicon surface passivation and epitaxial growth on c-Si by low temperature plasma processes.* (PhD Thesis). Ecole polytechnique. France.

Legeay, G. (2011). *Couches minces amorphes d'ITO: Caractérisation, structure, évolution et fonctionnalisation sous rayonnements UV.* (PhD. Thesis). Université de Rennes. France.

Martín de Nicolás, S. (2012). *a-Si:H / c-Si Heterojunction solare cell: Back side assessment and improvement.* (PhD. Thesis). Université Paris Sud. France.

Martín de Nicolás, S. (2012). Optimisation of ITO by excimer laser annealing for a-Si:H/c-si solar cells. *Energy Procedia, 27,* 586-591.

Muñoz, D. (2008). *Silicon heterojunction solar cells obtained by Hot-Wire CVD.* (Phd Thesis). Universitat de Catalunya.Spain.

Muñoz, D. (2012). *Key aspects on development of high efficiency heterojunction and IBC heterojunction solar cells: towards 22% efficiency on industrial size.* Frankfurt: Proceedings of the 27th EUPVSEC.

Smets, A. (12 de August de 2014). *Open course ET 3034 TUX Solar Energy*. Obtenido de TU Delft: http://delftxdownloads.tudelft.nl/solar/

Sze, S. (2006). *Physics of semiconducteur devices.* Willey.

Taguchi, M. (2013). 24.7 % Record Efficiency HIT solar cell on Thin Silicon wafer. *IEEE journal of Photovoltaics*, 1-4.

Van der Pauw, L. (1958). A method of measuring specific resistivity and Hall effect of discs of arbitrary shape. *Philips Res.*, 1-9.

Varache, R. (2012). *Development, characterization and modeling of interfaces of high efficiency Silicon Heterojunction solar cells.* (PhD Thesis). Technical University of Berlin, Berlin - Germany.